

Detailed Numerical Simulation of Liquid Jet In Crossflow Atomization with High
Density Ratios

by

Sina Ghods

A Dissertation Presented in Partial Fulfillment
of the Requirements for the Degree
Doctor of Philosophy

Approved May 2013 by the
Graduate Supervisory Committee:

Marcus Herrmann, Chair

Kyle Squires

Kangping Chen

Huei-Ping Huang

Wenbo Tang

ARIZONA STATE UNIVERSITY

August 2013

ABSTRACT

The atomization of a liquid jet by a high speed cross-flowing gas has many applications such as gas turbines and augmentors. The mechanisms by which the liquid jet initially breaks up, however, are not well understood. Experimental studies suggest the dependence of spray properties on operating conditions and nozzle geometry. Detailed numerical simulations can offer better understanding of the underlying physical mechanisms that lead to the breakup of the injected liquid jet.

In this work, detailed numerical simulation results of turbulent liquid jets injected into turbulent gaseous cross flows for different density ratios is presented. A finite volume, balanced force fractional step flow solver to solve the Navier-Stokes equations is employed and coupled to a Refined Level Set Grid method to follow the phase interface. To enable the simulation of atomization of high density ratio fluids, we ensure discrete consistency between the solution of the conservative momentum equation and the level set based continuity equation by employing the Consistent Rescaled Momentum Transport (CRMT) method. The impact of different inflow jet boundary conditions on different jet properties including jet penetration is analyzed and results are compared to those obtained experimentally by [1].

In addition, instability analysis is performed to find the most dominant instability mechanism that causes the liquid jet to breakup. Linear instability analysis is achieved using linear theories for Rayleigh-Taylor and Kelvin-Helmholtz instabilities and non-linear analysis is performed using our flow solver with different inflow jet boundary conditions.

ACKNOWLEDGEMENTS

This work was supported by the National Science Foundation grants NSF-CBET 0853627. Computations were performed using the ASU Fulton High Performance Computing cluster.

TABLE OF CONTENTS

	Page
LIST OF TABLES	v
LIST OF FIGURES	vi
CHAPTER	
1 Introduction	1
1.1 A General Description of Liquid Jet Atomization in Crossflow	2
1.2 Experimental and Numerical Challenges	6
1.3 Present Work	8
2 Jet in Crossflow Atomization	11
2.1 Primary Breakup Regimes	11
2.2 Jet Penetration(Column Trajectory)	13
3 Governing Equations	15
4 Numerical Method	17
4.0.1 Refined Level Set Grid Method	19
4.0.2 Flow Solver	21
4.0.3 Coupling to Lagrangian spray model	24
5 Verification	26
6 Impact of Boundary Conditions On Jet in Crossflow Atomization	37
7 Instability Analysis	57
7.1 Instability Modes	58
7.2 Proper Orthogonal Decomposition	59
7.3 Linear Analysis	59
7.4 Nonlinear Analysis	68
8 Summary and Future Work	80

CHAPTER	Page
REFERENCES	85

LIST OF TABLES

Table	Page
5.1 Error of the front position in the collapse of the water column.	29
5.2 Rms of amplitude error for damped surface wave.	31
5.3 Zero gravity 2D column oscillation. Error in oscillation period as compared to linear theory [2].	33
5.4 Shape errors for convection of high density droplet.	35
6.1 Operating conditions and characteristic numbers [1].	37
7.1 Operating conditions and characteristic numbers for the numerical simu- lations with $r = 10$ and $r = 100$ [3].	60

LIST OF FIGURES

Figure	Page
1.1 Rotary atomizers by GEA Process Engineering Inc. (left), pressure atomizers by GEA Process Engineering Inc. (right).	2
1.2 jet in crossflow atomizer [1] (left) and air blast atomizer [4] (right). . . .	3
1.3 bag breakup, column breakup and surface breakup of a round nonturbulent liquid jet in uniform gaseous crossflow [5]	4
1.4 A round nonturbulent liquid jet in uniform gaseous crossflow within the bag breakup regime [5]	5
1.5 Generation of artificial momentum when solving the momentum equation in non-conservative form.	9
2.1 Primary breakup regime map for nonturbulent round liquid jets in gaseous crossflow [5]	12
2.2 Visualization of primary breakup processes of round nonturbulent liquid jets in gaseous crossflow: a) $We = 0$, no breakup; b) $We = 3$, column breakup; c) $We = 8$, bag breakup; d) $We = 30$, multimode breakup; and e) $We = 220$, shear breakup [5].	13
4.1 Interfacial error leads to jump in momentum using non-conservative scheme(top), and leads to jump in velocity using a conservative scheme(center), but gives smooth momentum and velocity using CRMT method(bottom). . .	19
5.1 Qualitative comparison of dam-break results with density ratio 815, using non- method (left) and CRMT method (right) with no-slip boundary condition on the horizontal wall.	27
5.2 Non-dimensional front position (top) and non-dimensional height of water column (bottom) of dam-break versus non-dimensional time compared to the experimental results [6]	28

Figure	Page
5.3 Normalized amplitude(A/λ) of damped surface wave with density ratio 1000 versus time.	30
5.4 Normalized amplitude(A/λ) of damped surface wave with density ratio 1000 versus time using CRMT method.	31
5.5 Amplitude error E of damped surface wave for hexahedral (top) and prism (bottom) meshes using CRMT method.	32
5.6 Droplet shape after one passthrough using non-conservative method [7]. .	34
5.7 Droplet shape after one passthrough ($t = 1.0$) using CRMT method on hexahedral meshes. Thick lines are for numerical solutions and fine lines are the expected solution.	35
6.1 Computational domain and boundary conditions (top) and mesh detail near the injector (bottom) [8].	39
6.2 Velocity distribution in the nozzle from the single phase LESsimulation [8].	40
6.3 Instantaneous injector exit plane velocity distributions in axial direction from: database including nozzle geometry(left-top) [8], averaged database including nozzle geometry(right-top), turbulent pipe flow databas(bottom-left) and rotated database(bottom-right). Gas crossflow is from left to right.	41
6.4 Side view snapshots of jet in crossflow atomization using database(top) and data base average (bottom)	42
6.5 Side view snapshots of jet in crossflow atomization using pipe flow(top) and rotated data base(bottom)	43
6.6 Side view snapshots of jet in crossflow atomization with density rario $r=100$ at $t=5, 10, 15$ time units (top to bottom), using data base (left) and data base averaged (right).	44

Figure	Page
6.7 Front view snapshots of jet in crossflow atomization with density ratio $r=100$ at $t=5, 10, 15$ time units (top to bottom), using data base (left) and data base averaged (right).	45
6.8 Averaged normal cross sections of the jet for different distances from the bottom wall: $y/D=0.5(a)$, $y/D=1.0(b)$, $y/D=1.5(c)$	46
6.9 Pdf of drop diameters d generated directly by primary atomization. . . .	47
6.10 Averaged local momentum flux ratio for simulations using turbulent database including nozzle geometry.	48
6.11 Side view snapshots of jet in crossflow atomization with density ratio $r=100$ at $t=5, 10, 15$ time units (top to bottom), using data base (left) and pipe flow (right).	49
6.12 Front view snapshots of jet in crossflow atomization with density ratio $r=100$ at $t=5, 10, 15$ time units (top to bottom), using data base (left) and pipe flow (right).	50
6.13 Averaged normal cross sections of the jet for different distances from the bottom wall: $y/D=0.5(a)$, $y/D=1.0(b)$, $y/D=1.5(c)$	51
6.14 Pdf of drop diameters d generated directly by primary atomization. . . .	52
6.15 Side view snapshots of jet in crossflow atomization with density ratio $r=100$ at $t=5, 10, 15$ time units (top to bottom), using database (left) and rotated database (right).	53
6.16 Front view snapshots of jet in crossflow atomization with density ratio $r=100$ at $t=5, 10, 15$ time units (top to bottom), using database (left) and rotated database (right).	54
6.17 Jet penetration from the simulations using different local momentum flux ratios(q) based on a experimental study with $q=6.6$	55

Figure	Page
6.18 Averaged Volume of Fluid (left) and probability isoline (right).	55
6.19 Comparison between jet penetration from numerical simulations with density ratio $r=100$ and experimental correlations.	56
6.20 Comparison between jet penetration from numerical simulations with high density ratio and experimental correlations.	56
7.1 A schematic representation of the shear flow for Kelvin-Helmholtz instability study.	58
7.2 Proper orthogonal decomposition for $r=10$ (left) and $r=100$ (right) [3]. .	60
7.3 Center line(left) and normal line to the interface from the closest nodes on the surface(right).	63
7.4 Tangential velocity profile on the normal line to the interface for the interfacial nodes with associated nondimensional arc-length $s/D = 1.0$ (node4), $s/D = 1.75$ (node7), $s/D = 2$ (node8), $s/D = 2.25$ (node9), $s/D = 2.5$ (node10) for density ratio 10.	64
7.5 Tangential velocity profile on the normal line to the interface for the interfacial nodes with associated nondimensional arc-length $s/D = 1.0$ (node4), $s/D = 1.75$ (node7), $s/D = 2$ (node8), $s/D = 2.25$ (node9), $s/D = 2.5$ (node10) for density ratio 100.	65
7.6 Mean acceleration is calculated using the averaged leading edge based on VOF-0.5(top) and the velocity of the interfacial nodes(bottom).	66
7.7 Nondimensionalized mean acceleration on averaged leading edge based on VOF-0.5 for jet in crossflow with density ratio 10(top) and 100(bottom). .	67
7.8 The wavelength and growth-rate of Kelvin- Helmholtz and Rayleigh-Taylor instabilities for jet in crossflow simulation with density ratio 10.	68

Figure	Page
7.9 The wavelength and growth-rate of Kelvin- Helmholtz and Rayleigh-Taylor instabilities for jet in crossflow simulation with density ratio 100.	69
7.10 Side view snapshots of jet in crossflow atomization with density ratio $r=10$ at $t=5, 10, 15$ time units (top to bottom). Rayleigh-Taylor instability (left), Kelvin- Helmholtz instability (right).	72
7.11 Side view snapshots of jet in crossflow atomization with density ratio $r=10$ at $t=20, 25, 30$ time units (top to bottom). Rayleigh-Taylor instability (left), Kelvin- Helmholtz instability (right).	73
7.12 Front view snapshots of jet in crossflow atomization with density ratio $r=10$ at $t=5, 10, 15$ time units (top to bottom). Rayleigh-Taylor instability (left), Kelvin- Helmholtz instability (right).	74
7.13 Front view snapshots of jet in crossflow atomization with density ratio $r=10$ at $t=20, 25, 30$ time units (top to bottom). Rayleigh-Taylor instability (left), Kelvin- Helmholtz instability (right).	75
7.14 Side view snapshots of jet in crossflow atomization with density ratio $r=100$ at $t=5, 10, 15$ time units (top to bottom). Rayleigh-Taylor instability (left), Kelvin- Helmholtz instability (right).	76
7.15 Side view snapshots of jet in crossflow atomization with density ratio $r=100$ at $t=20, 25, 30$ time units (top to bottom). Rayleigh-Taylor instability (left), Kelvin- Helmholtz instability (right).	77
7.16 Front view snapshots of jet in crossflow atomization with density ratio $r=100$ at $t=5, 10, 15$ time units (top to bottom). Rayleigh-Taylor instability (left), Kelvin- Helmholtz instability (right).	78

Figure	Page
7.17 Front view snapshots of jet in crossflow atomization with density ratio $r=100$ at $t=20, 25, 30$ time units (top to bottom). Rayleigh-Taylor instability (left), Kelvin-Helmholtz instability (right).	79

Chapter 1

Introduction

Atomization is the process whereby a bulk liquid structure such as a liquid jet or sheet is transformed into a spray or other physical dispersions of small structures and particles in a gaseous atmosphere, due to different instability mechanisms. These instability mechanisms are activated by the kinetic energy of the liquid itself, by the exposure of high-velocity gas, or as a result of mechanical energy applied externally through a rotating or vibrating device. The atomization of liquids can be frequently found in nature and industry playing different roles. Natural sprays include waterfall mists, rains and ocean sprays. In the home, atomization is produced for example by shower heads, garden hoses, and hair sprays. In industry atomization is widely used in medical sprays (i.e. nebulizers and aerosol type drug delivery systems), agricultural sprays (i.e. crop dusting), food processing, paint sprays and combustion. This range of applications points out the importance of understanding the atomization process including the onset, types of instabilities that are responsible for the disruption of the liquid jet or sheet and characterization of the drop size distribution at the end of the process. For example, combustion of liquid fuels in diesel engines, spark ignition engines, gas turbines, rocket engines and industrial furnaces is dependent on effective atomization to increase the specific surface area of the fuel and thereby achieve high rates of mixing and evaporation as well as lower exhaust concentrations of pollutant emissions.

In spite of its importance we do not have a thorough knowledge of the atomization process in order to predict the outcome of atomization for an arbitrary given situation. The main reason that prevents us to have such ability is the complexity of the problem and variety of mechanisms involved in the process. In the following section the atomization of a liquid jet in cross flow will be explained in more detail.

1.1 A General Description of Liquid Jet Atomization in Crossflow

Sprays can be produced in various ways. Essentially, all that is needed is a high relative velocity between the liquid to be atomized and the surrounding air or gas. Some atomizers accomplish this by discharging the liquid at high velocity into a relatively slow-moving or stagnant stream of gas. Notable examples include the various forms of pressure atomizers (as is typically done in diesel and gasoline engines) and also rotary atomizers (which eject the liquid from the periphery of a rotating cup or disk).

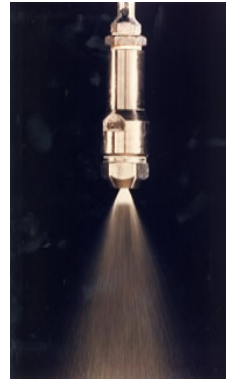


Figure 1.1: Rotary atomizers by GEA Process Engineering Inc. (left), pressure atomizers by GEA Process Engineering Inc. (right).

An alternative approach is to expose the liquid to a high-velocity airstream. It can be a coaxial gas stream (like in air-blast atomizers) or gaseous crossflow (with aerospace applications such as gas turbines and augmentors).

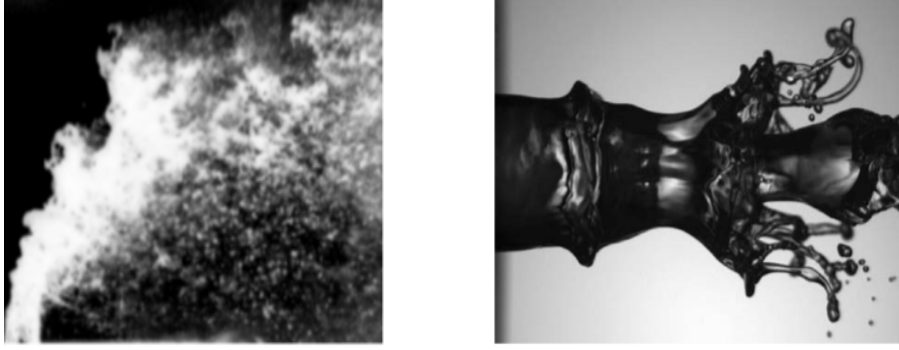


Figure 1.2: jet in crossflow atomizer [1] (left) and air blast atomizer [4] (right).

The typical atomization process which occurs in jet in crossflow atomization is explained in details by [9] and we bring a brief summary of it. The bulk liquid is called liquid column. The process by which a contiguous column of liquid initially breaks into drops is typically called *primary breakup*. The drops formed during primary breakup called *primary droplets* can then undergo *secondary breakup* into smaller droplets which finally evaporate and form the desired cloud of vapor. The most important mechanisms involved in secondary breakup are shear forces and turbulent stresses [10].

As figure 1.3 shows, the breakup process begins with deformation of the liquid column from a circular cross-section into an ellipsoidal cross-section. This behavior is caused by reduced gas pressure along the sides of the liquid jet due to acceleration of the gas across the liquid column, with the lateral motion eventually stabilized by surface tension. The windward side of the column establishes a stagnation zone in the oncoming air stream, while the leeward side establishes a low-pressure wake. The increased drag force due to the flattened shape of the liquid column enhances its

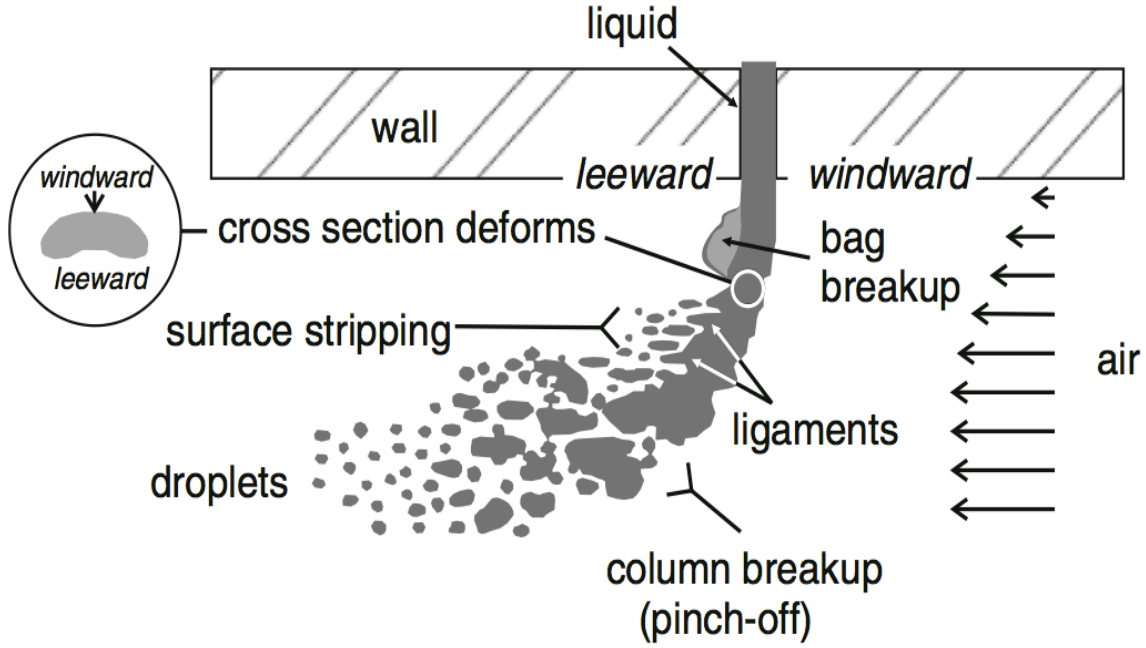


Figure 1.3: bag breakup, column breakup and surface breakup of a round nonturbulent liquid jet in uniform gaseous crossflow [5]

tendency to be deflected downstream due to cross flow gas motion. Primary breakup can occur via a number of processes, and real jets in crossflow tend to breakup under a combination of them called *mixed mode* breakup.

First, longitudinal waves are induced by the gas flow along the windward side of the column, and when their wavelength is larger than the jet diameter, the amplitude of these waves grows in the downstream direction of the liquid. Ultimately, the column can break producing very large drops. This pinch-off process is also called *column breakup*.

At the same time, the gas flowing past the stagnation point on the liquid column accelerates as it flows around to the sides of the column. This flow can develop transverse surface waves. At moderate relative gas velocities, these waves can form

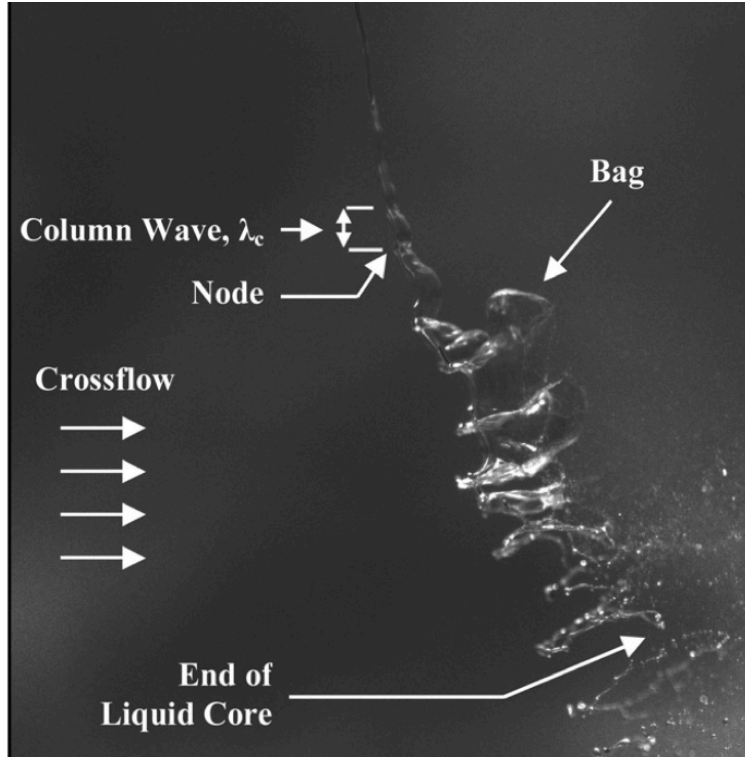


Figure 1.4: A round nonturbulent liquid jet in uniform gaseous crossflow within the bag breakup regime [5]

extended membranes that stretch downstream of the column, called *bag-breakup*. Bag-like structures develop between the nodes. With increasing streamwise distance along the liquid column, the bags grow progressively and their membrane eventually breaks up. This leaves the nodes connected by thin strings. The remaining thin liquid strings (rings) eventually breakup into droplets. During bag-breakup, longitudinal surface waves on the windward side of the column can still be observed.

In another type of instability wavelike disturbances appear on the upstream side of the deflected liquid column. The wavelength of these disturbances is smaller than the diameter of the liquid column and they do not develop into the nodes

observed in the bag-breakup regime. Instead they grow into ligaments that form around the periphery of the liquid jet and extend from the downstream side of the liquid column. These ligaments are terminated when drops are stripped from their ends. This process is termed *surface stripping* or sometimes *aerodynamic stripping*. Under some conditions, longitudinal waves are not observed on the windward side, but they are observed to develop toward the leeward side under surface stripping. These are typically called *leeward waves*. Both bag breakup and surface stripping are usually called *shear breakup*. As mentioned, the breakup of the bags and ligaments into a dispersed set of drops due to capillary forces is typically referred to as *primary breakup*.

As can be seen from the above general description, atomization is a very complicated multiphase process involving different length and time scales and turbulent properties with a very complex changing interface. Due to these complexities it is very challenging to observe, model and simulate this process experimentally or numerically. In the following we will explain these difficulties more in detail and show how our proposed research can help us to have a better understanding of the atomization in jet in crossflow atomizers.

1.2 Experimental and Numerical Challenges

A detailed experimental study of the primary breakup in the near field of atomizing sprays has many different challenges. One of them is the various time and length scales involved in the atomization process that forces experimental methods to have high temporal and spatial resolutions in order to provide data that can correctly explain different mechanisms. For example, in order to analyze different instability mechanisms that originate in the distortion of the interface, one needs to know the relative velocities of liquid and gas at the interface close to the nozzle over the time. This is very difficult to be measured by experimental methods specially for the

velocity in the gas at the interface. One of the other main reasons is a dense fog of droplets obscures the interior of the near field and because of that, many of the typical flow visualization methods are impractical in this case. Many theories about primary breakup of the jet have thus been based upon secondary observations such as the behavior of droplets on the spray periphery [11]. There are some Ultrafast X-ray techniques [12] that makes it possible to have access to the phase interface directly without any interface from the cloud around it, but the temporal and spatial resolution of them are still not high enough to capture the dynamics of the problem. A technique called Ballistic imaging has also been developed to visualize the interface in detail [13] ,[11]. While this provides temporal resolutions on the order of 1.8 *ps*, the spatial resolution of 10 μm is insufficient to probe the small scale dynamics.

Besides, many multiphase flows involving atomization occur under conditions where the ratio of liquid to gas fluid density is large. Even though some atomization devices operate in pressurized gaseous environments under real operating conditions, such devices are often studied experimentally under ambient pressure conditions to lower experimental cost. As such significant more experimental data exists for ambient (i.e. large density ratio) conditions than for high pressure (i.e. low density ratio) conditions.

The case is reversed for detailed numerical simulations of atomizing flows. There, a large density ratio can result in a more stiff system of equations that are more costly to solve. Furthermore, some classes of numerical techniques describing the dynamics of the phase interface in incompressible flows, mostly level set based methods, are prone to numerical instabilities if all of the following three conditions are met: a) the liquid-to-gas density ratio is large, of the order of 100 or more, b) the phase interface geometry is complex, as is typical of atomizing flows, and c) the flow exhibits a large shear at the phase interface, common to many atomization devices. Moreover,

numerical simulations of atomizing sprays should be able to handle the discontinuities of material properties at the phase interface as well as the singular surface tension force in the Navier-Stokes equations in a way that the solution remains accurate and stable. One should also remember that the temporal and spatial resolution is still an issue in the numerical simulations in order to resolve the dynamic of the problem completely.

The next section will explain our present research and show how it can help us to overcome these challenges.

1.3 Present Work

From the previous sections it can be concluded that the atomization of a liquid column in a crossflow gas is a very important process that needs to be fully understood, but unfortunately there is not a thorough knowledge about this problem due to the difficulties that exists when studying this problem either numerically or experimentally. The focus of this dissertation is on developing numerical methods and performing numerical simulations in order to obtain a better understanding of the underlying physics of the problem.

As mentioned briefly before, in numerical simulations of multiphase flows, there are some phase interface tracking methods, such as level set based methods, prone to numerical instabilities under some conditions which is typically the case in simulation of jet in crossflow atomization where complex geometry, high shear and high density ratio exist. These instabilities originate when there is a small error in the interface position and show themselves in the form of large jumps in velocities due to large momentum that is artificially generated. Figure 1.5 shows the error in the position and large momentum that can be generated as a result of that error in the position.

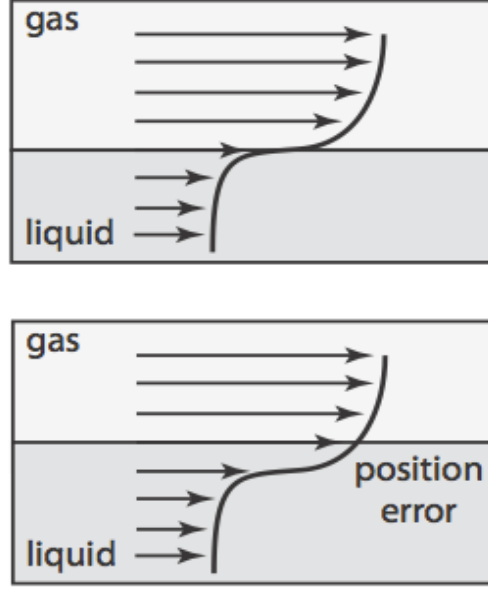


Figure 1.5: Generation of artificial momentum when solving the momentum equation in non-conservative form.

A new method called *Consistent Rescaled Momentum Transport* (CRMT) is proposed in this dissertation to avoid these artificial numerical instabilities. This will enable us to perform numerical simulations with the conditions similar to experimental studies, and the resulting data can be used in analysis of jet in crossflow atomization.

Another problem one may encounter studying jet in crossflow atomization is the ambiguity of the boundary conditions used in experimental studies. In other words, different numerical simulations using different numerical boundary conditions can be performed based on a specific experimental study, all having the same nominal characteristics numbers yet giving totally different results. The importance of the boundary conditions in studying jet in crossflow atomization is shown in this dissertation by performing different numerical simulations based on one configuration used in an experimental study.

Earlier in this section different breakup modes that cause the liquid column to break up were explained and some experimental studies that investigate those instabilities were mentioned. The majority of experimental studies suggest that breakup of the liquid column is due to the so-called Rayleigh-Taylor instability mechanism. In this dissertation both linear and nonlinear instability analysis is performed using results of numerical simulation in order to explore the breakup of the liquid jet in crossflow numerically. Since most of the experimental studies are performed at ambient pressure with high density ratio, the focus is more on lower density ratios in the numerical analysis performed in this dissertation in order to ascertain if there is any chance for other instability mechanisms for different operating conditions. In general switching to lower density ratios gives the gas higher relative momentum which is needed for instabilities such as shear driven instability. So in lower density ratios there might be a possibility for shear driven instabilities to dominate the other type of instability that experimental studies usually suggest is responsible for the liquid jet breakup, which is acceleration instability.

The dissertation is organized as follows: First the atomization of jet in crossflow and different characteristics associated to this process are explained in detail in chapter 2. Chapter 3 explains the governing equations solved in our numerical simulations. In chapter 4 the proposed numerical method is discussed that enables us to perform numerical simulations with high density ratios. Chapter 5 includes different numerical test cases performed in order to verify the new method. Chapter 6 shows the effect of different boundary conditions on numerical simulations of jet in crossflow. In chapter 7 different instability mechanisms acting on the breakup of the jet in crossflows are explored. Chapter 8 summarizes the dissertation, including the conclusions and future works.

Chapter 2

Jet in Crossflow Atomization

In this section regime maps for different breakup modes generated based on experimental studies are explained. These maps are based on characteristic numbers of the jet in crossflow problem such as momentum flux ratio and Weber number (We) as showed in figure 2.1. General characteristics for jet in crossflow from experimental studies will be reviewed. A thorough explanation of jet in crossflow breakup and atomization can be found in [5],[14] and [9].

2.1 Primary Breakup Regimes

The Weber number is defined as a ratio between forces that act to break apart a liquid structure and the surface tension acting to hold it together. For each style of spray, We is defined in a particular way that most appropriately emphasizes the critical breakup processes. For a jet in crossflow, We is typically defined in terms of the crossflow velocity and the jet diameter by:

$$We = \frac{\rho_g D u_g^2}{\sigma} \quad (2.1)$$

where ρ_g is the density of the crossflow, D is the liquid jet diameter exiting the nozzle, u_g is the velocity of liquid jet and crossflow and σ is the surface tension coefficient. In the absence of crossflow ($We = 0$), a nonturbulent liquid jet exhibits a smooth surface with no disturbances or protrusions of the surface of the liquid column, and no initiation of atomization even for relatively high Reynolds numbers [5], like $Re_l = 30,000$ rather than Rayleigh-Plateau instability.

Here we focus on conditions where effects of liquid viscosity are small ($Oh \leq 0.1$). The Ohnesorge number relates the viscous forces to inertial and surface tension forces:

$$Oh = \frac{\mu_l}{\sqrt{\rho_l D \sigma}} \quad (2.2)$$

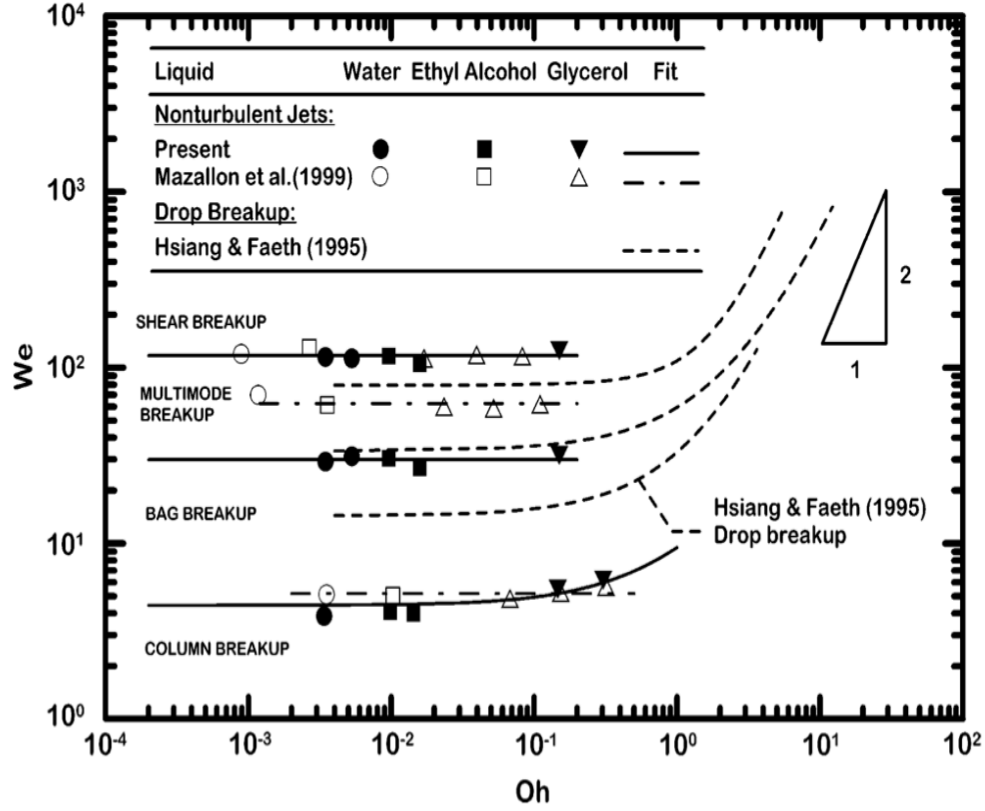


Figure 2.1: Primary breakup regime map for nonturbulent round liquid jets in gaseous crossflow [5]

where ρ_l, μ_l are density and dynamic viscosity of the liquid jet. For low Oh numbers, breakup regime transition of the liquid jet is determined by the crossflow Weber number as follows (figure 2.2): column breakup ($We < 4$), bag breakup ($4 < We < 30$), multimode breakup ($30 < We < 110$), and shear breakup ($110 < We$). Bag breakup and shear breakup are explained in the previous section, column breakup (also called enhanced capillary breakup) happens when aerodynamic forces are not large as com-

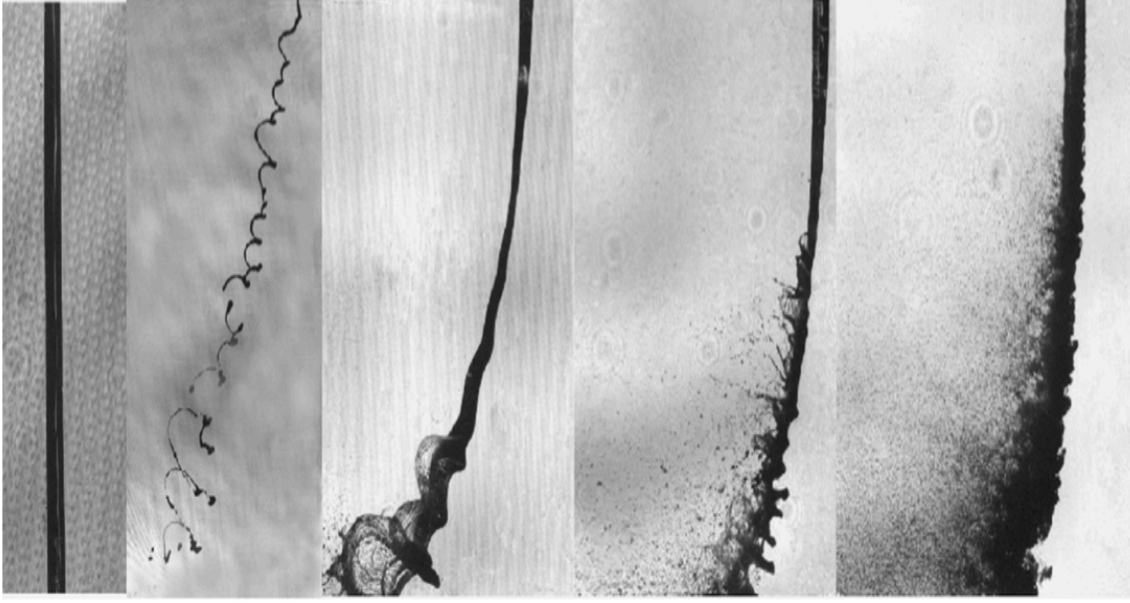


Figure 2.2: Visualization of primary breakup processes of round nonturbulent liquid jets in gaseous crossflow: a) $We = 0$, no breakup; b) $We = 3$, column breakup; c) $We = 8$, bag breakup; d) $We = 30$, multimode breakup; and e) $We = 220$, shear breakup [5].

pared to liquid surface tension forces. In this condition, breakup occurs due to Plateau-Rayleigh type of instability, and the liquid jet is curved by aerodynamic forces which also accelerate the breakup processes caused by capillary forces. Multimode breakup shows both bags and liquid break off with small sheared droplets.

Sallam et al.[5] also explored the wavelength λ_s of the longitudinal waves on the windward), discussed how they change with conditions, and then reported correlations between λ_s/D and breakup mode. When $\lambda_s/D > 1$ column breakup was observed, when $\lambda_s/D \approx 1$ bag breakup was observed, and when $0.1 < \lambda_s/D < 1.0$ a multimode region featuring surface stripping and column breakup was observed.

2.2 Jet Penetration(Column Trajectory)

Various analytical and experimental studies have been done in order to give an equation for the jet penetration curve in the jet direction and crossflow direction plane.

For example, [15] have modeled the liquid column as a cylindrical fluid element with nozzle exit diameter, D which is assumed to be constant. This means no mass loss is caused by evaporation and drop removal along the liquid column. The deformation and flattening of the liquid column are accounted for with an averaged drag coefficient. It is also assumed that the liquid column velocity in the nozzle direction remains constant. With the above conditions, the jet trajectory can be calculated as

$$\frac{y}{D} = 1.37(q\frac{x}{D})^{0.5} \quad (2.3)$$

Stenzler et al., [16] also found a close correlation,

$$\frac{y}{D} = 2.63q^{0.442}(\frac{x}{D})^{0.5} We^{-0.088}(\frac{\mu_l}{\mu_{H_2O}})^{-0.027} \quad (2.4)$$

where q is the momentum flux ratio between liquid and gas:

$$q = \frac{\rho_l U_l^2}{\rho_g U_g^2} \quad (2.5)$$

The difference between two above equations is that eq.2.4 depends not only on momentum flux ratios but also on the viscosity ratios and We number. Experimental studies show that eq.2.4 gives a better prediction for jet in crossflow atomizations with higher We numbers which are typically in the shear breakup mode, and eq.2.3 gives a better prediction for jet in crossflow atomizations with lower We numbers which are typically in the column breakup mode. The experimental results of Brown & McDonell [1] are in good agreement with the above correlations.

Chapter 3

Governing Equations

The equations governing the motion of an unsteady, incompressible, immiscible, two-fluid system are the Navier-Stokes equations in conservative form,

$$\frac{\partial \rho \mathbf{u}}{\partial t} + \nabla \cdot (\rho \mathbf{u} \mathbf{u}) = -\nabla p + \nabla \cdot (\mu (\nabla \mathbf{u} + \nabla^T \mathbf{u})) + \rho \mathbf{g} + \mathbf{T}_\sigma \quad (3.1)$$

or in non-conservative form,

$$\frac{\partial \mathbf{u}}{\partial t} + \mathbf{u} \cdot \nabla \mathbf{u} = -\frac{1}{\rho} \nabla p + \frac{1}{\rho} \nabla \cdot (\mu (\nabla \mathbf{u} + \nabla^T \mathbf{u})) + \mathbf{g} + \frac{1}{\rho} \mathbf{T}_\sigma \quad (3.2)$$

where \mathbf{u} is the velocity, ρ the density, p the pressure, μ the dynamic viscosity, \mathbf{g} the gravitational acceleration, and \mathbf{T}_σ the surface tension force which is non-zero only at the location of the phase interface \mathbf{x}_f ,

$$\mathbf{T}_\sigma(\mathbf{x}) = \sigma \kappa \delta(\mathbf{x} - \mathbf{x}_f) \mathbf{n}, \quad (3.3)$$

with σ the assumed constant surface tension coefficient, κ the local mean surface curvature, \mathbf{n} the local surface normal, and δ the delta-function. In addition, conservation of mass results in the continuity equation,

$$\frac{\partial \rho}{\partial t} + \nabla \cdot (\rho \mathbf{u}) = 0. \quad (3.4)$$

The phase interface location \mathbf{x}_f between the two fluids is described by a level set scalar G , with

$$G(\mathbf{x}_f, t) = 0 \quad (3.5)$$

at the interface, $G(\mathbf{x}, t) > 0$ in fluid 1, and $G(\mathbf{x}, t) < 0$ in fluid 2. Differentiating (3.5) with respect to time yields the level set equation,

$$\frac{\partial G}{\partial t} + \mathbf{u} \cdot \nabla G = 0 \quad (3.6)$$

For numerical accuracy of geometric properties of the phase interface it is advantageous, although not necessary, to define the level set scalar away from the interface to be a signed distance function,

$$|\nabla G| = 1 \quad (3.7)$$

Assuming ρ and μ constant within each fluid, density and viscosity at any point \mathbf{x} can be calculated from

$$\rho(\mathbf{x}) = H(G)\rho_1 + (1 - H(G))\rho_2 \quad (3.8)$$

$$\mu(\mathbf{x}) = H(G)\mu_1 + (1 - H(G))\mu_2 \quad (3.9)$$

where indices 1 and 2 denote values in fluid 1, respectively 2, and H is the Heaviside function. Finally, the interface normal vector \mathbf{n} and the interface curvature κ can be expressed in terms of the level set scalar as

$$\mathbf{n} = \frac{\nabla G}{|\nabla G|}, \quad \kappa = \nabla \cdot \mathbf{n}. \quad (3.10)$$

Chapter 4

Numerical Method

To solve the governing equations accurately and effectively on massively parallel computer architectures we employ two in-house Fortran codes. Interface tracking is accomplished with LIT(Level set Interface Tracker) which is based on the Refined level set grid (RLSG) method [7]. The velocity field is updated using the flow solver CDP(Cascade Technology Inc.).

As mentioned briefly in chapter 1, using a general level set method to track the interface in the multiphase simulations with huge density ratios can lead to numerical instabilities. The numerical instabilities manifest themselves in a sudden spike in local velocity that can grow unbounded.

Interestingly enough, some numerical methods to describe the phase interface motion appear not to be susceptible to numerical instability, among them the volume of fluid geometric transport methods, see [17] and references therein. The important difference of these methods to most level set based approaches lies not only in the fact that the volume of fluid (VOF) approaches solve the momentum equation in conservative form, but more importantly that they employ discrete operators for the convection terms in the momentum and VOF-scalar equation that are exactly equivalent. They thus ensure that mass (in the form of the VOF scalar), and momentum are transported in exactly the same discrete manner.

Level set based methods, on the other hand, transport mass and momentum in entirely different ways. Mass is transported by solving the level set equation, a Hamilton-Jacobi type equation. Momentum, on the other hand, is transported using a standard non-conservative formulation of the Navier-Stokes equations. Thus, even a small error in the position of the phase interface (as shown in figure4.1 (top)) can

lead to strong generation of artificial momentum in the presence of large density ratios and large shear in the velocities. This happens because a standard non-conservative method keeps the velocity distributions the same, while the error from the level set leads to the error in the density distribution and as a result in the momentum distribution.

Trying to conserve momentum by switching to a conservative form of the Navier-Stokes equations is equally bound to fail, since the density necessary to reconstruct velocity from momentum is again prone to phase interface position errors and can generate unphysical velocity distributions(as shown in figure 4.1 (middle)). Thus minimizing position errors of the phase interface can alleviate the problem, however, even if a level set method were mass conserving, there still exists the mechanism of artificial momentum/velocity creation since momentum and mass are not guaranteed to be transported in a discretely consistent manner. The key in avoiding the numerical instability is thus to ensure a discretely consistent transport of mass and momentum.

To this end, Raessi [18] and, Raessi & Pitsch [19] introduced a method to construct flux densities [20] from level set scalar information and use these flux densities to transport momentum in a consistent manner. However, their method is presently limited to one- and two-dimensional cases and not straightforward to extend to three dimensions.

In the proposed *Consistent Rescaled Momentum Transport* (CRMT) method explained later in this chapter, this consistency is enforced. The new method is viable in three dimensions, applicable to unstructured, collocated finite volume formulations of the governing equations and consistent with the balanced force formulation [7]. figure 4.1(bottom) illustrates the consistency in mass and momentum transport and how *CRMT* method can fix this problem. In this method, errors in the mass and momentum are not eliminated, but they are forced to be consistent. So recovering

velocity distribution from mass and momentum will give a bounded results.

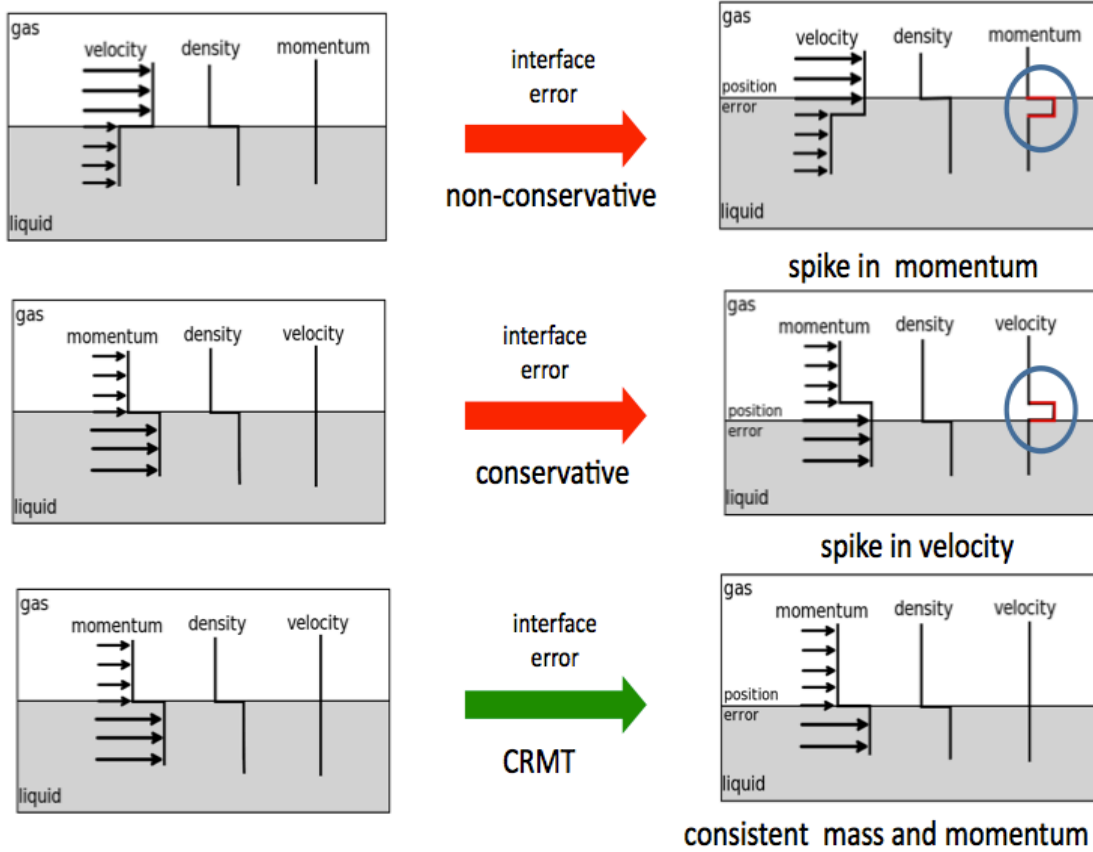


Figure 4.1: Interfacial error leads to jump in momentum using non-conservative scheme(top), and leads to jump in velocity using a conservative scheme(center), but gives smooth momentum and velocity using CRMT method(bottom).

Flow solver(including the implementation of CRMT method), level set solver and the coupling between them will be discussed in the following sections.

4.0.1 Refined Level Set Grid Method

Level set methods are one of the most common methods to track interfaces that have several benefits such as efficiency, ease of parallel implementation, the ability to automatically handle topology changes and making interface geometry such as interface normal and curvature easily calculable. One of the main issues of these methods is that on pure level set methods there is no constraint to conserve the volume

enclosed by the interface (and mass). There are numerous methods of addressing this issue. Most of these involve coupling the level set method to a volume conserving algorithm, see for example [21], [22], [23].

Since volume errors are proportional to grid size an alternative approach is to solve all level set related equations on a separate more refined grid (called the G-grid). The G-grid can then be refined independently of the flow solver grid allowing one to obtain a grid converged interface. Furthermore, since level set data is only needed near the interface, a narrow band approach similar to that of [24] can be followed where the level set equations are only solved in a narrow band of control volumes around the interface. This is the idea behind the RLSG method. Further details of the scalability, parallel implementation and domain decomposition algorithms can be found in [7].

The level set advection equation (eq.3.6) is solved using a fifth-order WENO scheme [25], coupled with the third-order TVD Runge-Kutta time discretization found in [26]. The use of high-order methods helps ensure that volume errors will be small.

From a computational point of view it is desirable to ensure that G is a smooth function with $|\nabla G| = 1$. The advection equation does not maintain this property so it is necessary to reinitialize G as a signed distance function away from the interface. The PDE-based re-initialization procedure of [27] is employed

$$\frac{\partial G}{\partial t^*} + S_0(|\nabla G| - 1) = 0 \quad (4.1)$$

where S_0 is the modified sign function of [24]

$$S_0 = \frac{G}{\sqrt{G^2 + |\nabla G|^2 h_G^2}} \quad (4.2)$$

where h_G is the G-grid spacing.

4.0.2 Flow Solver

The Navier-Stokes equations are solved using a fractional step method [28] on unstructured collocated meshes using a finite volume approach, where control volume material properties like density and viscosity are defined using (3.8) and (3.9) as

$$\rho_{cv} = \psi_{cv}\rho_1 + (1 - \psi_{cv})\rho_2 \quad (4.3)$$

$$\mu_{cv} = \psi_{cv}\mu_1 + (1 - \psi_{cv})\mu_2, \quad (4.4)$$

with the control volume volume fraction ψ_{cv} given by

$$\psi_{cv} = 1/V_{cv} \int_{V_{cv}} H(G) dV. \quad (4.5)$$

Here V_{cv} is the volume of the control volume.

In the *ConsistentRescaledMomentumTransport* (CRMT) method, instead of relying on the level set solution to transport mass, we first solve the continuity equation, (3.4). In discrete form this results in

$$V_{cv} \frac{\rho_{cv}^* - \rho_{cv}^n}{\Delta t} + \sum_f u_f^n \rho'_f A_f = 0, \quad (4.6)$$

where A_f is the cell face area, u_f^n is the face normal velocity, and ρ_{cv}^n is calculated from (4.3) and (4.5) using the level set solution at time t^n . In (4.6), ρ'_f is defined as

$$\rho'_f = \begin{cases} \rho_{Upwind}^n & \epsilon < \psi_{cv} < 1 - \epsilon \quad \text{or} \quad \epsilon < \psi_{nbr} < 1 - \epsilon \\ \frac{\rho_{cv}^n + \rho_{nbr}^n}{2} & \text{elsewhere} \end{cases}. \quad (4.7)$$

Here ϵ is a small number, the index *nbr* denotes the neighbor control volume to *cv* sharing the same face, and ρ_{Upwind}^n is calculated using a simple first-order upwind approach,

$$\rho_{Upwind}^n = \begin{cases} \rho_{cv}^n & u_f \geq 0 \\ \rho_{nbr}^n & u_f < 0. \end{cases} \quad (4.8)$$

The reason for using a simple first-order approach here lies in the fact that this will guarantee boundedness of ρ_{cv}^* , provided the face normal velocities u_f^n are discretely divergence free. The choice of ρ_f' away from the phase interface in (4.7) is dictated by the discrete operator for the momentum equation away from the interface described below and does not result in an unconditionally unstable method for (4.6), since away from the phase interface $\rho_{cv}^n = \rho_{nbr}^n$.

To conserve momentum discretely, we choose the conservative form of the Navier-Stokes equations. The discrete form of the conservative Navier-Stokes equations on collocated unstructured meshes reads

$$V_{cv} \frac{(\rho u)_{i,cv}^* - (\rho u)_{i,cv}^n}{\Delta t} + \sum_f u_f^n (\rho u)_{i,f}' A_f = \sum_f A_f \mu_f ((\nabla u)_{i,f} + (\nabla u)_{i,f}^T) + V_{cv} \rho_{cv}^n g_i + V_{cv} \rho_{cv}^n F_{i,cv}^n, \quad (4.9)$$

where $F_{i,cv}^n$ is a surface tension force induced acceleration, the subindex i indicates a spatial direction, $\mu_f = \frac{\mu_{cv} + \mu_{nbr}}{2}$, and $(\rho u)_{i,cv}^n = \rho_{cv}^n u_{i,cv}^n$.

To ensure discrete consistency with (4.6), $(\rho u)_{i,f}'$ in (4.9) is defined as

$$(\rho u)_{i,f}' = \begin{cases} (\rho u)_{i,U_{pwind}}^n & \epsilon < \psi_{cv} < 1 - \epsilon \quad \text{or} \quad \epsilon < \psi_{nbr} < 1 - \epsilon \\ \frac{(\rho u)_{i,cv}^n + (\rho u)_{i,nbr}^n}{2} & \text{elsewhere} \end{cases}. \quad (4.10)$$

with $(\rho u)_{i,U_{pwind}}^n$ calculated using the first-order upwind scheme

$$(\rho u)_{i,U_{pwind}}^n = \begin{cases} (\rho u)_{i,cv}^n & u_f \geq 0 \\ (\rho u)_{i,nbr}^n & u_f < 0 \end{cases}. \quad (4.11)$$

This ensures that the resulting method is discretely energy conserving away from the phase interface and discretely identical to the continuity equation which is the key point in this method.

To calculate $F_{i,cv}^n$ in (4.9), we follow the balanced force approach for collocated, finite volume methods [7]. At the cell face, the surface tension force is

$$T_{\sigma_f}^n = \sigma \kappa_f^n (\nabla \psi)_f^n, \quad (4.12)$$

resulting in

$$F_f^n = T_{\sigma_f}^n / \rho_f^n, \quad (4.13)$$

with $\rho_f^n = \frac{(\rho_{cv}^n + \rho_{nbr}^n)}{2}$. To ensure discrete consistency between the surface tension force at the control volume centroid and the pressure gradient evaluated there, $F_{i,cv}^n$ is calculated from F_f^n using a face-area weighted least-squares method [29] by minimizing

$$\epsilon_{cv} = \sum_f (F_{i,cv}^n n_{i,f} - F_f^n)^2 A_f, \quad (4.14)$$

where $n_{i,f}$ is the face normal vector.

Using the solutions to (4.9) and (4.6), $(\rho u)_{i,cv}^*$ and ρ_{cv}^* , we can then calculate the predicted velocity,

$$u_{i,cv}^* = \frac{(\rho u)_{i,cv}^*}{\rho_{cv}^*}. \quad (4.15)$$

Next, we project the predicted velocity field $u_{i,cv}^*$ into the subspace of divergence free velocity fields, by first solving the pressure Poisson equation

$$\nabla \cdot \left(\frac{1}{\rho^n} \nabla p \right) = \frac{1}{\Delta t} \nabla \cdot \mathbf{u}^* \quad (4.16)$$

which in discrete form is

$$\sum_f \frac{1}{\rho_f^n} \frac{\partial p_{cv}}{\partial n} A_f = \frac{1}{\Delta t} \sum_f u_f^* A_f, \quad (4.17)$$

with

$$u_f^* = \frac{1}{2} (u_{i,cv}^* + u_{i,nbr}^*) n_{i,f} - \frac{1}{2} \Delta t (F_{i,cv}^n + F_{i,nbr}^n) n_{i,f} + \Delta t F_f^n. \quad (4.18)$$

The projection, i.e. correction step is then

$$\mathbf{u}^{n+1} = \mathbf{u}^* - \frac{\Delta t}{\rho^n} \nabla p \quad (4.19)$$

which for the face velocities in discrete form is

$$u_f^{n+1} = u_f^* - \Delta t P_f, \quad (4.20)$$

with

$$P_f = \frac{1}{\rho_f^n} (\nabla p_{cv}^n)_f = \frac{1}{\rho_f^n} \frac{p_{nbr}^n - p_{cv}^n}{|\mathbf{s}_{cv,nbr}|}. \quad (4.21)$$

Here, $\mathbf{s}_{cv,nbr}$ is the vector connecting the cv and nbr control volume centroids.

To correct the control volume velocities, first the control volume centroid-based density weighted pressure gradient P_{cv} is calculated from the face-based density weighted gradient P_f using the same face-area weighted least-squares method employed in calculating F_f , see (4.14),

$$\epsilon_{cv} = \sum_f (P_{i,cv} n_{i,f} - P_f)^2 A_f. \quad (4.22)$$

Then, the control volume centroid velocity is corrected as

$$u_{i,cv}^{n+1} = u_{i,cv}^* - \Delta t P_{i,cv}. \quad (4.23)$$

Finally, we discard the solution to the continuity equation, ρ^* , and reset the density at t^{n+1} using the level set solution G^{n+1} obtained from solving the level set equation (3.6), as

$$\rho_{cv}^{n+1} = \psi_{cv}^{n+1} \rho_1 + (1 - \psi_{cv}^{n+1}) \rho_2 \quad (4.24)$$

This density is then used to update the momentum as

$$(\rho u)_{i,cv}^{n+1} = \rho_{cv}^{n+1} u_{i,cv}^{n+1}. \quad (4.25)$$

4.0.3 Coupling to Lagrangian spray model

Numerical simulations of jet in crossflow atomization can easily lead into the generation of millions of drops over a large distance from the nozzle exit. Having a fine level

set mesh in the vicinity of the interface of those droplets is extremely expensive. So it is more efficient to replace the small drops and structures with Lagrangian drops in our simulations. Since small drops have strong We numbers that keeps their shape close to sphere, it is reasonable to assume the Lagrangian drops having spherical shape. Drop transfer is initiated if a separated liquid structure has a liquid volume

$$V_D \leq V_{trans} \quad (4.26)$$

and its shape is nearly spherical,

$$r_{max} \leq \alpha \left(\frac{3}{4\pi} V_D \right)^{1/3} \quad (4.27)$$

with typically $\alpha = 2$ and r_{max} the maximum distance of the liquid structures surface to its center of mass. In the Lagrangian description, two-way momentum coupling of the drag force acting on the drop and the continuous phase is used, including a high Reynolds number correction for large relative velocities [30]. However, finite volume effects are not included, i.e. it is implicitly assumed that the drop volume is smaller than the flow solver volume and the point particle assumption is valid. Furthermore, neither drop/drop nor drop/tracked phase interface collisions are modeled. But, as long as liquid structures have not been transferred into the Lagrangian description, i.e. they are still tracked by the level set scalar, cell volume effects, and all collisions between level set tracked liquid structures are fully captured.

Secondary atomization is accounted for by using the stochastic secondary atomization model of Apte & Gorokhovski [30]. A detailed description of both the two-way momentum coupling and the stochastic secondary atomization model can be found in [30].

Chapter 5

Verification

Verification and validation are essential in computational fluid dynamics. Verification is essentially a mathematical exercise and answers the question: Are the equations being solved correctly? Validation answers the question: Are the correct equations being solved? In other words, verification provides evidence that the computational model is solved correctly and accurately, while validation provides evidence that the mathematical model accurately relates to experimental measurements [32]. For the verification of the new method, we performed different test cases with large fluid to gas density ratios. In all cases, the position of the phase interface is captured using the Refined Level Set Grid method [7] and the flow solver uses the *CRMT* method to handle high density ratios.

Collapse of a Water Column

A 2D water column with initial height and width of $h=5.715$ cm is placed inside a container of size 40×10 cm as shown in Fig. 5.1. The density of the water and air are $\rho_l = 1000$ kg/m³, respective $\rho_g = 1.226$ kg/m³, the viscosities are $\mu_l = 1.137 \times 10^{-3}$ kg/ms, respective $\mu_g = 1.78 \times 10^{-5}$ kg/ms, the surface tension coefficient is $\sigma = 0.0728$ N/m, and the gravitational acceleration is $g = -9.81$ m/s².

Figure 5.1 shows the phase interface shape at $\Delta t = 0.1$ s, time intervals obtained using the CRMT method compared to the shape obtained using a standard non-conservative method [7]. The non-conservative method shows significantly slower lateral spread of the water column and some unphysical deformations of the phase interface as compared to the results of the CRMT method. The CRMT results are comparable to the improvements reported using the method of Raessi [18] and Raessi & Pitsch [19].

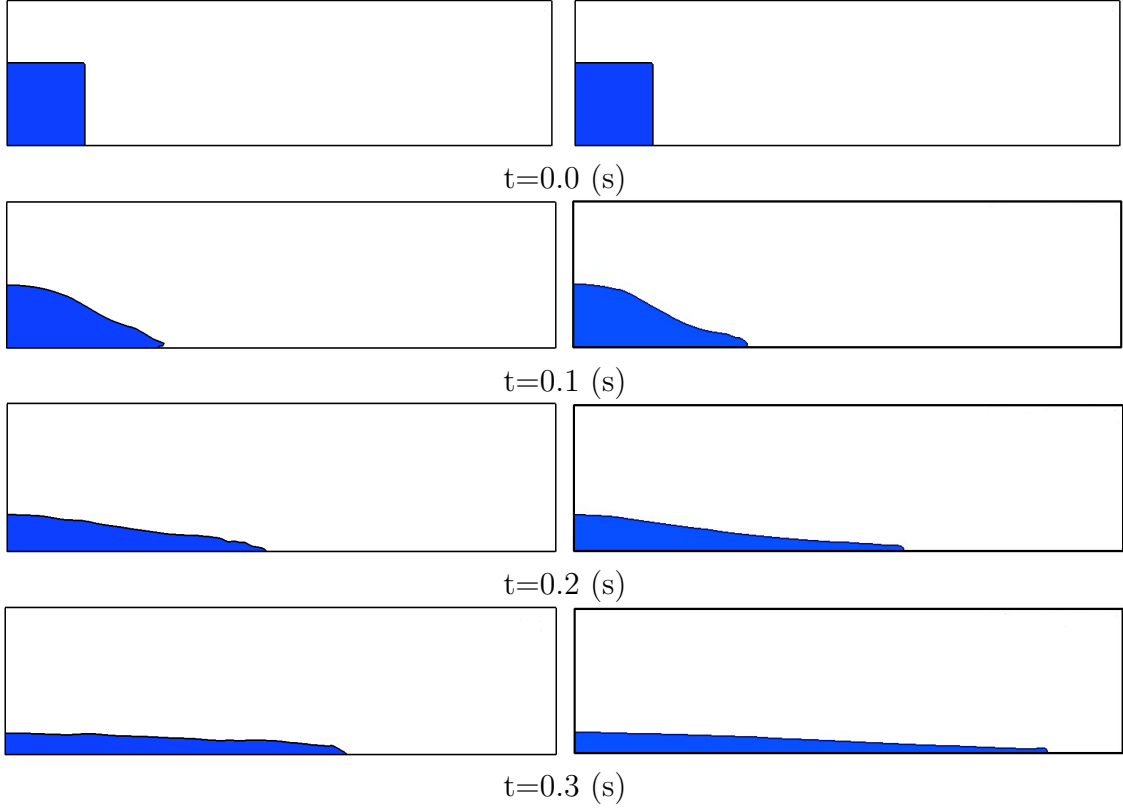


Figure 5.1: Qualitative comparison of dam-break results with density ratio 815, using non- method (left) and CRMT method (right) with no-slip boundary condition on the horizontal wall.

The non-dimensional front position and non-dimensional height of the water column as a function of non-dimensional time are shown in Fig. 5.2, where reference length is h and the reference time is $\sqrt{\frac{h}{g}}$. Figure 5.2 also shows the results of a grid refinement study resolving the container by 512×128 , 1024×256 , and 2048×512 equi-sized hexahedral control volumes. The lateral front position converges under grid refinement, and the results are in good agreement with spread rate observed experimentally [6], especially for the last point of the experimental data. The height of the water column is also well captured even on the coarsest mesh.

Table 5.1 shows both the order of convergence for the relative error of the front position (Z) with respect to the experimental data, $E_{exp} = \frac{Z_{exp} - Z}{Z_{exp}}$ and with respect

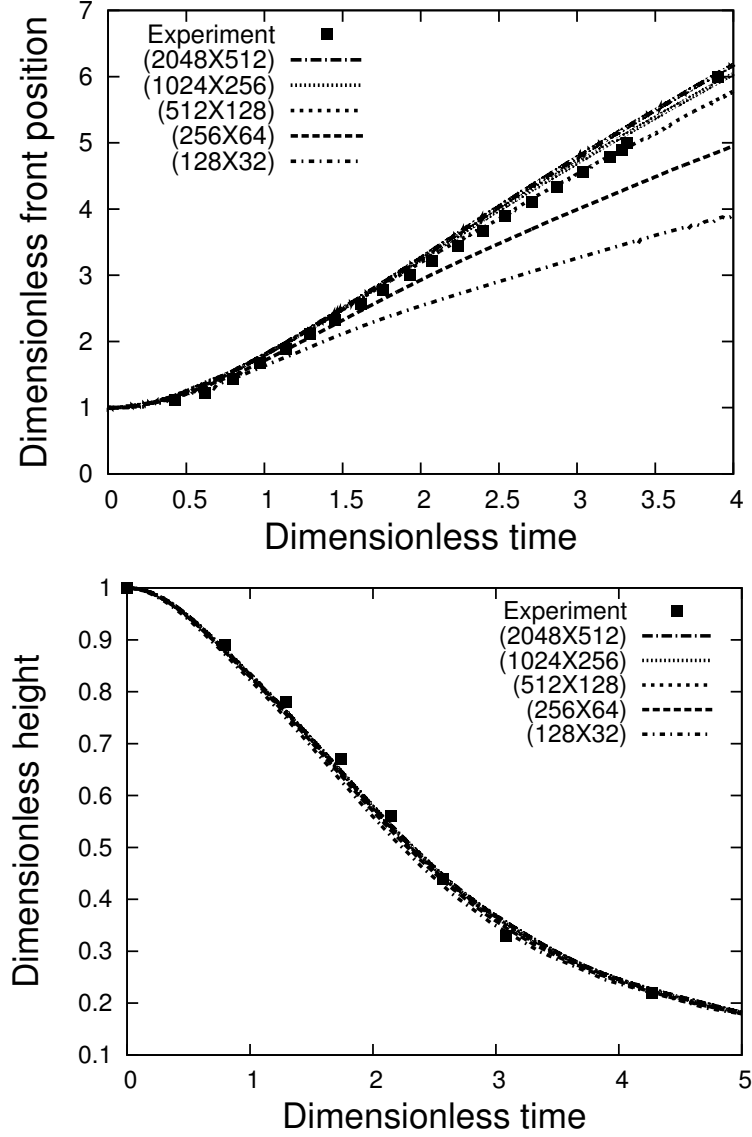


Figure 5.2: Non-dimensional front position (top) and non-dimensional height of water column (bottom) of dam-break versus non-dimensional time compared to the experimental results [6]

to the finest grid solution, $E_{finest} = \frac{Z_{finest} - Z}{Z_{finest}}$ at time $t = 3.9$.

Damped surface wave

The dynamics of a small amplitude damped surface wave between two superposed immiscible fluids are described by the initial value theory of Prosperetti [33]. The

Grid	E_{exp}	order	E_{finest}	order
128X32	0.356	-	0.360	-
256X64	0.190	0.90	0.195	0.88
512X128	0.058	1.71	0.064	1.60
1024X256	0.015	1.95	0.021	1.60
2048X512	0.006	1.32	-	-

Table 5.1: Error of the front position in the collapse of the water column.

initial surface position inside a $[0, 2\pi] \times [0, 2\pi]$ box is given by a sinusoidal disturbance of wavelength $\lambda = 2\pi$ and amplitude $A_0 = 0.01\lambda$,

$$G(vx, t = 0) = y - y_0 + A_0 \cos(x - h_G/2) , \quad (5.1)$$

with $y_0 = \pi$. Periodic boundary conditions are used in the x -direction and slip walls are imposed in the y -direction. The initial value solution for two fluids with equal kinematic viscosity ν and $\lambda = 2\pi$ can be written as [33]

$$A_{ex}(t) = \frac{4(1 - 4\beta)\nu^2}{8(1 - 4\beta)\nu^2 + \omega_0^2} A_0 \operatorname{erfc}\sqrt{\nu t} + \sum_{i=1}^4 \frac{z_i}{Z_i} \left(\frac{\omega_0^2 A_0}{z_i^2 - \nu} \right) \exp[(z_i^2 - \nu)t] \operatorname{erfc}(z_i \sqrt{t}) , \quad (5.2)$$

where z_i are the roots of

$$z^4 - 4\beta\sqrt{\nu}z^3 + 2(1 - 6\beta)\nu z^2 + 4(1 - 3\beta)\nu^{3/2}z + (1 - 4\beta)\nu^2 + \omega_0^2 = 0 , \quad (5.3)$$

the dimensionless parameter β is given by $\beta = \rho_1\rho_2/(\rho_1 + \rho_2)^2$, the inviscid oscillation frequency is $\omega_0 = \sqrt{\frac{\sigma}{\rho_1 + \rho_2}}$, and $Z_i = \prod_{\substack{j=1 \\ j \neq i}}^4 (z_j - z_i)$. In [7] results for $\rho_l = 1000$, $\rho_g = 1$, $\sigma = 2$ and $\nu_l = \nu_g = 0.064720863$ were reported using the non-conservative formulation.

Figure 5.3 shows the temporal evolution of the non-dimensional disturbance amplitude A for a mesh consisting of 128x128 equi-sized hexahedra using both the CRMT and non-conservative method [7], including a zoom of the temporal evolution

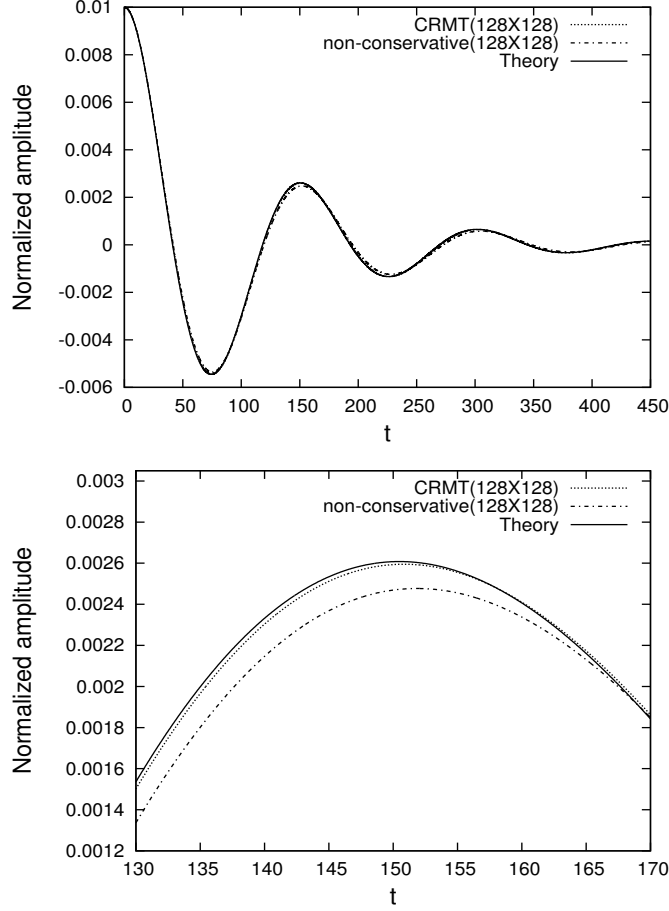


Figure 5.3: Normalized amplitude(A/λ) of damped surface wave with density ratio 1000 versus time.

starting at $t = 130$ to more clearly see the difference in results. The CRMT method shows noticeably improved results compared to the non-conservative methods.

Figure 5.4 shows the results of a grid refinement study in a zoom of the temporal evolution starting at $t = 130$. Excellent agreement of the CRMT method with the analytical results can be seen. Figure 5.5 shows the evolution of the corresponding non-dimensional error $E(t) = (A(t) - A_{ex}(t))/A_0$ for hexadral and prism meshes, while Tab. 5.2 summarizes their root mean squares. At the same grid resolution, the CRMT method shows a significantly lower error as compared to the standard non-conservative formulation [7]. The errors of the front position with respect to

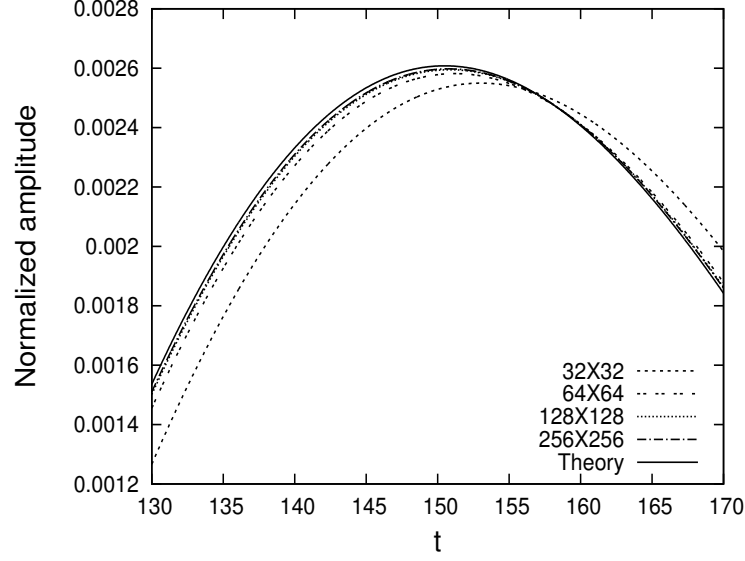


Figure 5.4: Normalized amplitude(A/λ) of damped surface wave with density ratio 1000 versus time using CRMT method.

the exact solution suggest that results are converging to a slightly different solution, which can be due to the fact that boundary conditions in the analytical solution is assumed to be infinite, while we have truncated the domain in our simulations.

	CRMT	Ref [7]
Cartesian Mesh		
32	1.440E-002	4.82E-002
64	4.534E-003	2.08E-002
128	2.465E-003	1.27E-002
256	2.246E-003	1.18E-002
Prism Mesh		
32	1.263E-002	5.64E-002
64	6.743E-003	1.41E-002
128	6.188E-003	1.13E-002
256	4.703E-003	1.57E-002

Table 5.2: Rms of amplitude error for damped surface wave.

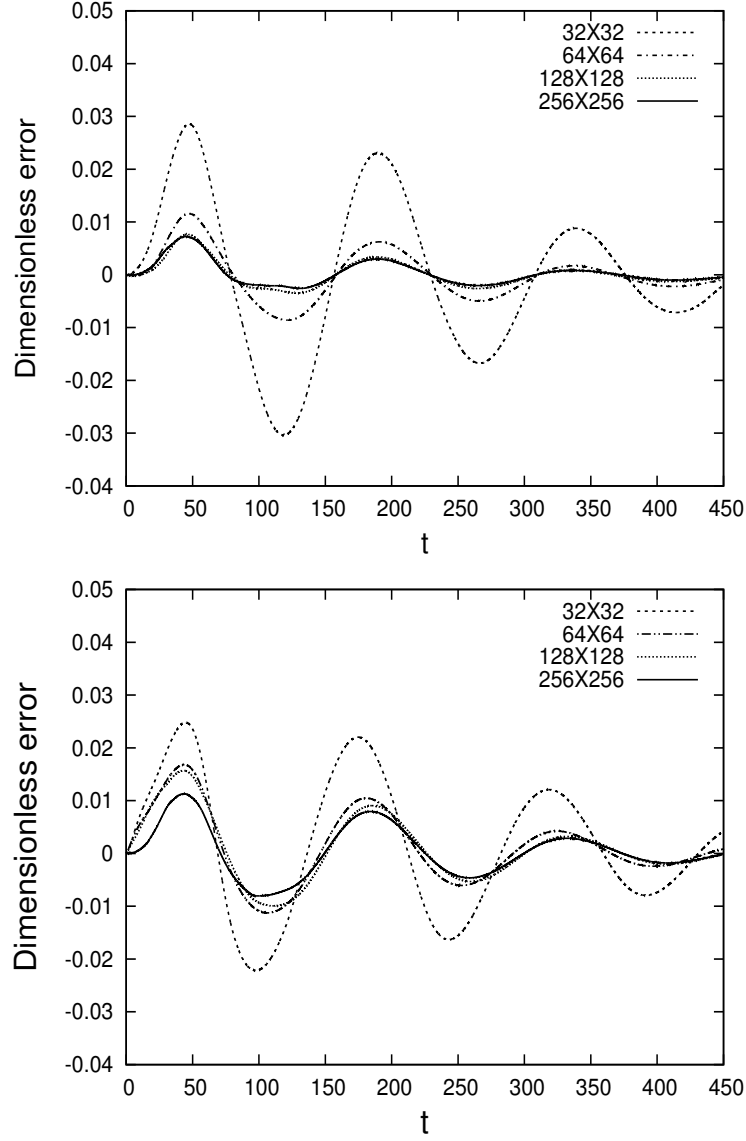


Figure 5.5: Amplitude error E of damped surface wave for hexahedral (top) and prism (bottom) meshes using CRMT method.

Zero gravity column oscillation

To further verify the implementation of the new method, this section presents results for zero gravity oscillating columns. The theoretical oscillation period for columns in

the linear regime is given by [2]

$$\omega^2 = \frac{n(n^2 - 1)\sigma}{(\rho_1 + \rho_2)R_0^3}. \quad (5.4)$$

In all simulations, a column of radius $R_0 = 2$ is placed in the center of a $[-10, 10]$ square box with periodic boundary conditions on all sides and $\sigma = 1$, $\rho_1 = 1$, $\rho_2 = 0.01$, $\mu_1 = 0.01$, and $\mu_2 = 1 \cdot 10^{-4}$, resulting in a Laplace number of $\text{La} = 20000$. The column is initially perturbed by a mode $n = 2$ perturbation with an initial amplitude of $A_0 = 0.01R_0$. The time step size in all simulations is chosen as $\Delta t = 0.5\Delta t_{cap}$. Where

$$t_{cap} = \sqrt{\frac{(\rho_1 + \rho_2)h^3}{4\pi\sigma}}. \quad (5.5)$$

Table 5.3 shows the period of oscillation error $E_T = |T_{calc}\omega/2\pi - 1|$ for the oscillating column together with the results reported in [7]. On fine hexahedral meshes, the CRMT method gives noticeably improved results as compared to those of the non-conservative method, whereas the results on prism meshes are comparable.

grid size	E_T hexadra	Ref. [7]	E_T prism	Ref [7]
20/64	7.47e-2	4.04e-2	5.66e-2	5.91e-2
20/128	7.32e-3	1.05e-2	1.61e-2	1.65e-2
20/256	3.44e-4	3.7e-3	1.35e-2	1.36e-2

Table 5.3: Zero gravity 2D column oscillation. Error in oscillation period as compared to linear theory [2].

Convection of high density droplet

In this test case initially proposed by Bussman et al. [34], a 2D liquid droplet of diameter $D = 0.4$ is placed in the center of a 1×1 periodic domain filled with gas. The density ratio is chosen as $\rho_l/\rho_g = 10^6$ and the fluids are assumed inviscid and without surface tension. The drop is given an initial homogeneous velocity of $\mathbf{u} = (1, 0)$ while the gas is initially at rest. We have employed different structured

equi-sized hexahedral and unstructured prism grids. Because of the large inertia, the drop should stay essentially undeformed while passing through the computational domain multiple times.



Figure 5.6: Droplet shape after one passthrough using non-conservative method [7].

Figure 5.6 shows the drop shape after passing the domain once ($t \approx 1$) using the non-conservative method [7] on a 128×128 hexahedral mesh. Erroneous transfer of momentum from the liquid to the gas has caused significant interface deformation, resulting in an unphysical shattering of the drop unbounded velocities. Figure 5.7 shows the drop shape after passing the entire domain once ($t = 1$) obtained using the CRMT method together with the expected solution for varying mesh resolutions and Tab. 5.4 summarizes the corresponding shape errors. While there are some minor deformations of the drop visible, the drop stays nearly spherical and no erroneous large scale interface deformations are visible. Errors in the simulations with hexahedra mesh are slightly higher compared to the prism mesh due to the fact that, there is a symmetric distribution of errors while resolving a spherical shape with hexahedra mesh, which is not the case when prism mesh is used.

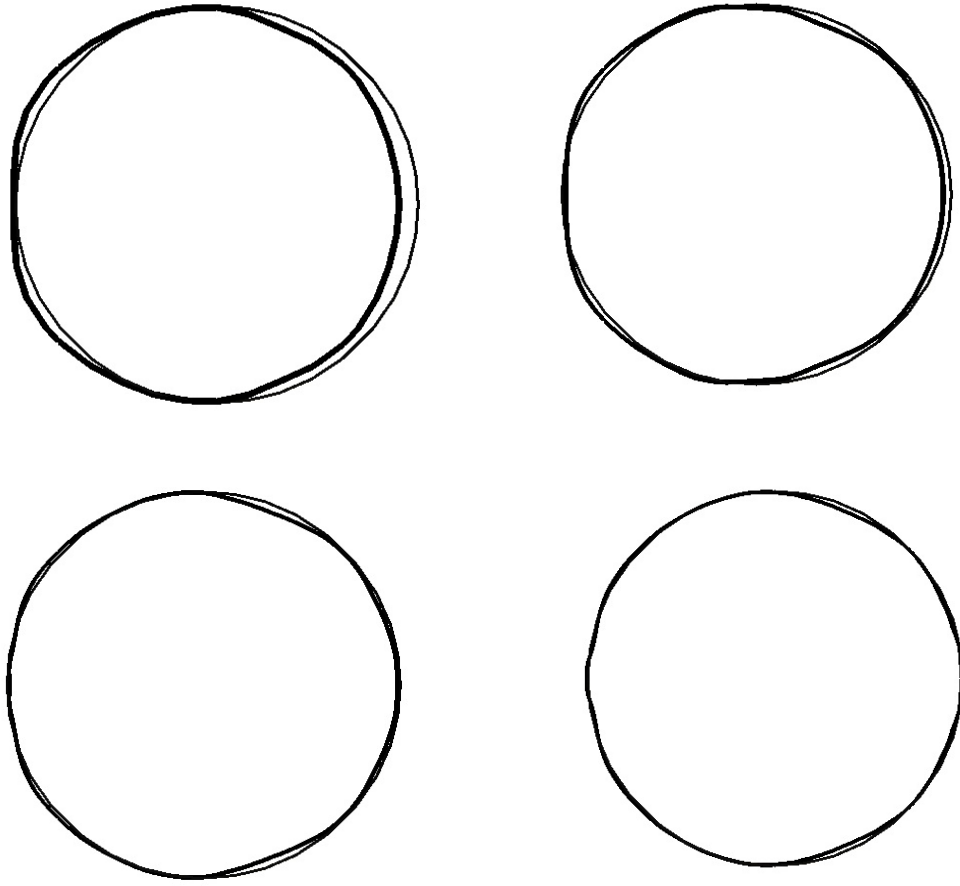


Figure 5.7: Droplet shape after one passthrough ($t = 1.0$) using CRMT method on hexahedral meshes. Thick lines are for numerical solutions and fine lines are the expected solution.

grid size	E_T (hexahedra)	order	E_T (prism)	order
1/32	5.33e-3	-	5.42e-3	-
1/64	3.73e-3	0.51	2.93e-3	0.88
1/128	2.64e-3	0.49	1.65e-3	0.82
1/256	1.85e-3	0.51	-	-

Table 5.4: Shape errors for convection of high density droplet.

We now have a method that enables us to perform numerical simulations of jet in crossflow atomization with large density ratio.

Chapter 6

Impact of Boundary Conditions On Jet in Crossflow Atomization

One of the problems in studying the jet in crossflow atomization is that the boundary condition used in experimental studies is not fully defined. This can lead completely different results from numerical simulations performed based on one experimental study. In this section it will be showed how using different numerical boundary conditions can produce totally different results while all have same nominal characteristic numbers.

Computational Domain and Operating Conditions

Detailed numerical simulations of jet in crossflow atomization with high density ratio were performed for different cases based on the experimental study by Brown & McDonell [1]. Table 6.1 summarizes the operating conditions and resulting characteristic numbers.

jet exit diameter D [mm]	1.3
crossflow density ρ_c [kg/m ³]	1.225
jet density ρ_j [kg/m ³]	1000
crossflow velocity u_c [m/s]	120.4
jet velocity u_j [m/s]	10.83
crossflow viscosity μ_c [kg/ms]	1.82e-5
jet viscosity μ_j [kg/ms]	1.0e-3
surface tension coeff. σ [N/m]	0.07
momentum flux ration q	6.6
crossflow Weber number We_c	330
jet Weber number We_j	2178
crossflow Reynolds number Re_c	5.7e5
jet Reynolds number Re_j	14079

Table 6.1: Operating conditions and characteristic numbers [1].

Figure 6.1 depicts the computational domain and the used boundary conditions as well as a zoom into the near-injector region to show the mesh detail used

in the simulations. The chosen computational domain is $(-25D \dots 50D \times 0 \dots 25D \times -10D \dots 10D)$ is smaller than the channel used in the experiment $(-77D \dots 127D \times 0 \dots 54D \times -27D \dots 27D)$ where D is the nondimensional diameter of the jet exit. However, simulations using the full experimental channel geometry were conducted to verify that the reduced computational domain does not impact the reported results [8].

The injector geometry used in the experiments consists of a long initial pipe section of diameter 7.49mm, followed by an 138° angled taper section, followed by a short pipe section of diameter D with $L/D = 4$, whose exit is mounted flush with the lower channel wall. The flow solver grid consists of hexahedra of edge length $D/4$, which are isotropically refined in layers near the injector and lower channel walls, such that the spatial region where the phase interface is tracked is completely filled with equidistant grid cells of the minimum cell size $\Delta x = D/32$. Note that, the G-grid is a factor 2 finer than the flow solver grid in order to enhance numerical accuracy of the interface tracking scheme. At $t = 0$, the liquid jet is initialized in the computational domain by a small cylindrical section of length D capped by a half-sphere, protruding into the crossflow channel. For more detail see [8].

The inflow gas is assumed fully developed and a mean channel flow velocity distribution is assigned to it. In order to investigate the impact of the nozzle geometry and turbulence in the velocity of the liquid inflow, different jet in crossflow simulations are performed using the following jet inflow velocity profiles:

Database including nozzle geometry :

To account for their effect in the atomization simulations, detailed single phase Large Eddy Simulations (LES) of the pre-taper pipe, the taper, the post-taper pipe, and the cross flow channel in the vicinity of the injector exit were performed using a

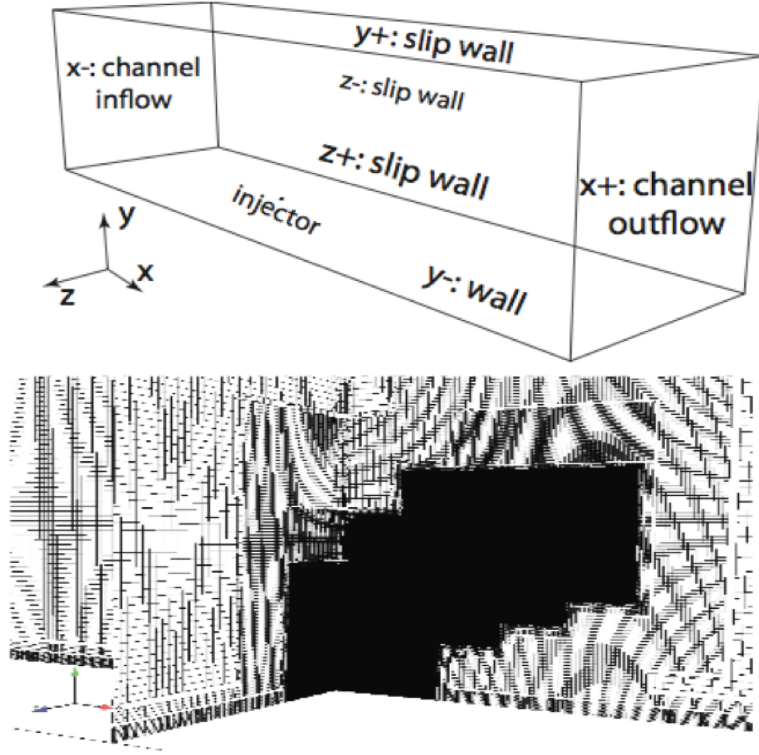


Figure 6.1: Computational domain and boundary conditions (top) and mesh detail near the injector (bottom) [8].

dynamic Smagorinsky model. The channel section was included in these simulations to capture the effect of the cross flow on the injector exit plane velocity distribution. Inflow boundary conditions for the pre-taper pipe were taken from a pre-computed LES pipe flow simulation database at the appropriate Reynolds number. The injector exit plane velocity distributions were then stored as a time sequence in a database to be used in the subsequent two-phase atomization simulations [8]. Figure 6.2 shows the velocity distribution in the nozzle and how it is effected by the crossflow. Figure 6.3 also shows how velocities that are stored in the database are shifted toward the downstream direction due to the effects of the crossflow.

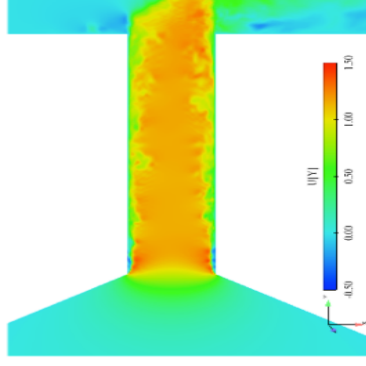


Figure 6.2: Velocity distribution in the nozzle from the single phase LES simulation [8].

Averaged database including nozzle geometry :

The inflow database described in the above section is averaged over time in order to neglect the effect of turbulence in the liquid inflow. This averaged velocity profile is used for all the timesteps of the two-phase simulation of the atomization. From figure 6.3 it can be seen that there is no turbulence in the averaged database velocity distribution but the mean velocity still is shifted due to the crossflow gas.

Turbulent pipe flow database:

In order to neglect the effect of the cross flow on the injector exit flow, a LES pipe flow simulation with the appropriate Reynolds number is performed for a single pipe with the diameter of the post-taper pipe of the actual nozzle to generate this database.

Rotated database:

Since the channel cross flow clearly has an impact on the distribution of the jet direction velocity, to study this effect further, the database including the nozzle geometry is rotated 180° around the nozzle axis. This means that the velocities are shifted toward the upwind direction and liquid is pushed more the incoming cross

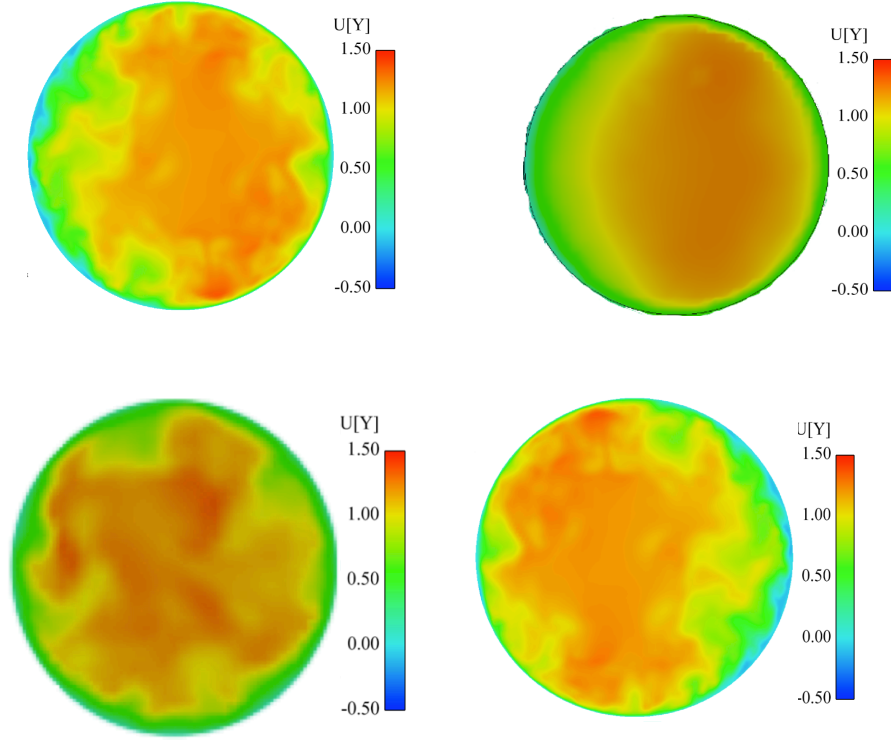


Figure 6.3: Instantaneous injector exit plane velocity distributions in axial direction from: database including nozzle geometry(left-top) [8], averaged database including nozzle geometry(right-top), turbulent pipe flow databas(bottom-left) and rotated database(bottom-right). Gas crossflow is from left to right.

flow. Figure 6.3 shows the instantaneous injector exit plane velocity distributions in the axial direction for all four velocity profiles used as jet inflow boundary conditions.

The key point in using above boundary conditions is that since the mean averaged velocities over the surface area of the injector are the same, they all have the same nominal momentum flux ratio, they all have different velocity distributions specifically on the upwind direction of the injector, giving different local momentum flux ratios.

Results and Discussion

We initially perform simulations with density ratio $r=100$ which is a realistic density ratio for gas turbine applications, keeping all other nondimensional parameters in table 6.1 the same. Figures 6.4 and 6.5 show snapshots of the atomizing jets at time 20, using all four boundary conditions including the Lagrangian drops generated from the breakup of the ligaments and larger structures.

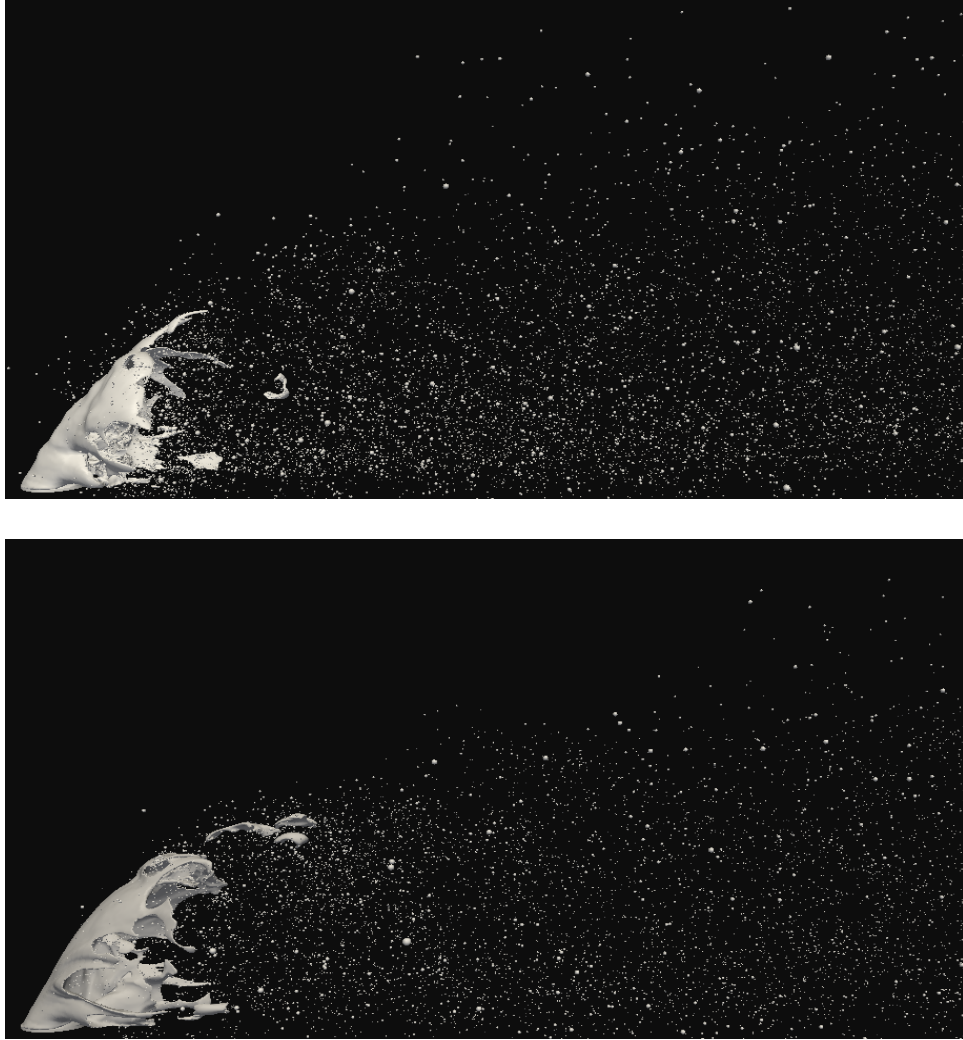


Figure 6.4: Side view snapshots of jet in crossflow atomization using database(top) and data base average (bottom)

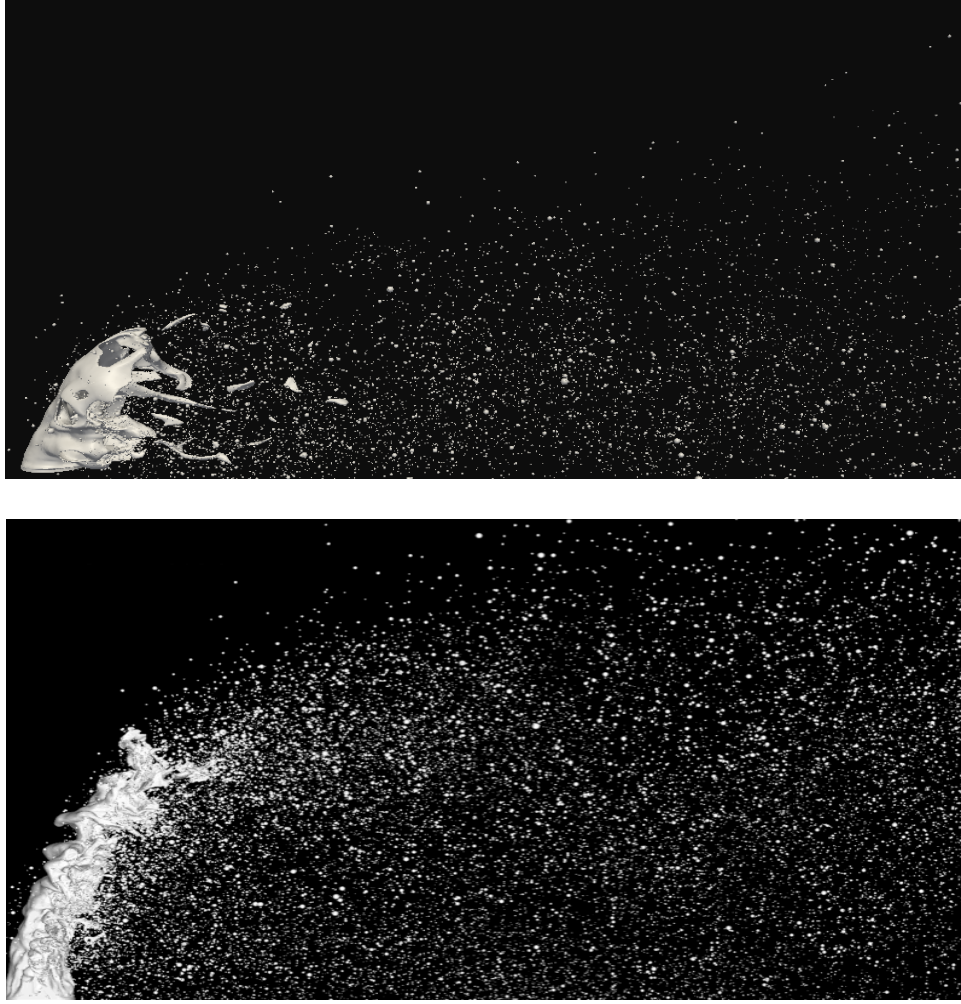


Figure 6.5: Side view snapshots of jet in crossflow atomization using pipe flow(top) and rotated data base(bottom)

First results from the simulations using time resolved unsteady database and its averaged are compared. Figures 6.6 and 6.7 show snapshots of the atomizing jets next to each other. Turbulences in the inflow jet has a slight effect on the instabilities on the jet interface and triggers some instabilities that grow along the jet penetration in the simulation using the unsteady database, while results from the averaged database show smoother interface, stretching more toward the sides of the jet and forming thinner ligaments. So results suggest that at this mesh resolution turbulence in the injected jet has a slight impact on the generation of instabilities.

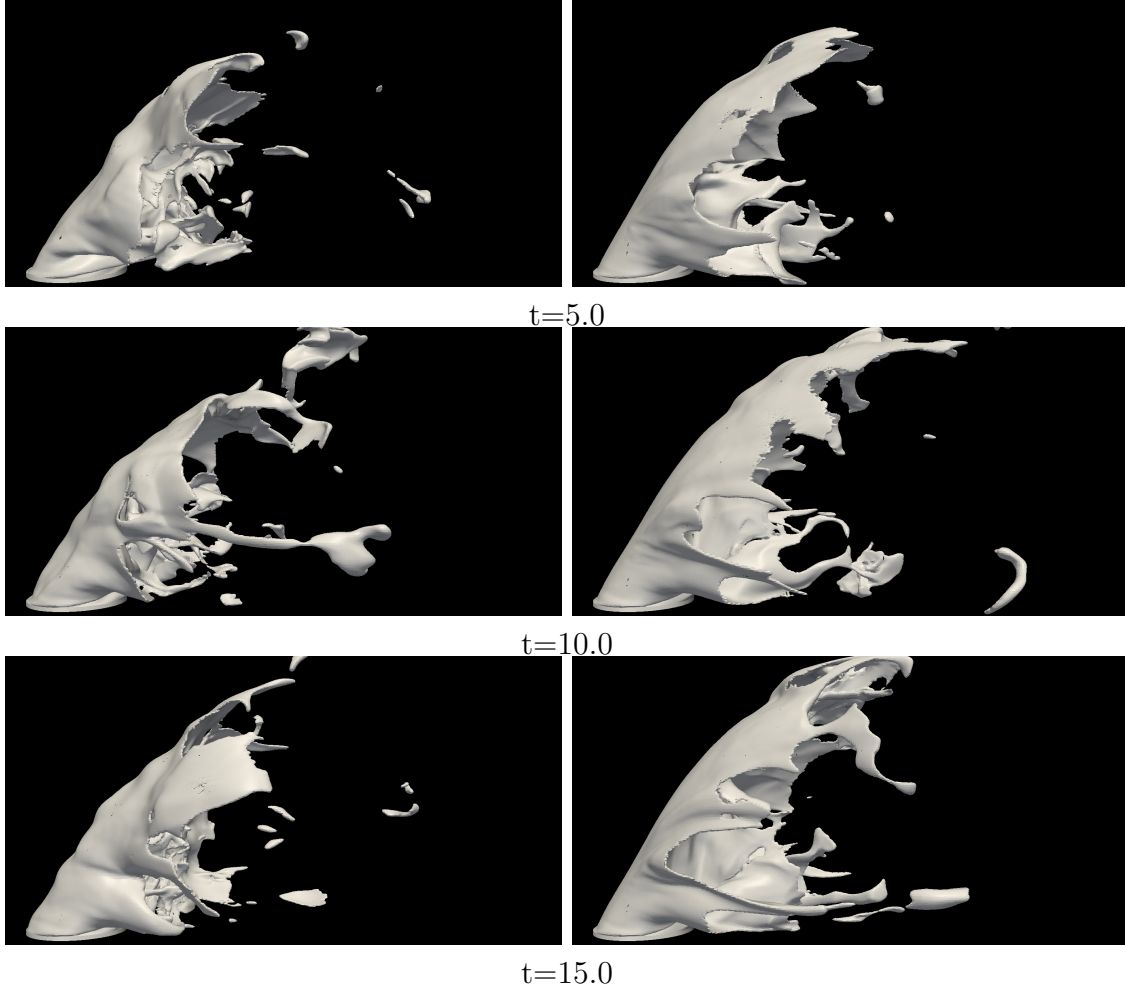


Figure 6.6: Side view snapshots of jet in crossflow atomization with density ratio $r=100$ at $t=5, 10, 15$ time units (top to bottom), using data base (left) and data base averaged (right).

Figure 6.8 shows different averaged normal cross sections of the jet for different distances from the bottom wall resulted from above mentioned simulations. Volume of Fluid scalar (VOF) calculated in eq. 4.5 is averaged over time for different cross sections and probability isoline of $VOF=0.5$ is used as averaged normal cross sections. It can be noticed again in this figure that in the simulation using time resolved unsteady database, ligaments and drops cut faster from the sides of the jet, leaving a smaller cross section area compared to the simulation using the time averaged database, where the liquid column stretches toward the sides, forming thin ligaments.

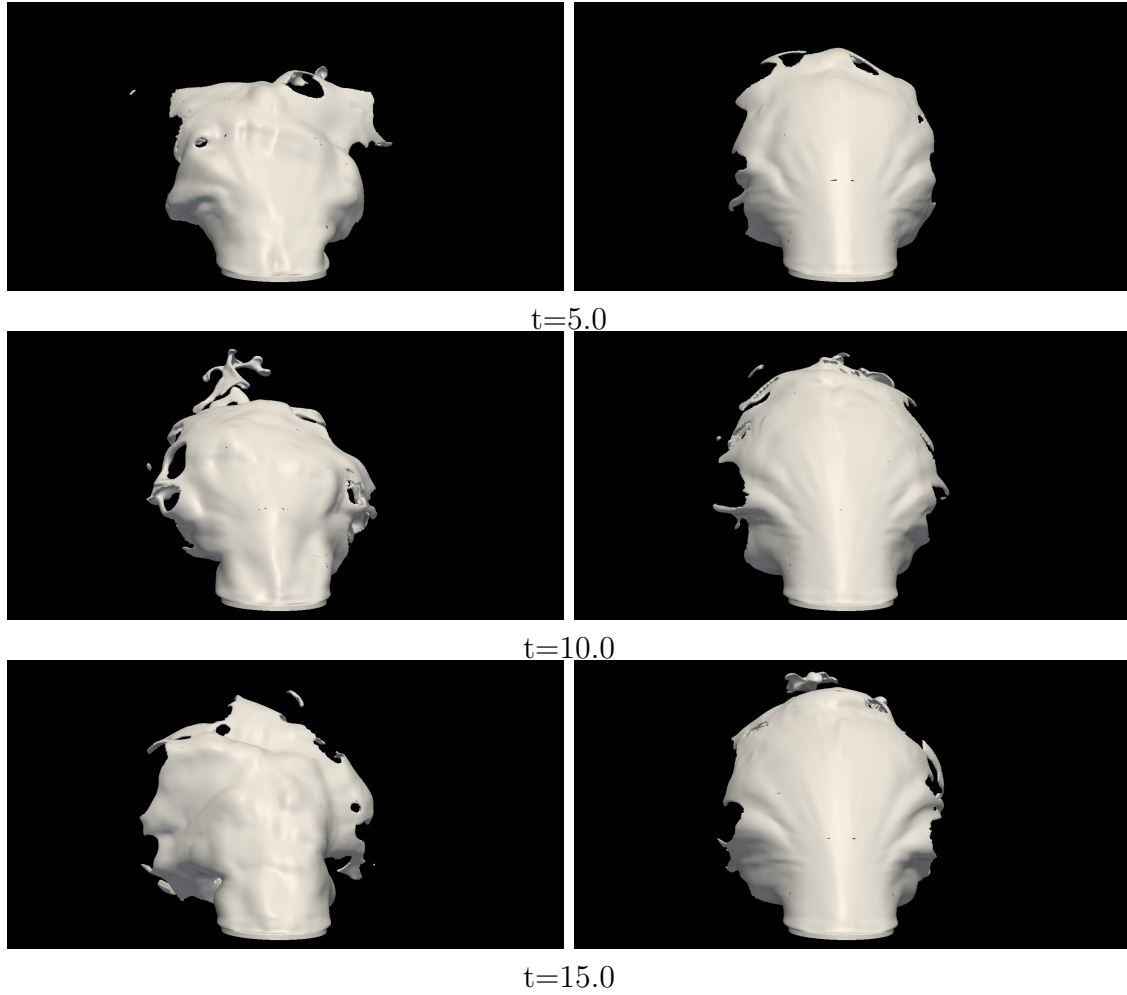


Figure 6.7: Front view snapshots of jet in crossflow atomization with density ratio $r=100$ at $t=5, 10, 15$ time units (top to bottom), using data base (left) and data base averaged (right).

Figure 6.9 shows drop size distribution suggesting the similarity of these simulations. Note that size distribution is calculated only for the transferred Lagrangian drops from the small structures cut from liquid jet. Since structures smaller than the level set solver mesh size are under resolved, drop size distribution only includes drops with the size larger than G-grid.

Next we compare results from the simulation using the time resolved unsteady database with the simulation using the pipe flow database. Figures 6.11 and 6.12 show snapshots of the atomizing jets using these two boundary conditions. In the

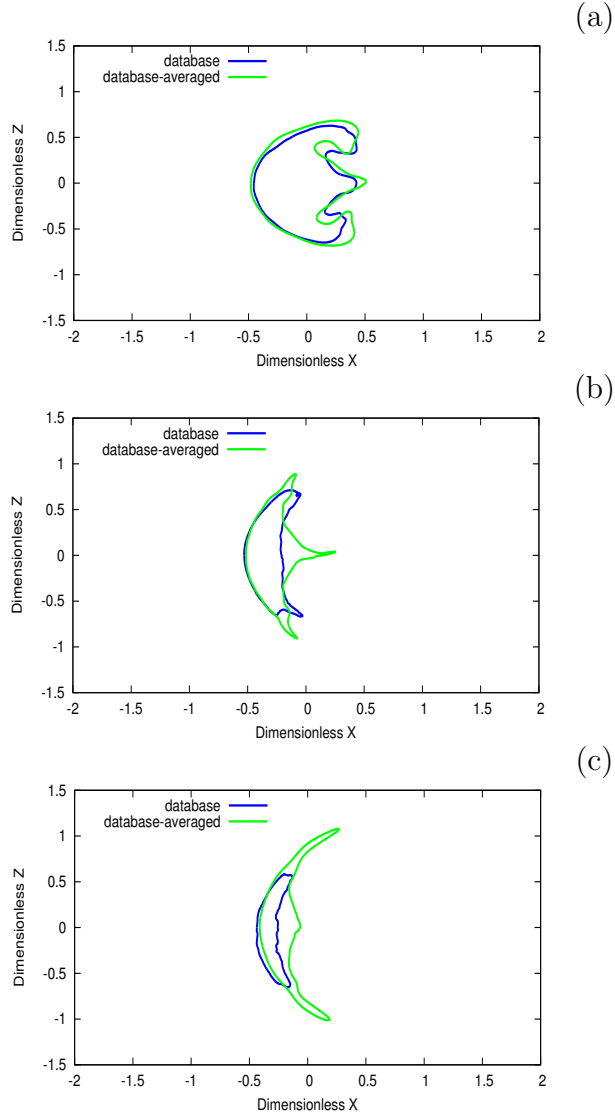


Figure 6.8: Averaged normal cross sections of the jet for different distances from the bottom wall: $y/D=0.5$ (a), $y/D=1.0$ (b), $y/D=1.5$ (c).

simulation using the turbulent pipe flow database, the liquid jet penetrates more in the crossflow gas close to the nozzle exit since the jet inflow boundary condition does not include the effect of the cross flow gas. This can also be explained with respect to local momentum flux ratio. By looking at figure 6.10 it can be seen that the local q in the upwind direction is low for turbulent database including nozzle geometry. Instabilities that are generated on the interface and grow along the jet penetration

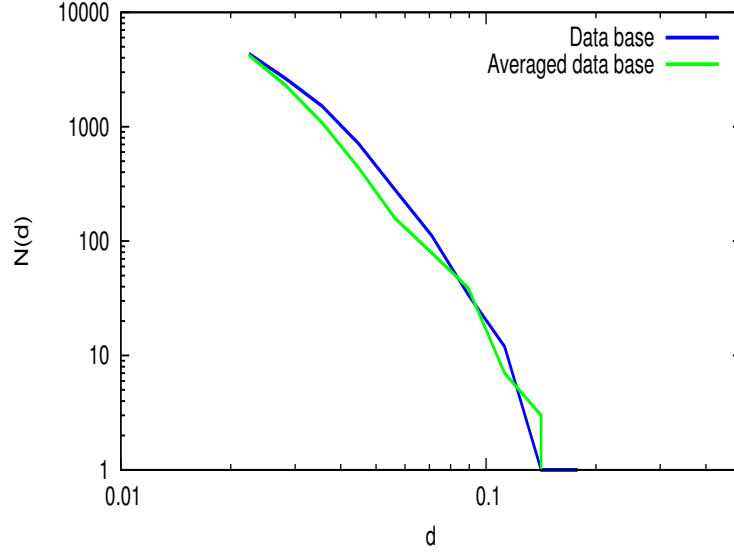


Figure 6.9: Pfd of drop diameters d generated directly by primary atomization.

are comparable for both cases since both include turbulence in the inflow jet at the same Reynolds number.

Figure 6.13 shows different averaged normal cross sections of the jet for different distances from the bottom wall for these two simulations. The liquid columns in both simulations show similar behavior. One noticeable difference is that the center of the cross section area is shifted towards the upwind direction in the simulation using the pipe flow database. This is due to the exclusion of the crossflow effects on the inflow jet. Figure 6.14 shows the drop size distribution. The case using the pipe database has slightly larger drops due to larger instabilities growing on the interface.

Finally we compare the results from the simulation using the time resolved unsteady database with simulation using the rotated database. Figures 6.15 and 6.16 show snapshots of the atomizing jet using these two boundary conditions. Since the liquid jet is pushed more into the gas in the simulation using the rotated database, it penetrates more in the cross flow gas and it experiences more acceleration from

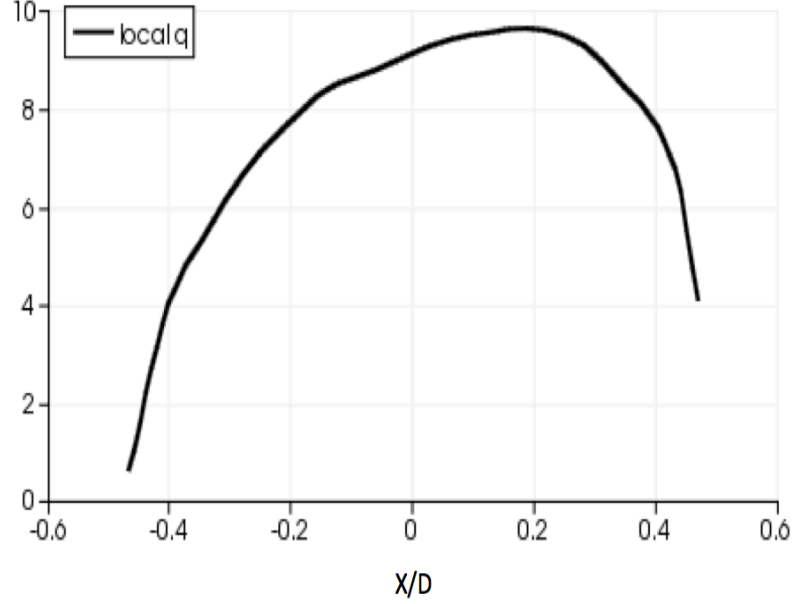


Figure 6.10: Averaged local momentum flux ratio for simulations using turbulent database including nozzle geometry.

the gas, which generates more instabilities on the interface with higher growth rates compared to the simulation using the turbulent database.

Another important parameter in the atomization of the liquid jet in crossflow is the jet penetration correlation. The mean leading edge can be used to determine jet penetration. In order to calculate the mean leading edge, Volume of Fluid scalar (VOF) calculated in eq. 4.5 is averaged over time and different probability isolines are fitted to it (figure 6.18). In our simulations a probability isoline of $VOF=0.5$ is used to calculate the mean leading edge of the jet. Figure 6.17 shows the jet penetration for all four boundary conditions mentioned above. As mentioned before, experimental correlations suggest the dependency of the jet penetration on the momentum flux ratio. So the difference between the jet penetration, specially between the simulations using turbulent database and rotated turbulent database might initially look inconsistent with experimental correlations. But if one predict the jet

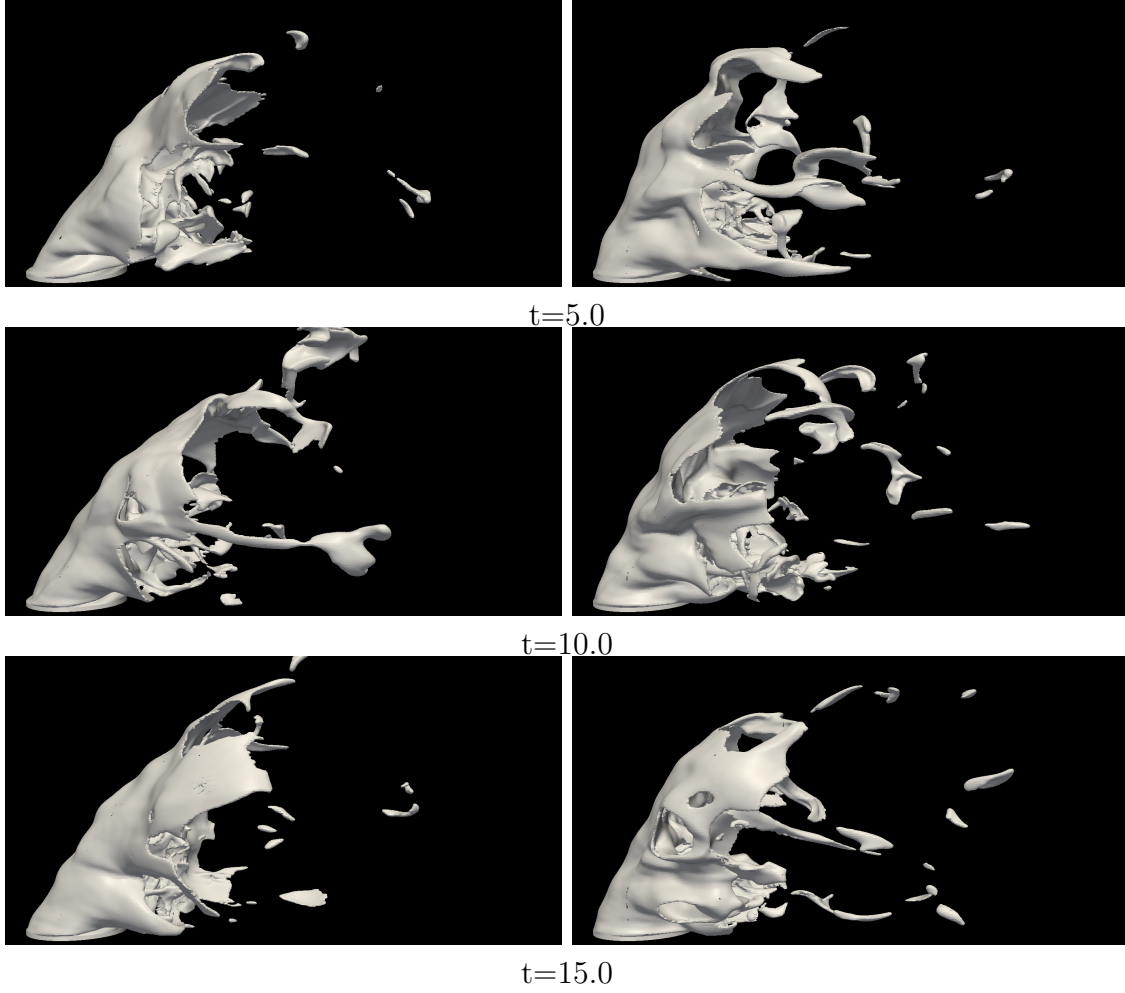


Figure 6.11: Side view snapshots of jet in crossflow atomization with density ratio $r=100$ at $t=5, 10, 15$ time units (top to bottom), using data base (left) and pipe flow (right).

penetrations based on the local momentum flux ratios showed in figure 6.17, the resulted jet penetrations are predictable, since rotated database generates higher local momentum flux ratios at the exit of the nozzle in the upwind direction.

The comparison between the experimental jet penetration correlation of Wu et al [35] and jet penetration from our simulations (figure 6.19) shows that in our simulations, the liquid jet bends faster than in the experimental studies as a result of lower local momentum flux ratio compared to the nominal momentum flux ratio. One other potential reason can be the difference between the density ratios, since

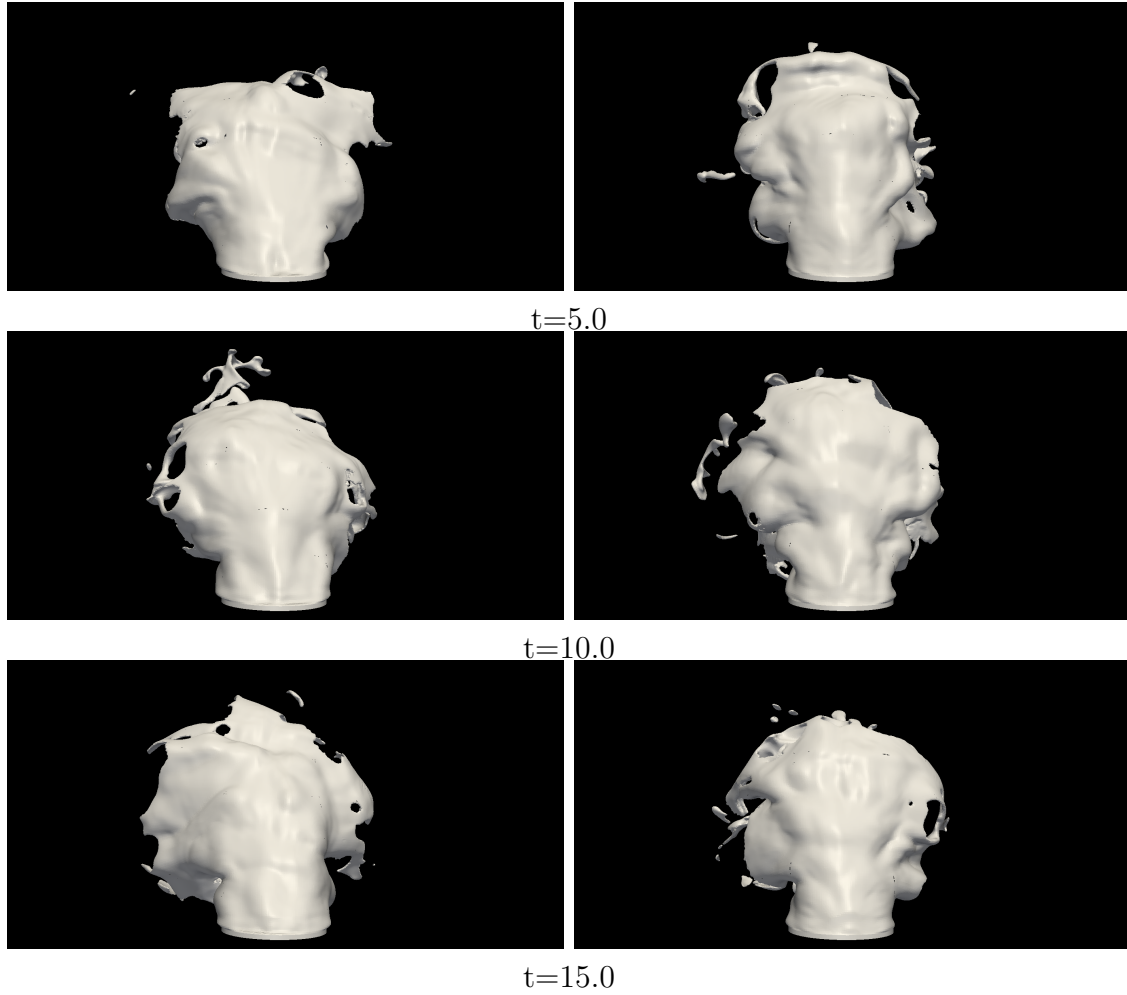


Figure 6.12: Front view snapshots of jet in crossflow atomization with density ratio $r=100$ at $t=5, 10, 15$ time units (top to bottom), using data base (left) and pipe flow (right).

experimental correlations are usually generated from experimental studies at ambient pressure, thus high density ratios due to the cost of experiments.

In order to investigate the effect of density ratio on the jet penetration, another simulation was performed with the same density ratio of the experiment ($r=816$). Comparison between the experimental jet penetration and jet penetration from the simulation with high density ratio (figure 6.20) suggests that density ratio has an important impact on the jet penetration and results from simulations with high density ratio are significantly closer to the experiment.

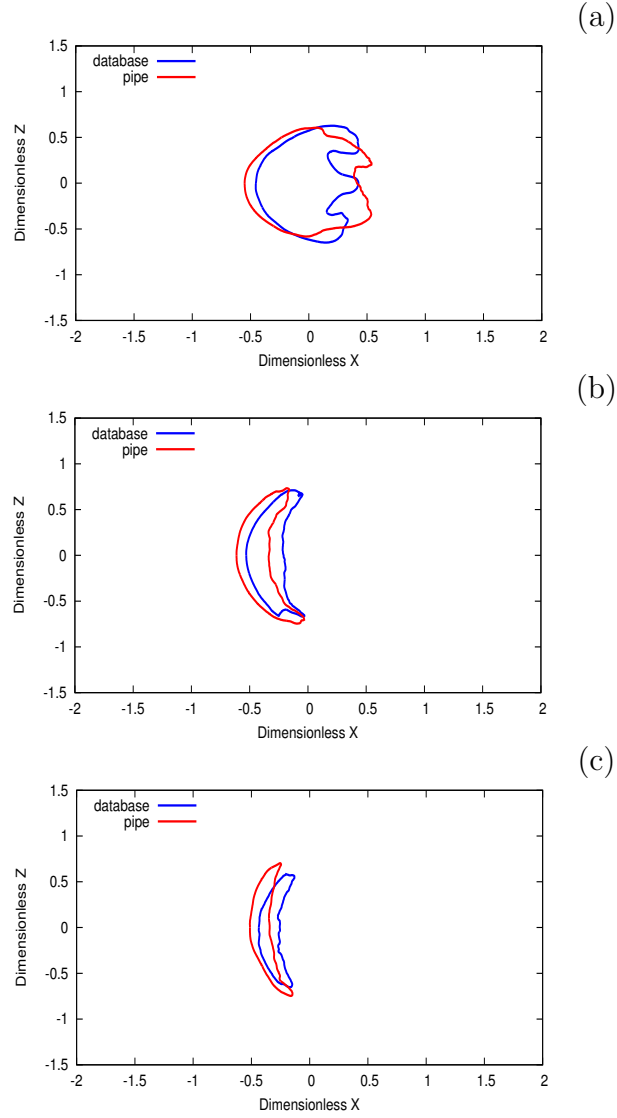


Figure 6.13: Averaged normal cross sections of the jet for different distances from the bottom wall: $y/D=0.5$ (a), $y/D=1.0$ (b), $y/D=1.5$ (c).

Conclusions

Detailed numerical simulations of liquid jets injected into turbulent gaseous cross flows for different liquid jet inflow velocity profiles were performed using the new Consistent Rescaled Momentum Transport method. Four different jet inflow velocity profiles were applied to investigate the impact of turbulence in the inflow jet and the

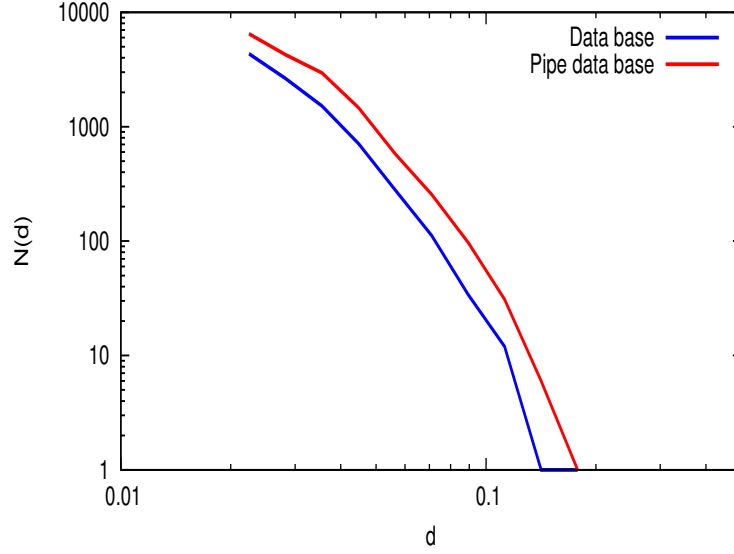


Figure 6.14: Pdf of drop diameters d generated directly by primary atomization.

effect of the cross flow on the incoming jet velocity profile, jet atomization and jet penetration. Results suggest that at the grid resolution that the simulations were performed, turbulence in the inflow jet velocity profile has a slight impact on the instabilities that grow on the surface of the liquid column and lead to the breakup of the jet. Results also show that impact of the cross flow gaseous on the velocity profile of the inflow jet effects the results of the simulation including the penetration of the liquid jet in the cross flow gas and the instabilities generated on the interface. Comparison between the jet penetration for simulations with different density ratios indicates changing the density ratio changes the jet penetration and using the same density ratio as the experiment makes the results of the simulation more comparable to the experimental penetration correlations.

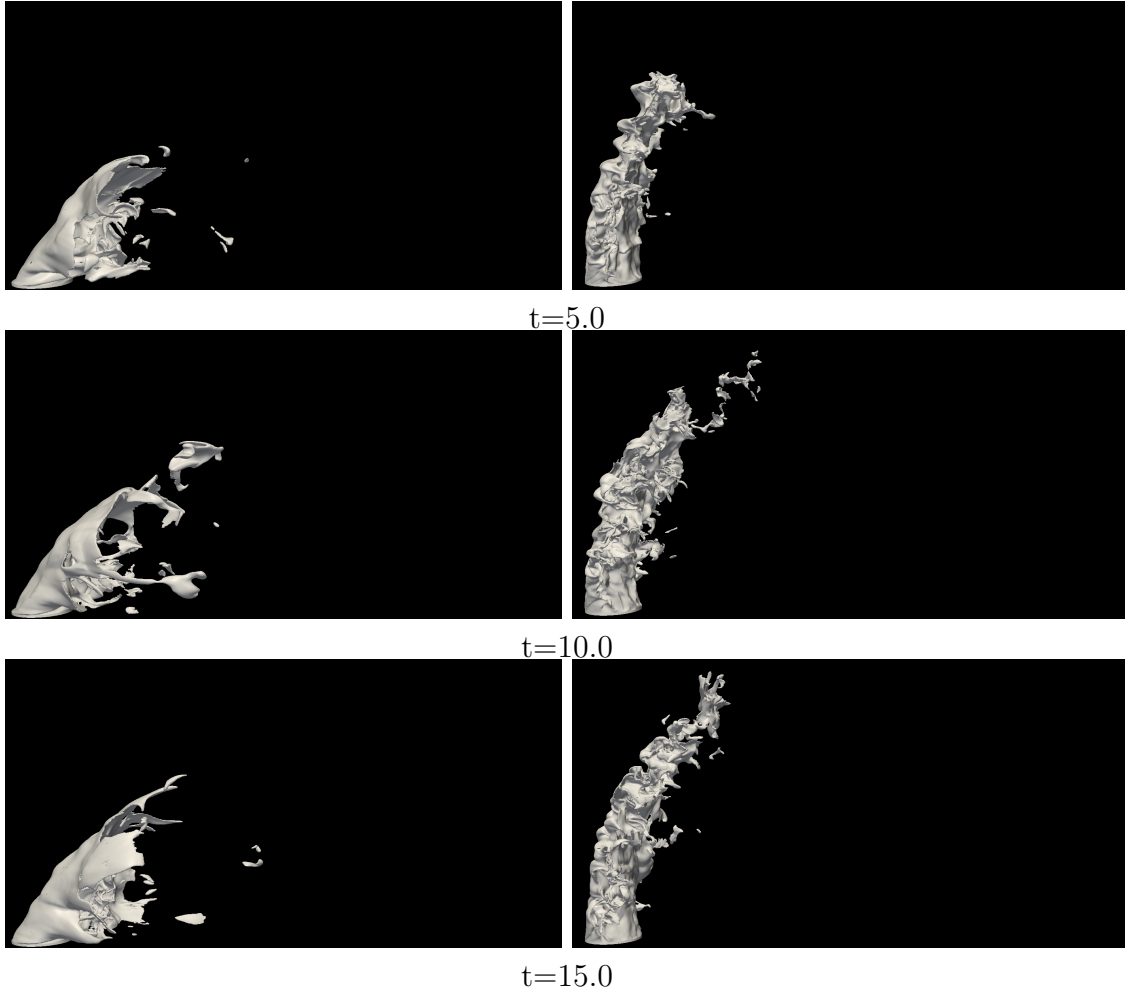


Figure 6.15: Side view snapshots of jet in crossflow atomization with density ratio $r=100$ at $t=5, 10, 15$ time units (top to bottom), using database (left) and rotated database (right).

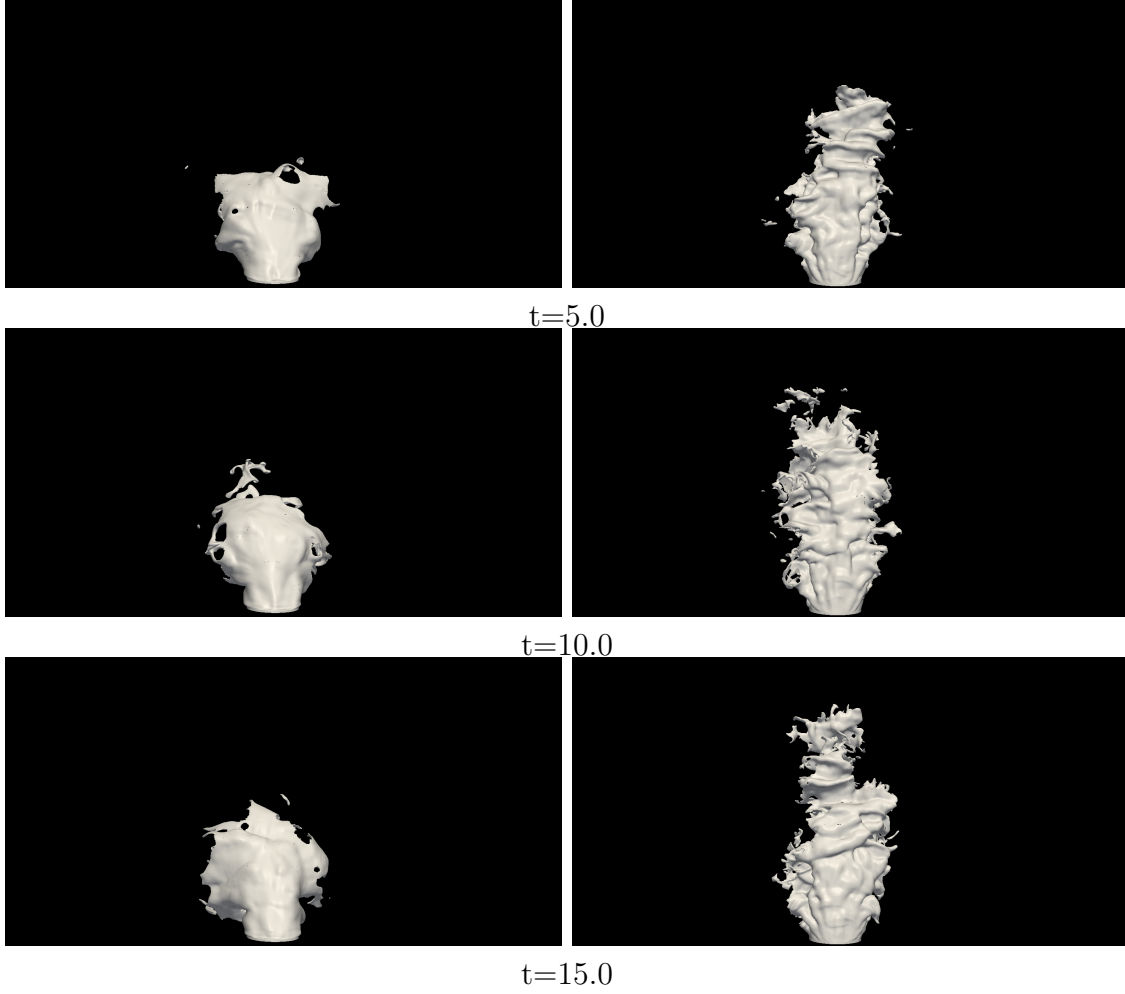


Figure 6.16: Front view snapshots of jet in crossflow atomization with density ratio $r=100$ at $t=5, 10, 15$ time units (top to bottom), using database (left) and rotated database (right).

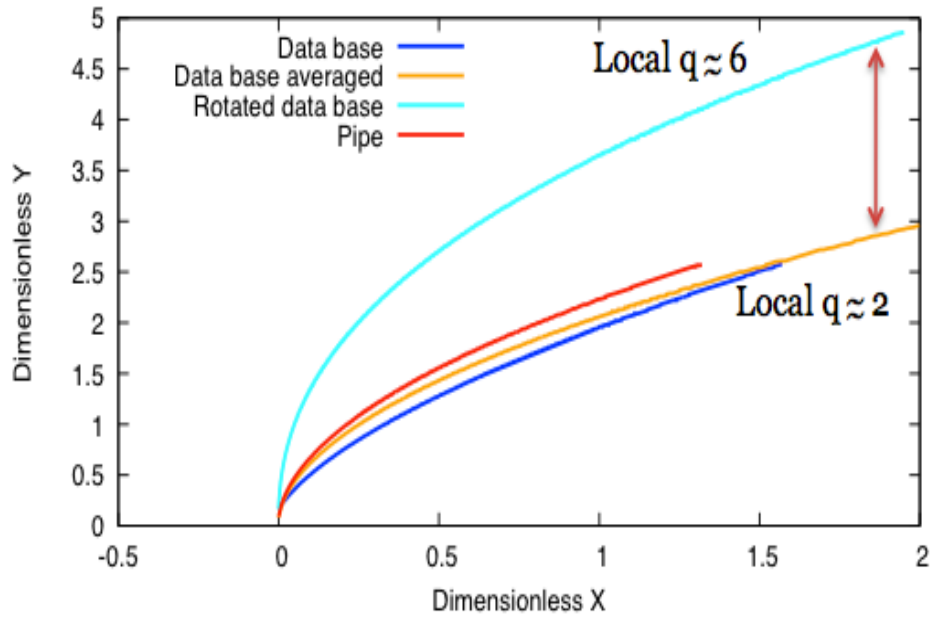


Figure 6.17: Jet penetration from the simulations using different local momentum flux ratios(q) based on a experimental study with $q=6.6$

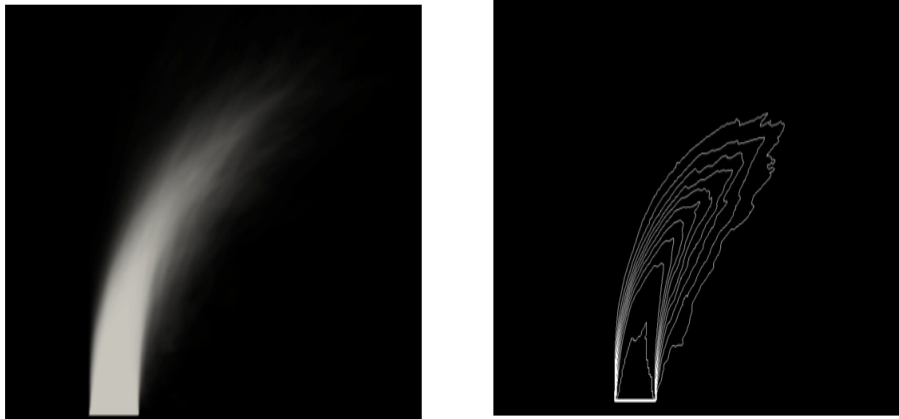


Figure 6.18: Averaged Volume of Fluid (left) and probability isoline (right).

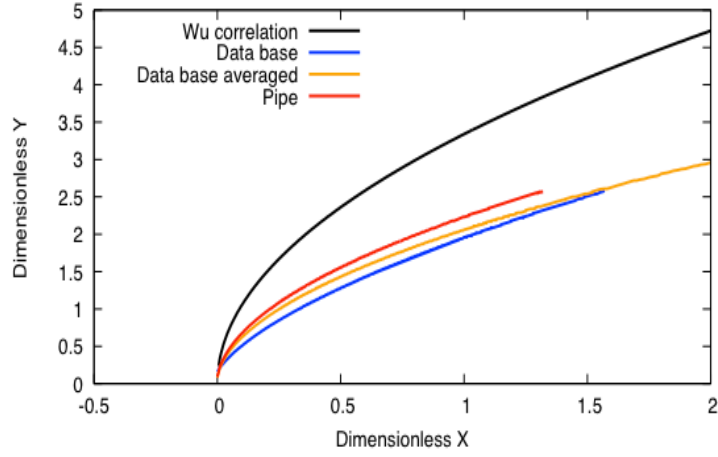


Figure 6.19: Comparison between jet penetration from numerical simulations with density ratio $r=100$ and experimental correlations.

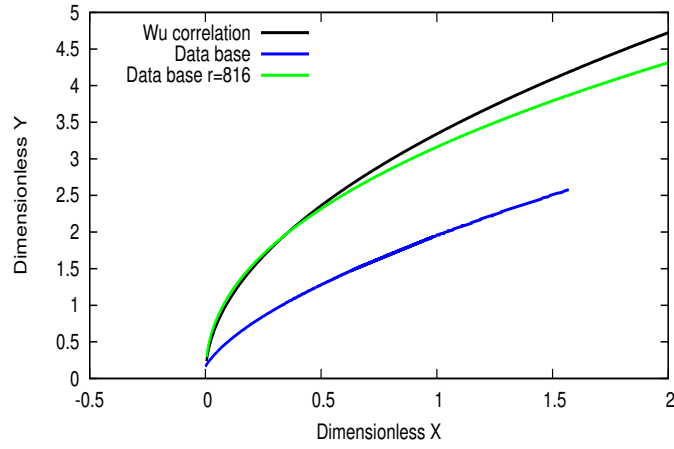


Figure 6.20: Comparison between jet penetration from numerical simulations with high density ratio and experimental correlations.

Chapter 7

Instability Analysis

As mentioned in the introduction section, instability mechanisms that generate growing waves on the interface of the jet injected into the crossflow gas have been studied experimentally for many years. As we know, most of the experimental studies are performed at ambient condition, meaning gas with low pressure and thus high density ratios between the injected liquid and the crossflow gas. Performing numerical simulations of jet in crossflow atomization for different density ratios and performing instability analysis on them in order to find the most dominant mode will help us to make predictions for other configurations without needing to perform full simulations. Finding the most dominant breakup mode and corresponding wavelength that enables us to have a good prediction for the size of the generated droplets.

In this section numerical simulations of jet in crossflow atomization are performed with lower density ratios in order to investigate the possibility of different instability mechanisms at different operating conditions. It is also explained how results from the detailed numerical simulation of the jet in crossflow atomization will be used, in order to find out the dominant instability mechanism involved in the breakup of jet in crossflow.

Instability analysis usually is performed for different characteristic numbers such as We and momentum flux ratio q , but due to difficulties in performing experiments with high gas pressures, the effect of changing density ratio on liquid jet breakup is not studied in details. So, in this chapter instability analysis is performed for different density ratios and effects of changing density ratio on breakup process of the liquid column is investigated.

7.1 Instability Modes

Exploring the conditions where different breakup mechanisms are present suggests that there are multiple potential instability mechanisms in atomization of jet in cross-flow. Here two of these instability mechanisms that most likely have more impact on the breakup of liquid jet are discussed. These instability modes are Kelvin-Helmholtz instability also called shear driven instability and Rayleigh-Taylor instability also called acceleration instability. Kelvin-Helmholtz (classical shear driven instability) can occur when there is a velocity difference across the interface between two fluids, as it is shown in figure 7.1. It is very common in this type of instability to witness the development of interfacial waves or even, for more rapid flows, the mixing of the two fluids as the surface eventually breaks into drops.

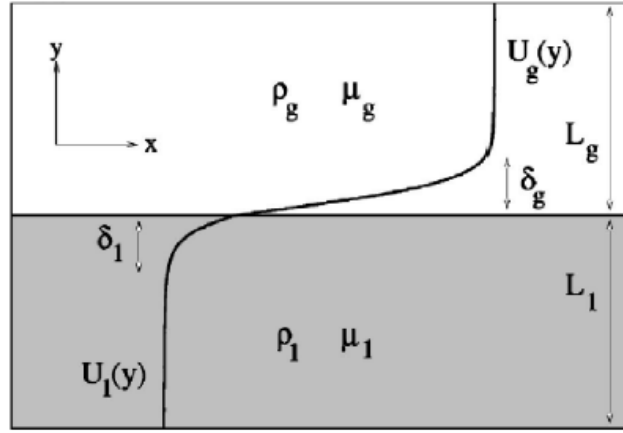


Figure 7.1: A schematic representation of the shear flow for Kelvin-Helmholtz instability study.

On the other hand, Rayleigh-Taylor instability occurs when acceleration is acting on two fluids of different density, for example the dense fluid above a fluid of

lesser density under gravity force. The equivalent situation occurs when the lighter fluid is pushing the heavier fluid. This happens in the jet in crossflow atomization where liquid with low velocity in the crossflow direction is injected into the high speed crossflow gaseous.

7.2 Proper Orthogonal Decomposition

Proper Orthogonal Decomposition (POD) can be used to perform statistical analysis of flow snapshots. POD is today an established technique and many investigators have successfully used POD to analyze complex flow fields. Meyer et al. [36] used PIV based POD to analyze flow structures in jet in crossflow configurations. Moin and Moser [37] used DNS based POD analysis to study fully developed channel flows.

To analyze the instability mechanism of the liquid column, POD of side view images extracted from detailed simulations of the near injector primary atomization region were performed for two density ratios, $r = 10$ and $r = 100$ [3]. Side view images are used instead of data for the full geometry to follow exactly the same process used in the experimental studies. Table 7.1 summarizes the parameters used in those two simulations.

This analysis shows a single dominant wavelength with the associated interface corrugation traveling downstream with the jet for each case, shown in figure 7.2. The non-dimensional wavelength is $\lambda/D = 1.7$ for density ratio 10 and $\lambda/D = 1.1$ for density ratio 100.

7.3 Linear Analysis

In this section it is explained how results from the numerical simulations of jet in crossflow atomization is used as the input for the linear instability theories for both Rayleigh-Taylor and Kelvin-Helmholtz mechanisms. This shows the importance of numerical simulations since those flow conditions including the velocities across the

density ratio $r = \rho_j / \rho_c$	10	100
crossflow density ρ_c [kg/m^3]	1.225	1.225
jet density ρ_j [kg/m^3]	12.25	122.5
crossflow velocity u_c [m/s]	120.4	120.4
jet velocity u_j [m/s]	97.84	30.94
crossflow viscosity μ_c [kg/ms]	1.82e-5	1.82e-5
jet viscosity μ_j [kg/ms]	11.1e-4	3.5e-4
surface tension coeff. σ [N/m]	0.07	0.07
momentum flux ration q	6.6	6.6
crossflow Weber number We_c	330	330
jet Weber number We_j	2178	2178
crossflow Reynolds number Re_c	5.7e5	5.7e5
jet Reynolds number Re_j	14079	14079

Table 7.1: Operating conditions and characteristic numbers for the numerical simulations with $r = 10$ and $r = 100$ [3].

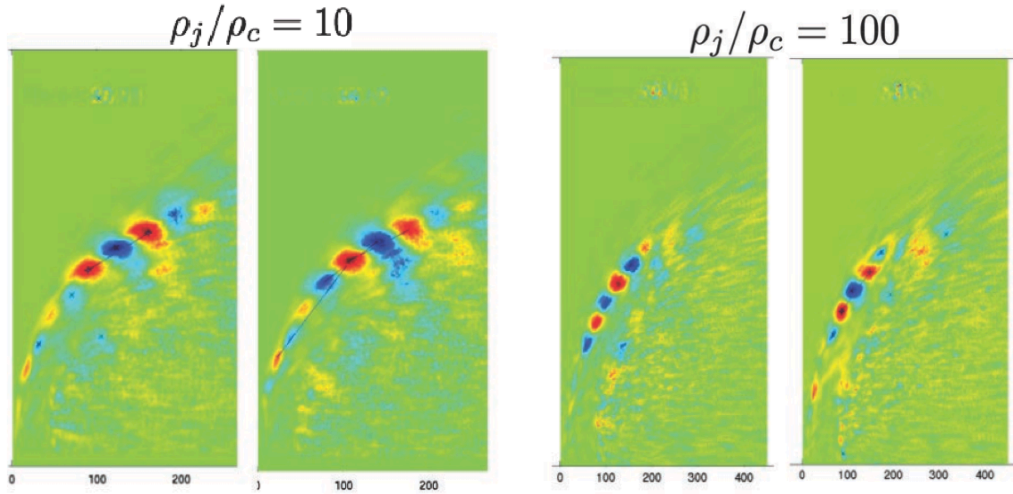


Figure 7.2: Proper orthogonal decomposition for $r=10$ (left) and $r=100$ (right) [3].

interface can not be measured experimentally. Results are compared to the POD analysis to determine which instability mode is responsible for the breakup of the liquid column and also to determine whether density ratio has an impact on the dominant instability mechanism or not. Results can also show the validation of the spray models from experimental studies.

Kelvin- Helmholtz:

Introducing perturbations in the manner of traditional linear perturbation theory leads to the familiar Orr-Sommerfeld equation for the lower layer fluid, indicated with subscript 1 here, and the same for the upper layer fluid, indicated with subscript 2, but for the additional appearance of r/m , where $r = \frac{\rho_2}{\rho_1}$, and $m = \frac{\mu_2}{\mu_1}$. Nondimensionalization is based on lower layer quantities. The perturbation equations read:

$$(U_1 - c)(D_I^2 - \alpha^2)\phi_1 - U_1''\phi_1 = \frac{1}{i\alpha Re}(D_I^2 - \alpha^2)^2\phi_1 \quad (7.1)$$

$$(U_2 - c)(D_I^2 - \alpha^2)\phi_2 - U_2''\phi_2 = \frac{m}{r} \frac{1}{i\alpha Re}(D_I^2 - \alpha^2)^2\phi_2 \quad (7.2)$$

Here D_I is the operator for differentiation across the interface, ϕ represents the eigenfunction of the streamfunction in the cross interface direction, and complex quantity c represents the eigenvalue for the real wavenumber α . Boundary conditions include the continuities, both for normal and tangential components of the velocity and the stress. The results of analysis show three different modes: Interfacial mode, Liquid Tollmien-Schlichting mode, Gas Tollmien-Schlichting mode, it also shows that surface tension stabilizes this kind of instability, for more detail see [38] and references there. The results also suggest the sensitivity of the instability to the following quantities: $n = \frac{\delta_1}{\delta_2}$, $m = \frac{\mu_2}{\mu_1}$, r , u_2 and u_1 . Where δ_1 , and δ_2 are the boundary layer thicknesses shown in figure 7.1. The procedure by Yecko et al., [38] gives the growth-rate as function of wavelength for different shear instability modes that may arise at the phase interface.

Steps to calculate the required boundary layer velocity profiles at the phase interface from the simulation data are as follow, shown also in figure 7.3: First the

center of mass(center line) is calculated for each instantaneous time of the simulation using VOF scalar field, and that center line is divided into equidistance points with distance $D/4$. Then the closest point on the windward of the interface to each of these center line points is found using the iso-surface of the scalar VOF=0.5.

Next, normal lines to the interface from these closest interfacial nodes, found in the previous step, are considered and divided into equidistance nodes. Finally the normal velocity to these normal lines(which are good representatives of the tangential velocities across the interface), for each of the nodes on them is calculated, using the velocity field resulted from the simulation. Averaging the velocities over time, starting from the time that the simulation has reached a steady state, results in the velocity profile conditioned on the centerline arc-length and normal coordinate that can be used in the calculation of shear instability modes. Figure 7.4 and 7.5 show these velocity profiles for jet in crossflow simulations with density ratio 10 and 100.

It should be mentioned again that keeping the momentum flux ratio the same, gives the gas a lower velocity for density ratio 10 compared to 100. As it can be seen in figure 7.4 and 7.5 for density ratio 10, the liquid jet always has higher relative velocity, moving along the jet penetration. For density ratio 100 liquid initially has higher tangential velocity to the interface, but as it bends along the jet penetration, tangential velocities to the interface in the gas become larger.

Rayleigh-Taylor:

An analytical analysis of [39] gives the growth-rate of Rayleigh-Taylor instability valid in the linear regiem as following:

$$\eta^2 + 2\eta k^2 \left(\frac{\mu_l - \mu_g}{\rho_l + \rho_g} \right) + \frac{k^3 \sigma}{\rho_l + \rho_g} - ka \left(\frac{\rho_l - \rho_g}{\rho_l + \rho_g} \right) = 0 \quad (7.3)$$

where a is the acceleration acting on the interface, η is the growth-rate and k is the wave number. The mean acceleration normal to the interface, used in equation

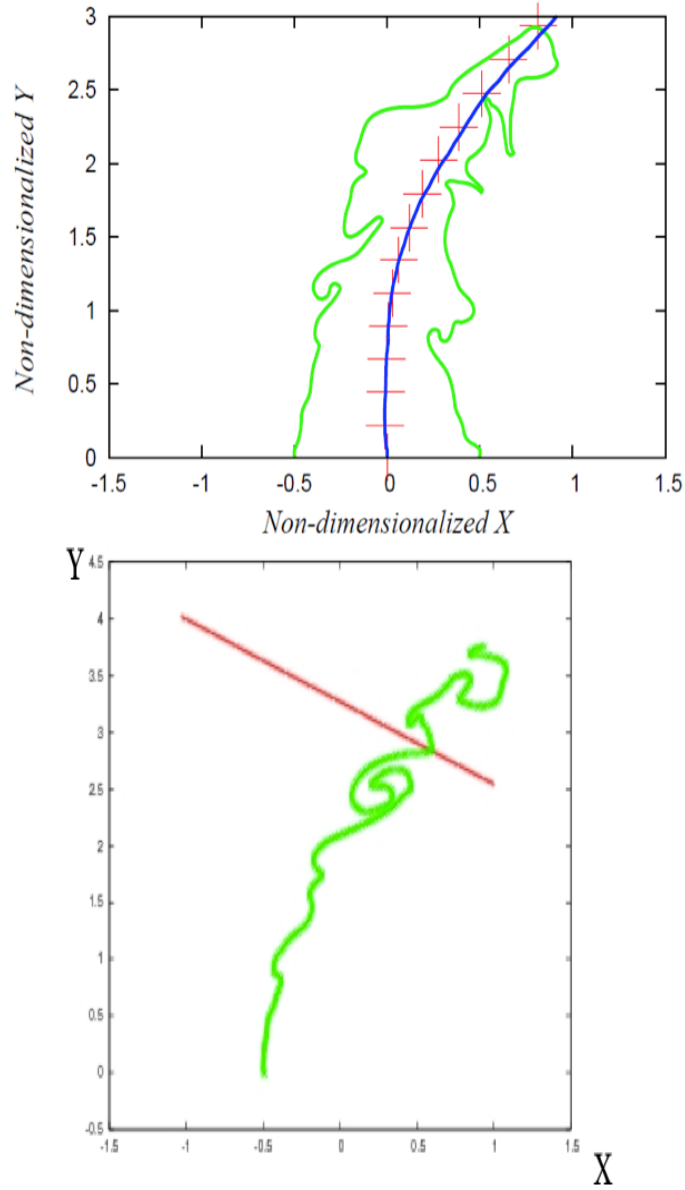


Figure 7.3: Center line(left) and normal line to the interface from the closest nodes on the surface(right).

7.3 is calculated using the averaged leading edge based on VOF-0.5, shown in figure 7.6, assuming that a particle is traveling along the leading edge with the tangential velocity calculated in the previous section. Figure 7.7 shows the resulting accelerations for jet in crossflow simulations with density ratios 10 and 100.

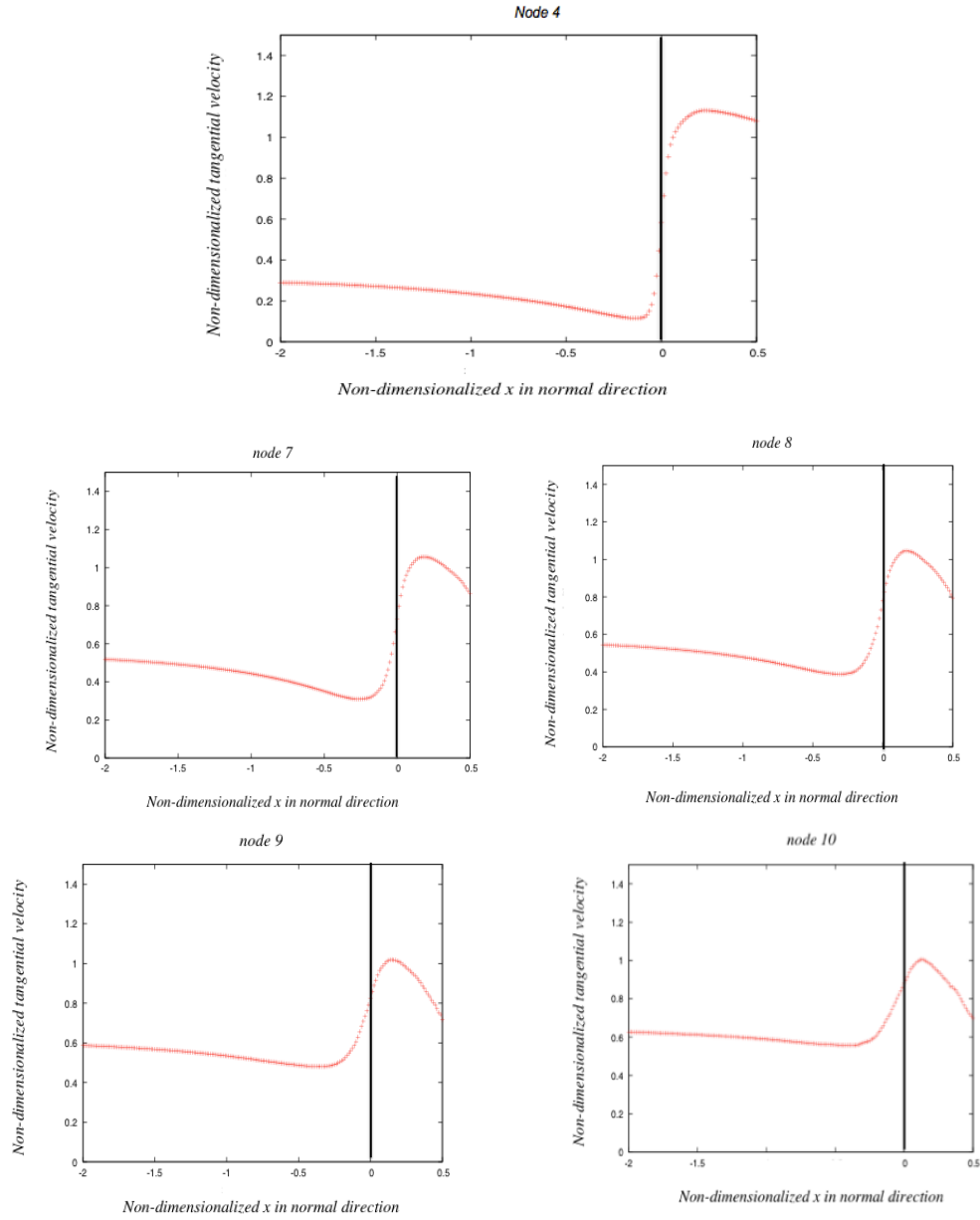


Figure 7.4: Tangential velocity profile on the normal line to the interface for the interfacial nodes with associated nondimensional arc-length $s/D = 1.0$ (node4), $s/D = 1.75$ (node7), $s/D = 2$ (node8), $s/D = 2.25$ (node9), $s/D = 2.5$ (node10) for density ratio 10.

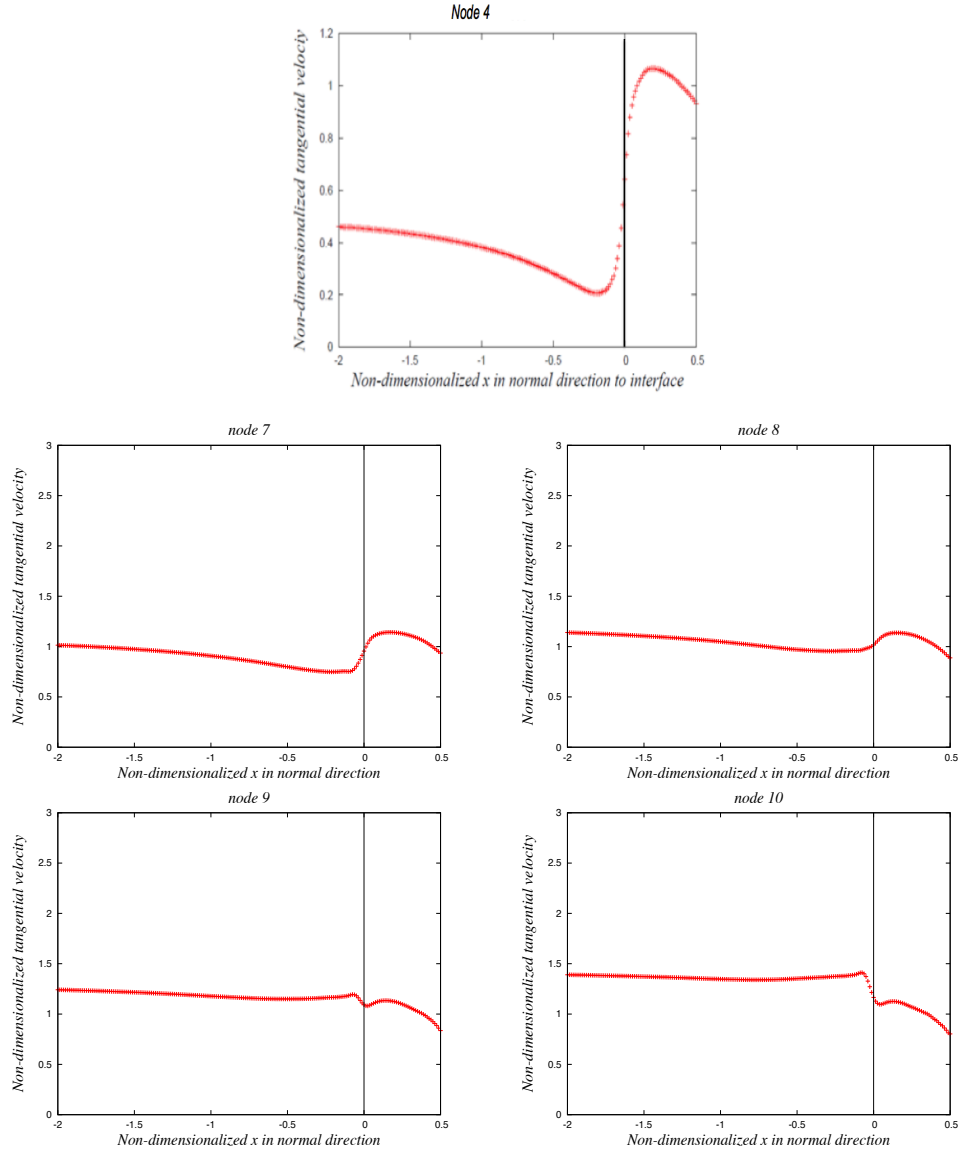


Figure 7.5: Tangential velocity profile on the normal line to the interface for the interfacial nodes with associated nondimensional arc-length $s/D = 1.0$ (node4), $s/D = 1.75$ (node7), $s/D = 2$ (node8), $s/D = 2.25$ (node9), $s/D = 2.5$ (node10) for density ratio 100.

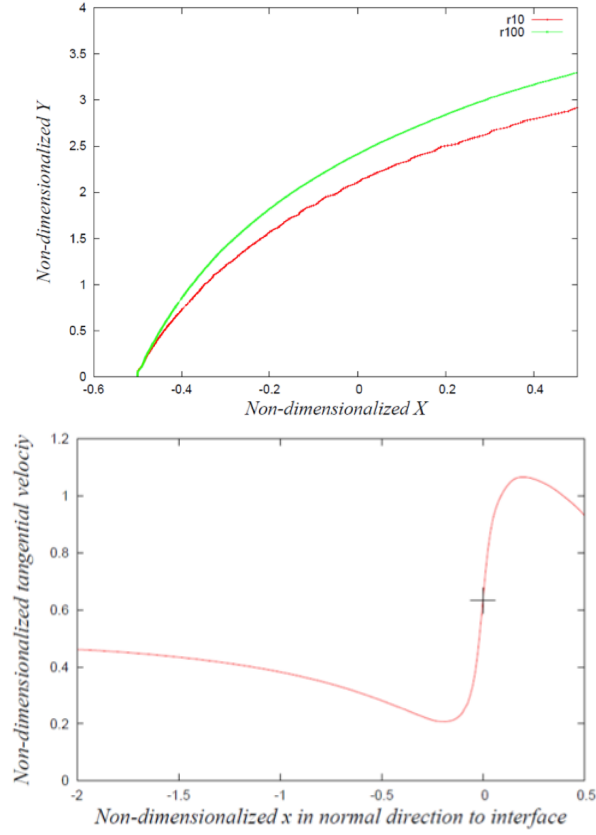


Figure 7.6: Mean acceleration is calculated using the averaged leading edge based on VOF-0.5(top) and the velocity of the interfacial nodes(bottom).

Results:

Figures 7.8 and 7.9 show that both instability mechanisms yield the correct order of magnitude for the wavelength of the dominant corrugation, with the acceleration driven instability explaining the data best. However, the results also shows that POD wavelengths are larger than the Rayleigh-Taylor driven instability wavelenths for both density ratios. This can be due to the stretching effects of the crossflow gas on the liquid jet, since the traveling waves identified in POD analysis are not exactly at the nozzle exit. It should also be mentioned that at $r=10$ Kelvin- Helmholtz instability should be more pronounced than at $r=100$, because the aerodynamic effect is in theory larger. However, since momentum flux ratio is kept constant, this is mitigated.

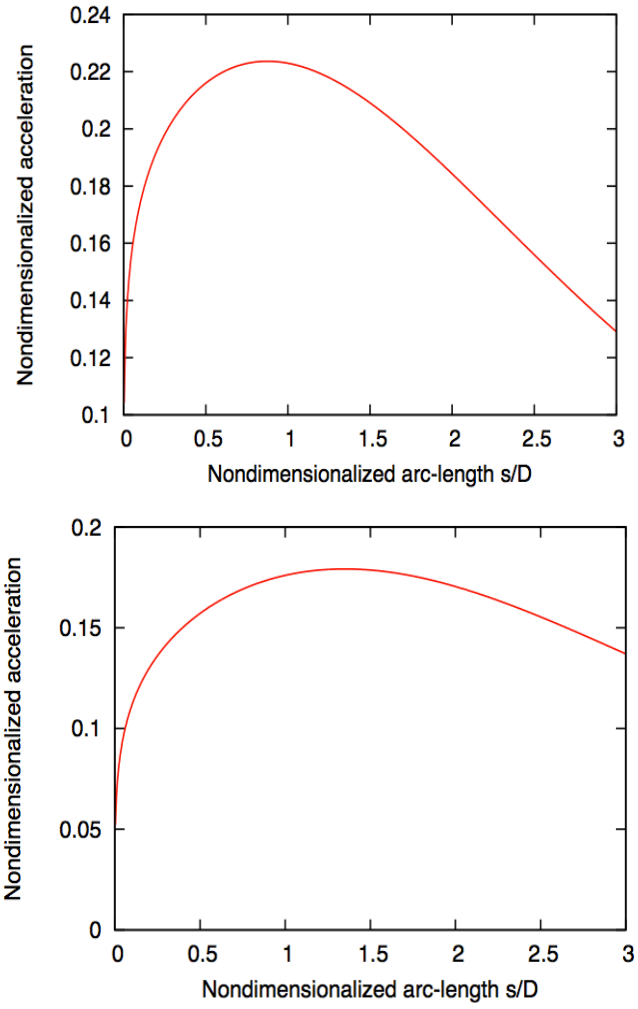


Figure 7.7: Nondimensionalized mean acceleration on averaged leading edge based on VOF-0.5 for jet in crossflow with density ratio 10(top) and 100(bottom).

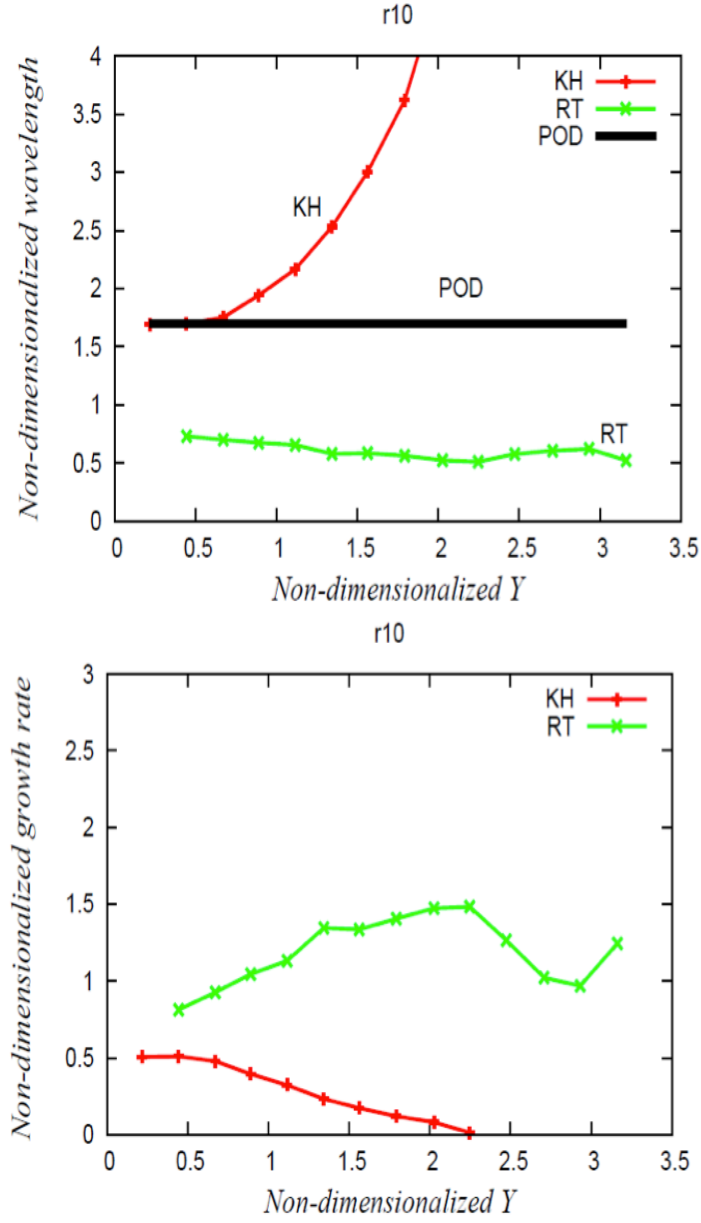


Figure 7.8: The wavelength and growth-rate of Kelvin- Helmholtz and Rayleigh-Taylor instabilities for jet in crossflow simulation with density ratio 10.

7.4 Nonlinear Analysis

Above results are calculated based on linear instability theories for Rayleigh-Taylor and Kelvin- Helmholtz, which means for disturbances with small amplitudes. But

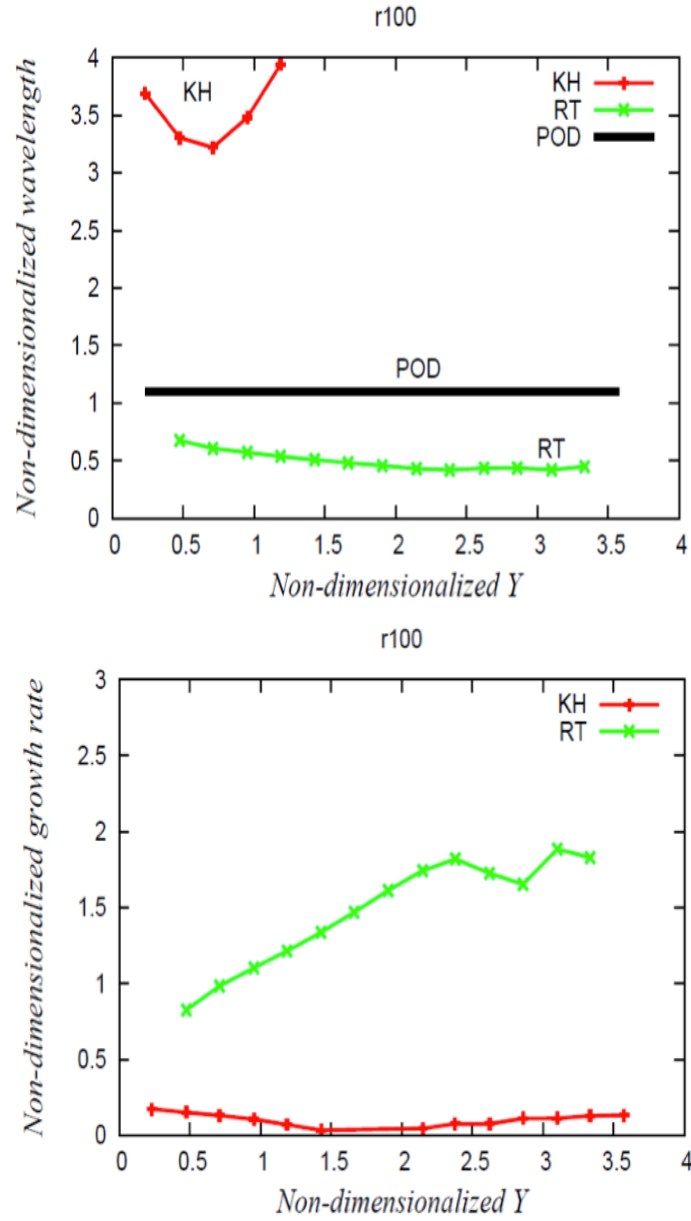


Figure 7.9: The wavelength and growth-rate of Kelvin- Helmholtz and Rayleigh-Taylor instabilities for jet in crossflow simulation with density ratio 100.

waves that cause the column to break must have an amplitude as large as the jet diameter which necessitates a nonlinear analysis.

In order to perform nonlinear analysis we need a nonlinear solver and the actual flow solver is used for that purpose. A mean solution is also needed for the

nonlinear analysis. The averaged database explained in section 5 is used to establish a mean solution. In addition the boundary condition needs to be controlled in order to study nonlinear growth of waves with the most unstable linear wavelength. In other words an instability with most unstable linear wavelength must be imposed and its nonlinear evolution should be studied. For this purpose a wave is imposed to the inflow jet by oscillating the radius of the nozzle exit as a function of time which can be achieved by superposing a sinusoidal function in time to the jet boundary condition in the radial direction:

$$r(t) = r_0 * (1 + a_0 * \sin(2\pi * (\frac{V}{\lambda_{linear}}) * t)) \quad (7.4)$$

where r_0 is unperturbed radius, a_0 the amplitude of the function is set to 0.01 in the simulations. Larger amplitudes may add a large amount of mass on the liquid jet and change the physics of the problem. λ_{linear} is wavelength from linear instability analysis (figures 7.8 and 7.9) and V is the velocity of the interface in the upwind direction at the nozzle exit. First guess for V can be the interface velocity right after the nozzle exit. But due to the developed boundary layer in the nozzle this velocity is theoretically close to zero. So instead of above option, another way is chosen in our simulations to calculate the needed velocity by averaging the mean velocity of the interface on the jet penetration up to the breakup point, calculated in linear analysis of Kelvin- Helmholtz instability.

Calculated frequencies corresponding to Rayleigh-Taylor most unstable wavelengths are 0.55 and 0.65 for $r = 10$ and $r = 100$ and calculated frequencies corresponding to Kelvin- Helmholtz most unstable wavelengths are 3.5 and 1.7 for $r = 10$ and $r = 100$. The evolution of the imposed waves can be a good indicator for the influence of the corresponding mode on the breakup process.

Results:

As can be seen in figures 7.10- 7.13 in the simulations with the density ratio $r = 10$ the waves generated from the oscillating nozzle corresponding to the Rayleigh-Taylor persist, grow, and result in regular periodic breakup of the column while waves generated from the oscillating nozzle corresponding to the Kelvin- Helmholtz instability damp along the downstream direction of the liquid. This comparison suggests that Rayleigh-Taylor instability is the more effective mechanism for the breakup of the liquid column compared to the Kelvin- Helmholtz instability for the analyzed wavelengths.

Figures 7.10- 7.13 show the result for the simulation with density ratio $r = 100$. In these simulations Rayleigh-Taylor has again a higher growth rate compared to Kelvin- Helmholtz which is consistent with the results from linear analysis. It can also be noticed that the Kelvin- Helmholtz instabilities have higher growth rate in the case with $r = 10$ compared to $r = 100$. The reason can be the fact that Kelvin- Helmholtz's most unstable wavelength is almost twice as Rayleigh-Taylor's most unstable wavelength for density ratio $r = 10$ (see figure 7.8) and can include the affects of Rayleigh-Taylor instability on its growth rate.

Overall it can be concluded that like in experimental studies with high density ratios, in lower density ratios also Rayleigh-Taylor mechanism is the most dominant breakup mode.

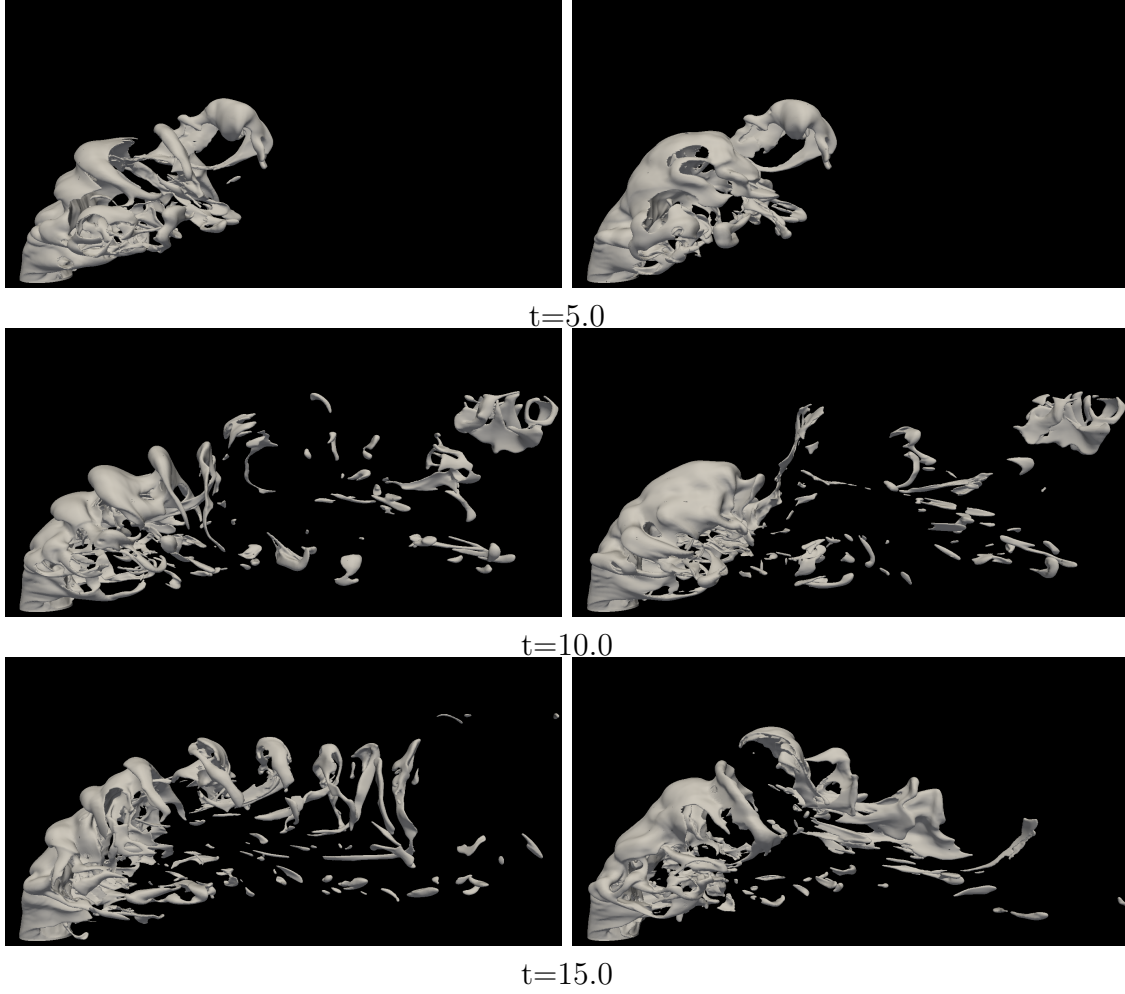


Figure 7.10: Side view snapshots of jet in crossflow atomization with density ratio $r=10$ at $t=5, 10, 15$ time units (top to bottom). Rayleigh-Taylor instability (left), Kelvin-Helmholtz instability (right).

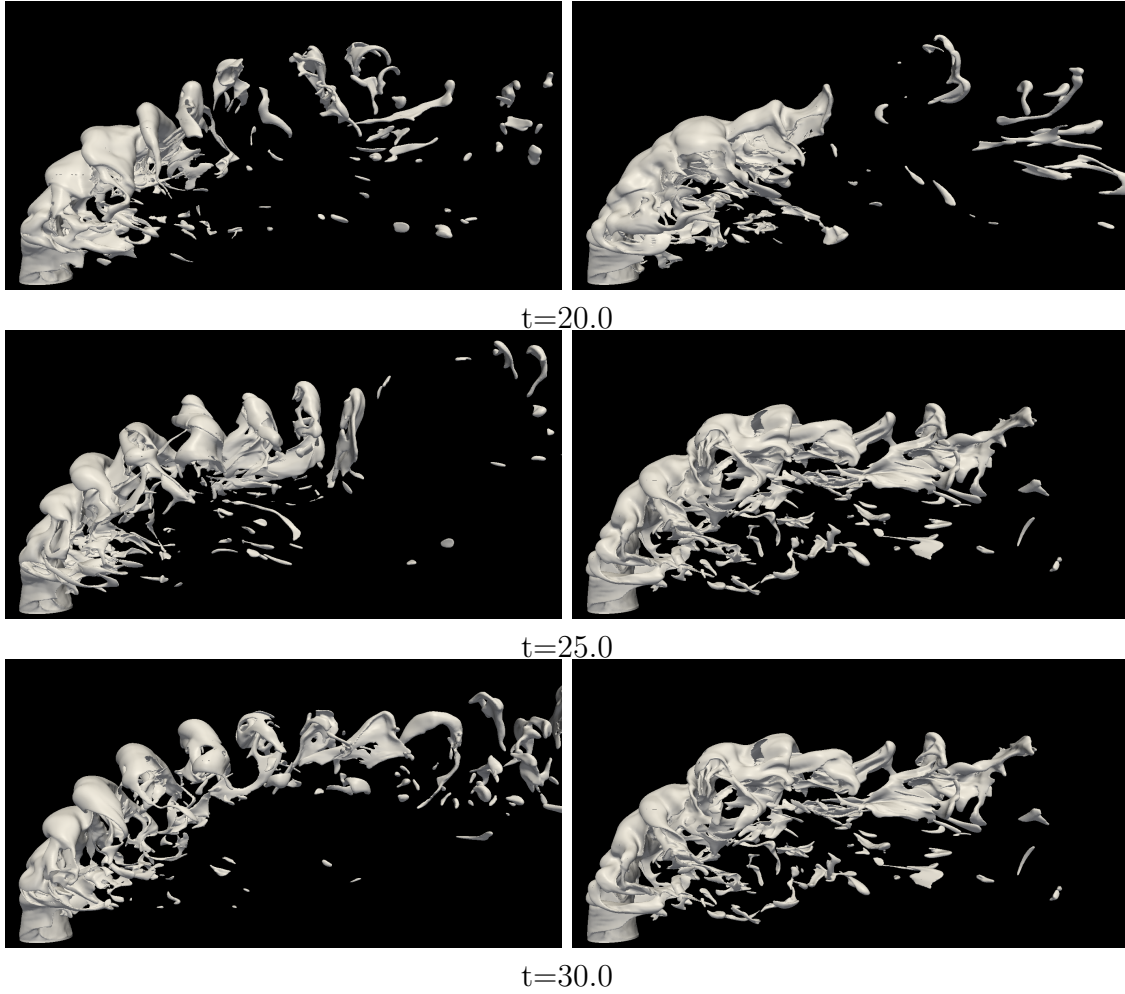


Figure 7.11: Side view snapshots of jet in crossflow atomization with density ratio $r=10$ at $t=20, 25, 30$ time units (top to bottom). Rayleigh-Taylor instability (left), Kelvin-Helmholtz instability (right).

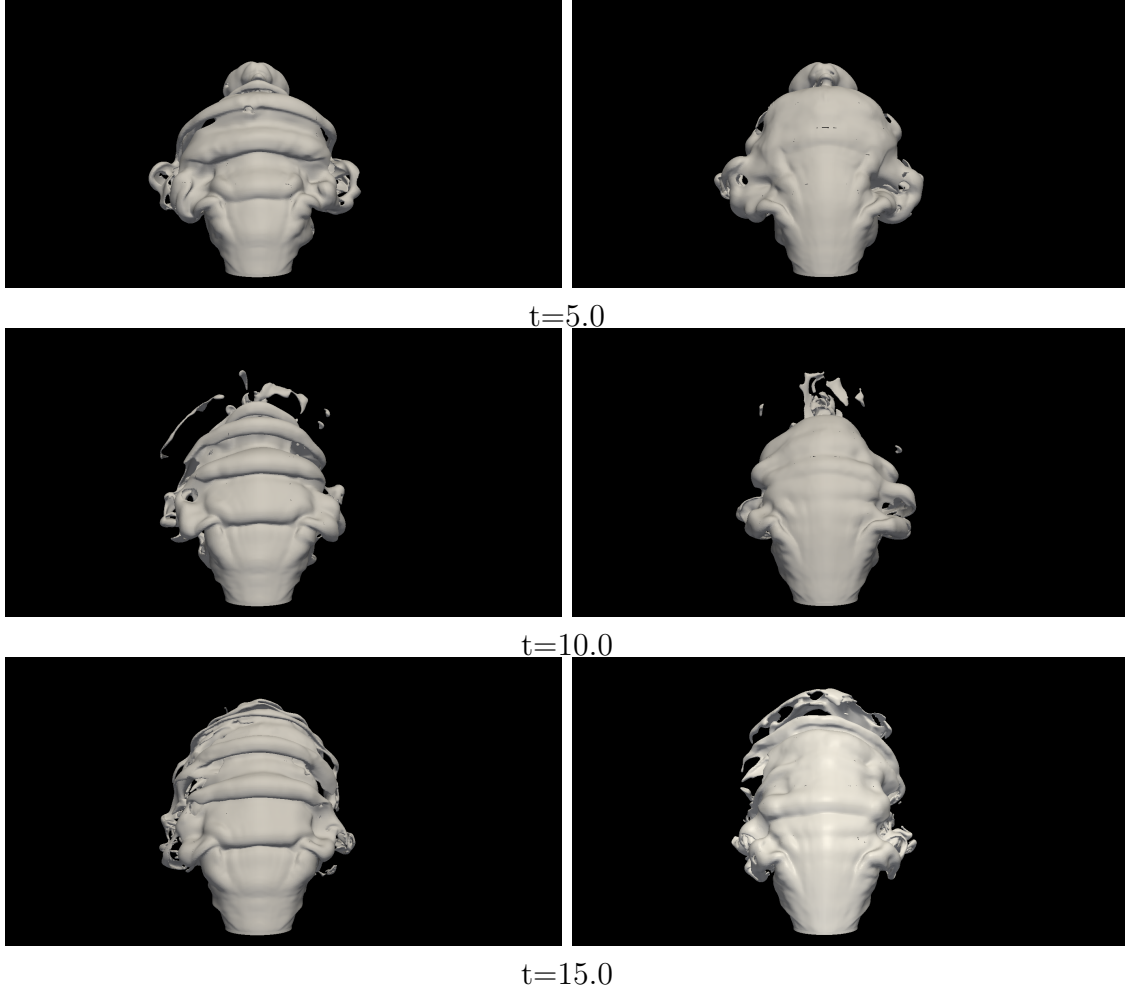


Figure 7.12: Front view snapshots of jet in crossflow atomization with density ratio $r=10$ at $t=5, 10, 15$ time units (top to bottom). Rayleigh-Taylor instability (left), Kelvin-Helmholtz instability (right).

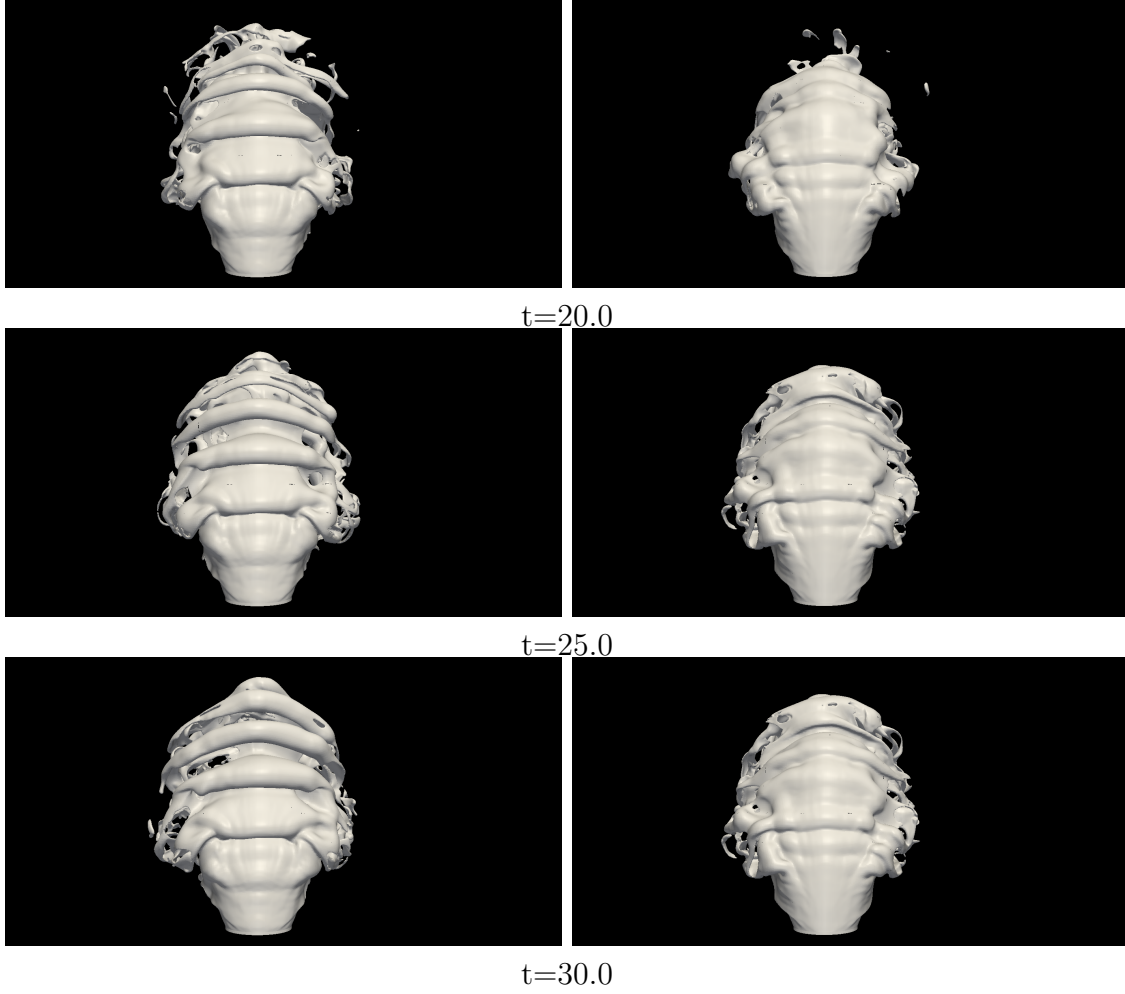


Figure 7.13: Front view snapshots of jet in crossflow atomization with density ratio $r=10$ at $t=20, 25, 30$ time units (top to bottom). Rayleigh-Taylor instability (left), Kelvin-Helmholtz instability (right).

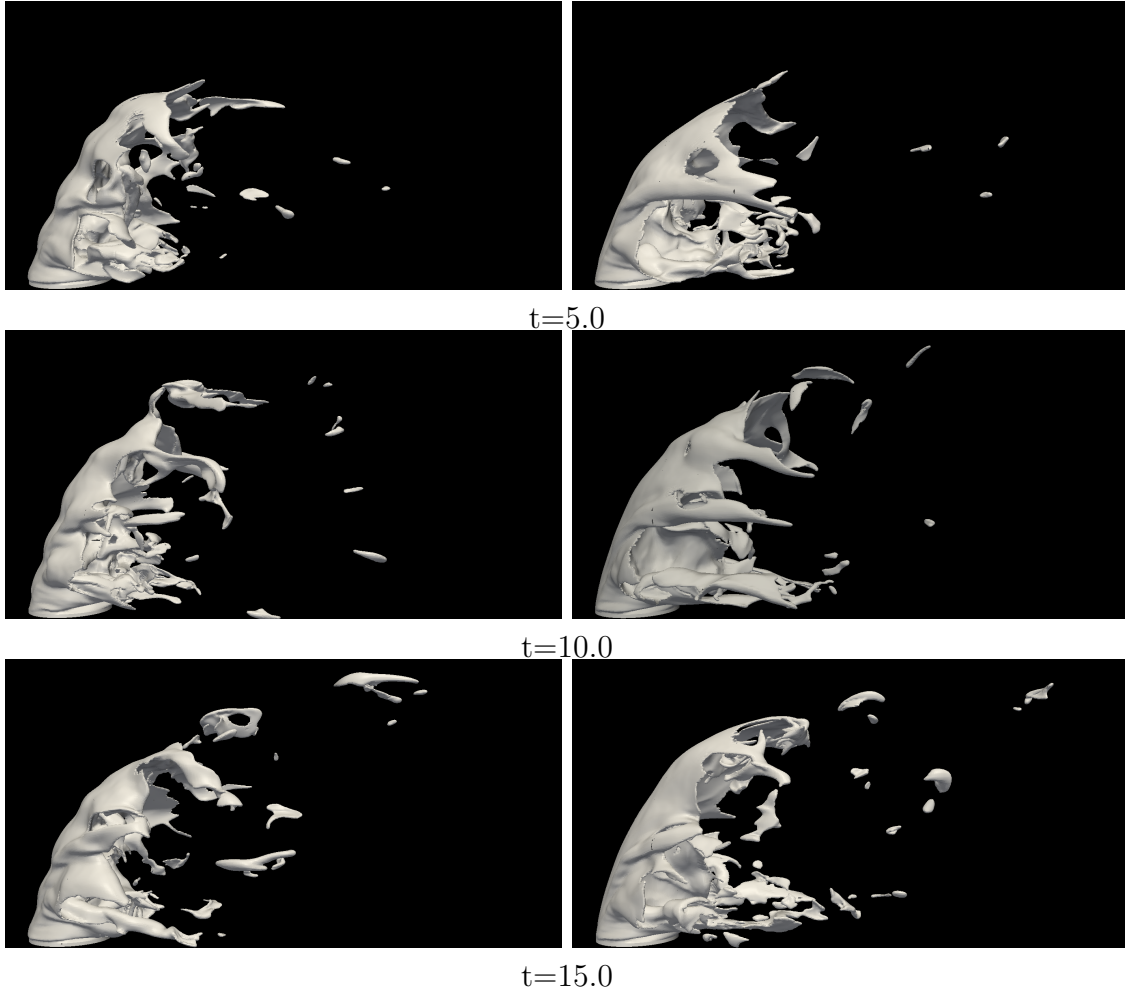


Figure 7.14: Side view snapshots of jet in crossflow atomization with density ratio $r=100$ at $t=5, 10, 15$ time units (top to bottom). Rayleigh-Taylor instability (left), Kelvin-Helmholtz instability (right).

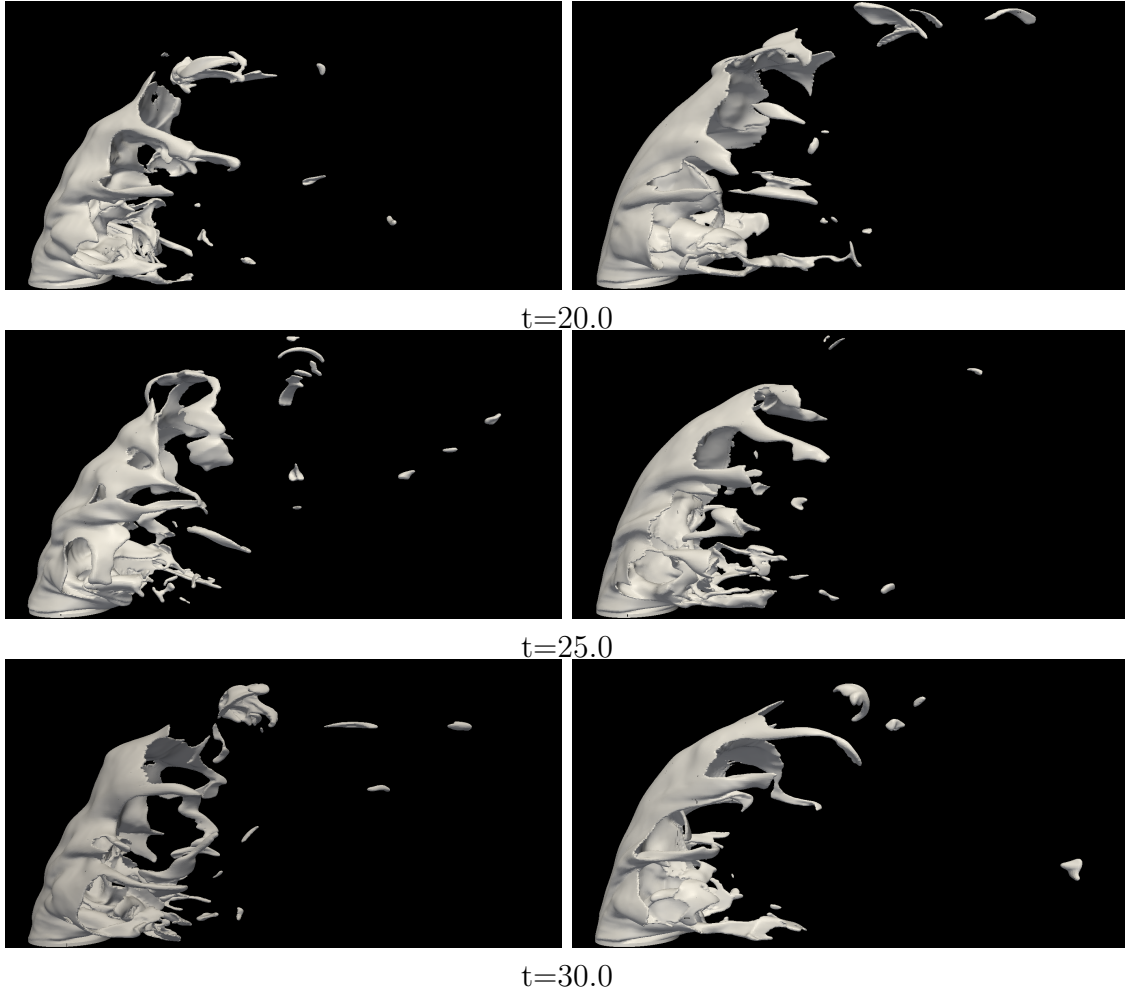


Figure 7.15: Side view snapshots of jet in crossflow atomization with density ratio $r=100$ at $t=20, 25, 30$ time units (top to bottom). Rayleigh-Taylor instability (left), Kelvin-Helmholtz instability (right).

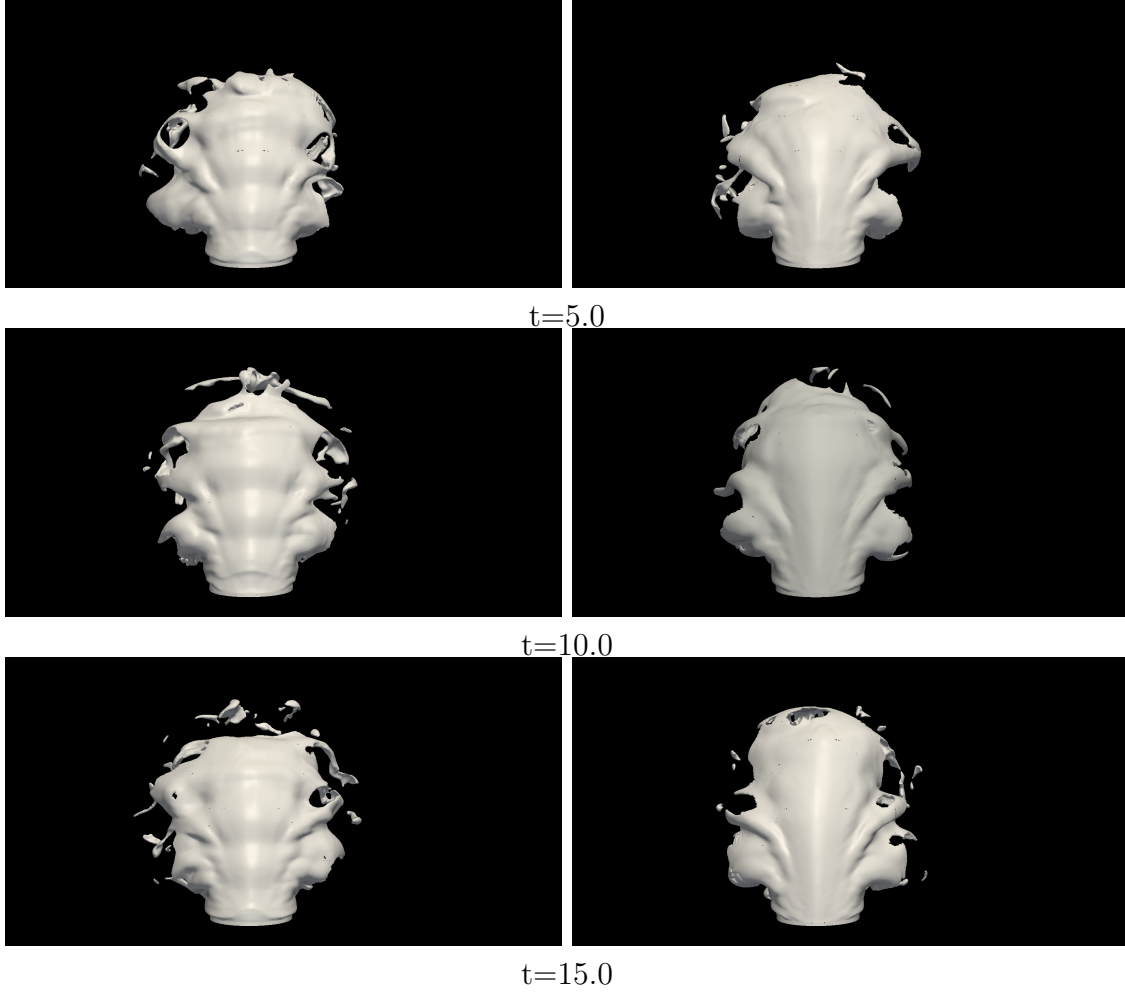


Figure 7.16: Front view snapshots of jet in crossflow atomization with density ratio $r=100$ at $t=5, 10, 15$ time units (top to bottom). Rayleigh-Taylor instability (left), Kelvin-Helmholtz instability (right).

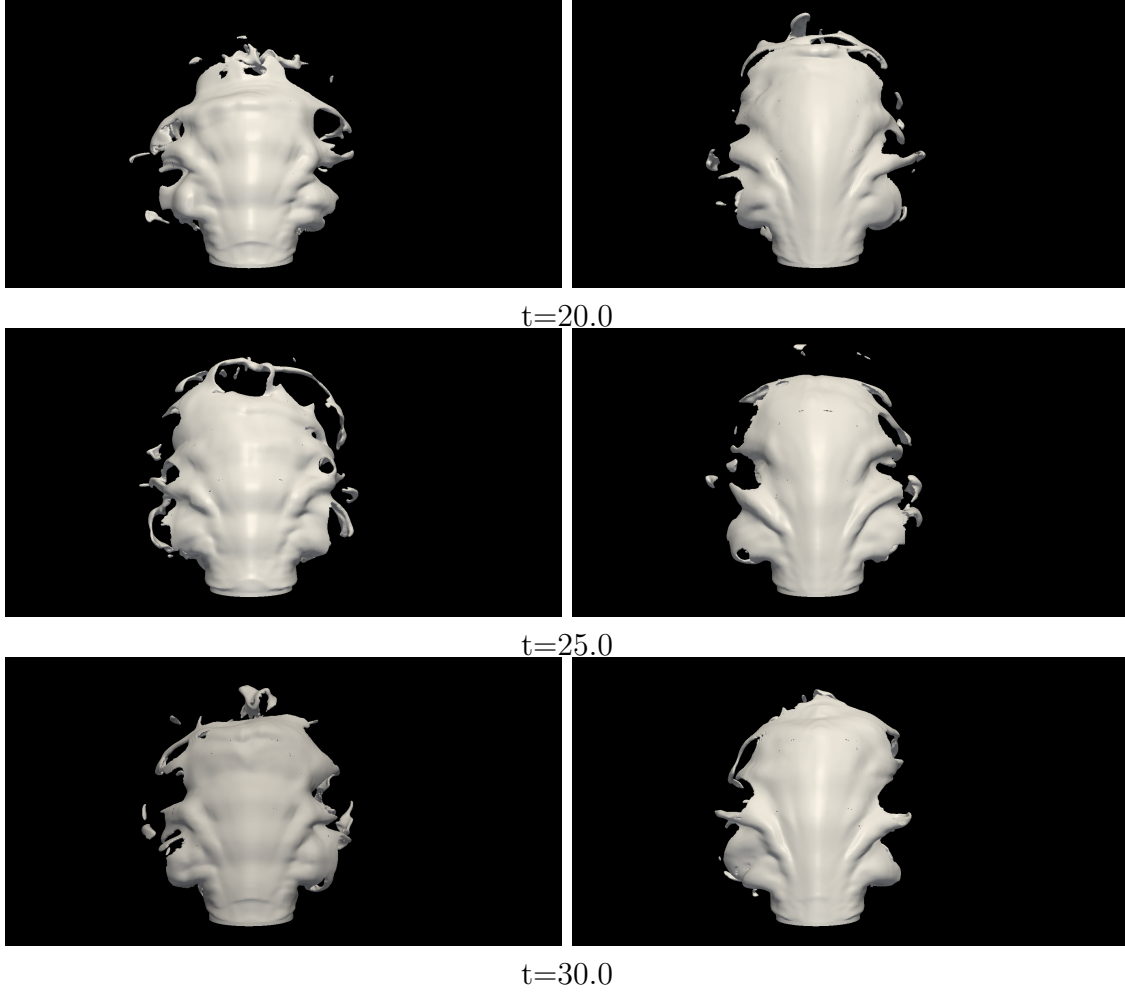


Figure 7.17: Front view snapshots of jet in crossflow atomization with density ratio $r=100$ at $t=20, 25, 30$ time units (top to bottom). Rayleigh-Taylor instability (left), Kelvin-Helmholtz instability (right).

Chapter 8

Summary and Future Work

Summary and Conclusion

The atomization of a liquid jet by a high speed cross-flowing gas has many applications such as gas turbines and augmentors. The mechanisms by which the liquid jet initially breaks up, however, are not well understood. Detailed numerical simulations can offer better understanding of the underlying physical mechanisms that lead to the breakup of the injected liquid jet. In this work, we presented detailed numerical simulation results of turbulent liquid jets injected into turbulent gaseous crossflows for different inflow jet boundary conditions. We employed a finite volume, balanced force fractional step flow solver to solve the Navier-Stokes equations coupled to a Refined Level Set Grid method to follow the phase interface. To enable the simulation of atomization of high density ratio fluids, discrete consistency between the solution of the conservative momentum equation and the level set based continuity equation was ensured by developing and employing the Rescaled Conservative Momentum Transport method.

Different numerical simulations were performed using different numerical boundary conditions based on the experimental study[1] all having same nominal characteristics numbers and yet showing markedly different behavior. The results indicate the importance of the boundary condition to be fully defined in studying jet in crossflow atomization. Looking at the jet penetrations from simulations using different boundary conditions indicates the dependency of the results on local momentum flux ratios rather than nominal values of momentum flux ratio.

To analyze the instability mechanism that causes the liquid column injected into the crossflow gas to breakup, results from proper orthogonal decomposition of

side view images extracted from detailed numerical simulations of the near injector primary atomization region [3] were used. POD analysis shows a single dominant wavelength with the associated interface corrugation traveling downstream with the jet. Using consistent temporal averaging of the simulation data, mean interface geometries and boundary layer velocity profiles were extracted. These were used to calculate the most unstable wavelength of the linear shear layer instability following the procedure of Zaleski et al.[38]. In addition to shear layer instability we analyzed Rayleigh-Taylor as a potential instability mechanism of the liquid column. The theoretical wavelengths are comparable to those extracted from the simulation data. Moreover, nonlinear instability analysis was performed. Inflow jet boundary condition in those simulations were an averaged database to achieve the mean solution to the problem. Nozzle exit was forced to oscillate with the wavelengths from the linear analysis results. Nonlinear analysis results are consistent with the linear analysis, suggesting the Rayleigh-Taylor instability having more impact on the jet breakup. Results also show dependency of the results on the density ratio.

Future Works

As was shown in chapter 6, the boundary condition of the inflow jet changes the outcome of the atomization and effects all the characteristics of the jet in crossflow including jet penetration and drop size distribution. We analyzed different boundary conditions for the liquid jet by replacing the nozzle geometry with a database at the nozzle exit. Including the whole complex geometry of the nozzle in the simulations will produce results that are more realistic and comparable to the experimental results, but on the other hand it will be more costly and complicated to perform.

Another problem that can be explored further is the effect of density ratio on jet in crossflow characteristics such as jet penetration and drop size distribution for different sets of We numbers and momentum flux ratios, as well as finding the most

unstable growth rate and wavelength of the Rayleigh-Taylor and Kelvin- Helmholtz instabilities for those configurations.

REFERENCES

- [1] C. T. Brown and V. G. McDonell, “Near field behavior of a liquid jet in a crossflow,” *ILASS Americas, 19th annual conference on Liquid Atomization and Spray Systems*, vol. 19, 2006.
- [2] H. Lamb, “Hydrodynamics,” *Dover Publications, New York*, 1945.
- [3] M. Herrmann, M. Arienti, and M. Soteriou, “The impact of density ratio on the liquid core dynamics of a turbulent liquid jet injected into a crossflow,” *Journal of Engineering for Gas Turbines and Power*, vol. 133(6), pp. 061 501:1–9, 2011.
- [4] P. Marmottant and E. Villermaux, “On spray formation,” *Journal of Fluid Mechanics*, vol. 498, pp. 73–111, 2003.
- [5] K. A. Sallam and G. M. Faeth, “Breakup of round nonturbulent liquid jets in gaseous crossflow,” *AIAA*, vol. 24, pp. 2529–2540, 2003.
- [6] J. Martin and W. Moyce, “An experimental study of the collapse of liquid columns on a rigid horizontal plane,” *Philosophical Transactions of the Royal Society of London. Series A, Mathematical and Physical Sciences*, vol. 244, pp. 312–324, 1952.
- [7] M. Herrmann, “A balanced force refined level set grid method for two-phase flows on unstructured flow solver grids,” *Computational Physics*, vol. 227(4), pp. 2674–2706, 2008.
- [8] M. Herrmann, “Detailed numerical simulations of the primary atomization of a turbulent liquid jet in crossflow,” *Journal of Engineering for Gas Turbines and Power*, vol. 132(6), pp. 061 506:1–10, 2010.
- [9] D. Sedarsky and M. Paciaroni, “Model validation image data for breakup of a liquid jet in crossflow: part i,” *Experimental Fluids*, vol. 49, p. 391408, 2010.
- [10] J. C. Lasheras and E. J. Hopfinger, “Liquid jet instability and atomization in a coaxial gas stream,” *Annual Review of Fluid Mechanics*, vol. 32, pp. 275–308, 2000.
- [11] M. Linne, M. Paciaroni, T. Hall, and T. Parker, “Ballistic imaging of the near field in a diesel spray,” *Experiments In Fluids*, vol. 40, pp. 836–846, 2006.

- [12] Y. Wang, X. Liu, K. Im, W. Lee, J. Wang, K. Fezzaa, D. L. S. Hung, and J. R. Winkelman, "Ultrafast x-ray study of dense-liquid-jet flow dynamics using structure-tracking velocimetry," *Nature Physics*, vol. 4, pp. 305–309, 2008.
- [13] M. A. Linne, M. Paciaroni, J. R. Gord, and T. R. Meyer, "Ballistic imaging of the liquid core for a steady jet in crossflow," *Applied Optics*, vol. 44(31), pp. 6627–6634, 2005.
- [14] C.-L. Ng, R. Sankarakrishnan, and K. Sallam, "Bag breakup of nonturbulent liquid jets in crossflow," *International Journal of Multiphase Flow*, vol. 34, p. 241259, 2008.
- [15] P. Wu, R. P. Fuller, K. A. Kirkendall, and A. S. Nejad, "Breakup processes of liquid jets in subsonic crossflows," *Propulsion and Power*, vol. 13, pp. 64–73, 1997.
- [16] J. N. Stenzler, J. G. Lee, D. Santavicca, and W. Lee, "Penetration of liquid jets in a cross-flow," *Atomization and Sprays*, vol. 8, pp. 887–906, 2006.
- [17] R. Scardovelli and S. Zaleski, "Direct numerical simulation of free-surface and interfacial flow," *Fluid Mechanics*, vol. 31, pp. 567–603, 1999.
- [18] M. Raessi, "A level set based method for calculating flux densities in two-phase flows," *Center of Turbulence Research, Annual Research Briefs*, pp. 467–478, 2008.
- [19] M. Raessi and H. Pitsch, "Modeling interfacial flows characterized by large density ratios with the level set method," *Center of Turbulence Research, Annual Research Briefs*, pp. 467–478, 2009.
- [20] M. Rudman, "A volume-tracking method for incompressible multifluid flows with large density variations," *International Journal for Numerical Methods in Fluids*, vol. 28, pp. 357–378, 1998.
- [21] M. Sussmana and E. G. Puckett, "A coupled level set and volume-of-fluid method for computing 3d and axisymmetric incompressible two-phase flows," *Computational Physics*, vol. 162(2), pp. 301–337, 2000.
- [22] D. Enrighta, R. Fedkiwb, J. Ferziger, and I. Mitchella, "A hybrid particle level set method for improved interface capturing," *Computational Physics*, vol. 183(1), pp. 83–116, 2002.

- [23] S. P. van der Pijl, A. Segal, C. Vuik, and P. Wesseling, “A mass-conserving level-set method for modelling of multi-phase flows,” *International Journal for Numerical Methods in Fluids*, vol. 47(4), p. 339361, 2004.
- [24] D. Peng, B. Merriman, S. Osher, H. Zhao, and M. Kang, “A pde-based fast local level set method,” *Computational Physics*, vol. 155(2), pp. 410–438, 1999.
- [25] G. Jiang and D. Peng., “Weighted eno schemes for hamilton-jacobi equations,” *SIAM Journal on Scientific computing*, vol. 21(6), p. 21262143, 2000.
- [26] B. Cockburna and C. Shub, “The rungekutta discontinuous galerkin method for conservation laws v: Multidimensional systems,” *Computational Physics*, vol. 141(2), pp. 199–224, 1998.
- [27] M. Sussman, P. smerka, and S. Osher, “A level set approach for computing solutions to incompressible two-phase flow,” *Computational Physics*, vol. 114, p. 146159, 1994.
- [28] J. Kim and P. Moin, “Application of a fractional-step method to incompressible navier-stokes equations,” *Computational Physics*, vol. 59(2), pp. 308–323, 1985.
- [29] K. Mahesh, G. Constantinescu, and P. Moin, *Computational Physics*, vol. 197, pp. 215–240, 2004.
- [30] M. G. S. V. Apte and P. Moin, “Les of atomizing spray with stochastic modeling of secondary breakup,” *Journal of Multiphase Flow*, vol. 29, pp. 1503–1522, 2003.
- [31] M. H. D. Kim, O. Desjardins and P. Moin, “The primary breakup of a round liquid jet by a coaxial flow of gas,” *ILASS Americas 20th Annual Conference on Liquid Atomization and Spray Systems*, vol. 20, 2007.
- [32] W. L. Oberkampf, “Verification and validation in computational simulation,” *2004 Transport Task Force Meeting*, pp. 1–48, 2004.
- [33] A. Prosperetti, “Motion of two superposed viscous fluids,” *Physics of Fluids*, vol. 24(7), pp. 1217–1223, 1981.
- [34] M. Bussmann, D. B. Kothe, and J. M. Sicilian, “Modeling high density ratio incompressible interfacial flows,” *ASME Conference Proceedings*, pp. 707–713, 2002.

- [35] R. P. F. P. K. Wu, K. A. Kirkendall and A. S. Nejad, “Breakup process of liquid jets in subsonic cross flows,” *Propulsion and Power*, vol. 13(1), 1997.
- [36] J. P. K. Meyer and O. Ozcan, “A turbulent jet in crossflow analysed with proper orthogonal decomposition,” *Fluid Mechanics*, vol. 583, p. 199227, 2007.
- [37] P. Moin and Moser, “Characteristic-eddy decomposition of turbulence in a channel,” *Journal of Fluid Mechanics*, vol. 200, pp. 471–509, 1989.
- [38] P. Yecko, S. Zaleski, and J. M. Fullana, “Viscous modes in two-phase mixing layers,” *Physics of Fluids*, vol. 14, pp. 4115–4122, 2002.
- [39] K. O. Mikaelian, “Effect of viscosity on rayleigh-taylor and richtmyer-meshkov instabilities,” *Physical Review*, vol. 47, pp. 375–383, 1993.